The effects of air film pressure constraints and top foil detachment on the static equilibrium, stability and modal characteristics of a foil-air bearing rotor model

DOI:
10.1016/j.jsv.2020.115590

Document Version
Accepted author manuscript

The effects of air film pressure constraints and top foil detachment on the static equilibrium, stability and modal characteristics of a foil-air bearing rotor model

Philip Bonello

Department of Mechanical, Aerospace and Civil Engineering,

University of Manchester,

Sackville Street, Manchester M13 9PL, United Kingdom

Corresponding author: P. Bonello

Email: philip.bonello@manchester.ac.uk

The effects of air film pressure constraints and top foil detachment on the static equilibrium, stability and modal characteristics of a foil-air bearing rotor model

P Bonello,

Department of Mechanical, Aerospace and Civil Engineering, University of Manchester, United Kingdom

Abstract

The linear force coefficients method (LFCM) has been a mainstay in the computation of the onset of instability speed (OIS) and Campbell diagrams of foil-air bearing (FAB) rotor systems, despite reported inconsistencies with low amplitude dynamic analysis of the nonlinear system. The author recently established a linearisation method that eliminates such errors since it is based on the Jacobian of the nonlinear system. Unlike LFCM, this static equilibrium, stability and modal analysis (SESMA) procedure is not restricted to a spring-damper foil model. This paper investigates for the first time the effects of air film constraints and top foil detachment using SESMA, backed by transient nonlinear dynamic analysis (TNDA). The novel FAB model comprises an air film acting on a modal beam top foil that can detach from discretely distributed bumps according to a smoothed bilinear model. Application to a symmetric rigid rotor on single-pad FABs reveals abrupt shifts in modal frequencies and damping as the contact state of a bump with the top foil changes with speed. The applicability of the Gümbel correction for simpler models is illustrated. The SESMA procedure operates efficiently and accurately. The TNDA results present the first independent verification of previously presented top foil detachment simulations.

Keywords: Foil-air bearings; bilinearity; nonlinear analysis; linearisation; Campbell diagrams

Table of Nomenclature

Main symbols only (all symbols used defined in text)

$(\ )'$	Differentiation with respect to τ
$\mathbf{a}.*\mathbf{b}$	Vector of products of corresponding elements of $\mathbf{a}$, $\mathbf{b}$
$\mathrm{mod}\{\boldsymbol{\upsilon}\}$, $\arg\{\boldsymbol{\upsilon}\}$	Vectors of moduli, arguments of elements of vector $\boldsymbol{\upsilon}$
c	Radial clearance of FAB
c_n	Reduction factor, eq. (34)
C	Cut-off threshold factor, eq. (33)
$\mathbf{C}_{\mathrm{b}}$	Zero-frequency receptance matrix of bump foil , eq. (14)
$\tilde{\mathbf{d}}_{\mathrm{L}}$, $\tilde{\mathbf{d}}_{\mathrm{R}}$	Vectors of non-dimensional radial deflections of top foil at bump apex locations of L, R bearings, eq. (11).
$\tilde{d}_{n_{\mathrm{L}}}$, $\tilde{d}_{n_{\mathrm{R}}}$	n^{th} element of $\tilde{\mathbf{d}}_{\mathrm{L}}$, $\tilde{\mathbf{d}}_{\mathrm{R}}$
$\mathbf{f}_{\mathrm{J_L}}$, $\mathbf{f}_{\mathrm{J_R}}$	Vectors of FAB journal forces, eq. (4)
$\mathbf{f}_{\mathrm{p_L}}$, $\mathbf{f}_{\mathrm{p_R}}$	Vectors of discretised air pressure forces on top foils, eq. (12)
$\mathbf{f}_{\mathrm{b_L}}$, $\mathbf{f}_{\mathrm{b_R}}$	Vectors of bump reactions, eq. (13)
$\mathbf{f}_{\mathrm{sm}}$	Smoothing function, eq. (15)
$\tilde{h}$	Air film gap divided by c, eq. (20)
H	Total number of rotor component modes
H_{F}	Total number of top foil component modes
i, j	Counters for FD grid
$\mathbf{J}$	Jacobian, eq. (22)
$\mathbf{K}_{\mathrm{b\,eff}}$	Effective bump foil stiffness matrix (Figure 2)
L	Axial length of FAB
N_{b}	Number of bumps
N_z, N_θ	Number of points of FD grid along ξ, θ directions

p	Air film pressure (absolute)
p_{a}	Ambient pressure
$\tilde{p}$	$= p/p_{\mathrm{a}}$
$\mathbf{q}$	Vector of rotor modal coordinates
$\mathbf{q}_{\mathrm{F_L}}$, $\mathbf{q}_{\mathrm{F_R}}$	Vectors of top foil modal coordinates at L, R bearings
R	Undeformed inner radius of top foil
$\mathbf{s}$	Vector of state variables, eqs. (1, 3)
$\mathbf{s}_{\mathrm{E}}$	Static equilibrium value of $\mathbf{s}$
$\mathbf{s}_{\mathrm{F_{L,R}}}$	State variables of top foils of L, R bearings, eq. (7)
t	Time in seconds
$\widetilde{\mathbf{w}}_{\mathrm{L}}$, $\widetilde{\mathbf{w}}_{\mathrm{R}}$	Vectors of non-dimensional radial deflections of top foil at angular locations of FD grid of L, R bearings, eq. (8)
$x_{\mathrm{J}}, y_{\mathrm{J}}$	Cartesian displacements of journal centre J relative to (fixed) bearing centre
$\boldsymbol{\varepsilon}_{\mathrm{L,R}}$	Journal eccentricity vectors, eq. (5)
$\Delta\xi$, $\Delta\theta$	FD grid spacings in ξ, θ
ξ	$= z_{\mathrm{local}}/R$, z_{local} being the local axial coordinate
ζ_n	Viscous damping ratio of coupled rotor-FAB mode no. *n*
ζ_{F_r}	Viscous damping ratio of top foil component mode no. *r*
η	foil hysteretic damping factor
θ	Angular coordinate (Figure 1b)
θ_{b_n}	θ values at the bump apexes
$\boldsymbol{\psi}_{\mathrm{L}}$, $\boldsymbol{\psi}_{\mathrm{R}}$	Vectors of air film state variables at FD grid locations, eq. (3)
ψ	$\equiv \tilde{p}\tilde{h}$, air film state variable
τ	Non-dimensional time ($= \Omega t/2$)
ω_{ref}	Reference frequency for conversion from hysteretic damping, eq. (13)
$\widetilde{\omega}_{\mathrm{ref}}$	$= \omega_{\mathrm{ref}}/\Omega$

Ω	Rotational speed in rad/s
$\boldsymbol{\rho}^{(n)}$	Eigenvectors of matrix $\mathbf{J}$ in eq. (22)
$\boldsymbol{\rho}_{\mathbf{q}}^{(n)}$, $\boldsymbol{\rho}_{\mathbf{s}_{\mathrm{F_{L,R}}}}^{(n)}$	Eigenvectors partitioned as per eq. (3)
$\tilde{\boldsymbol{\rho}}^{(n)}$	Scaled eigenvector, eq. (30)
ϱ	Bilinear smoothing parameter, eq. (13)
σ	Scaling parameter, eq. (26)
$\varpi_{\mathrm{d},n}$	Damped natural circular frequency of coupled rotor-FAB mode no. n
$\boldsymbol{\chi}$	Nonlinear vector function, eq. (1)

Abbreviations

CLE/FTE	Clamped leading edge / free trailing edge
EPM	Extended perturbation method
FFSMM	Full foil structure modal model
FLE/CTE	Free leading edge / clamped trailing edge
FAB	Foil air bearing
FE, FD	Finite Element, Finite Difference
LFCM	Linear force coefficients method
OIS	Onset of instability speed
RE	Reynolds Equation
SEFM	Simple equivalent foundation model
SEP	Static equilibrium position
SESA	Static equilibrium and stability analysis
SESMA	Static equilibrium stability and modal analysis
TNDA	Transient nonlinear dynamic analysis

Main subscripts

L, R	Left, right hand bearings

1. INTRODUCTION

Dynamic analysis is of fundamental importance in the drive to increase the scope and breadth of oil-free machinery operating on foil-air bearings (FABs, also known as gas foil bearings) [1]. The dynamic response of a generic rotor-FAB system (Figure 1) is governed by the coupling of the rotor with the air films and associated foil structures that make up its bearings. The rotor, each air film, and each foil structure, are domains represented by time-based differential equations [2]. The dynamical system representation of the resulting coupled nonlinear model follows the generic state space format [3]

$$\mathbf{s}' = \boldsymbol{\chi}(\tau, \mathbf{s}) \tag{1}$$

where $(\,)'$ denotes differentiation with respect to the time variable τ, $\mathbf{s}$ is the state vector and $\boldsymbol{\chi}$ is a vector of nonlinear functions of $\mathbf{s}$ and τ (the explicit dependency on τ arising from the external dynamic excitation $\mathbf{f}_{\text{ext}}$ e.g. rotating unbalance) [3]. The system is typically analysed for the following:

a) The nonlinear response;

b) Free linear perturbations about the static equilibrium configuration at a given rotational speed Ω.

The latter involves stability analysis for the onset of instability speed (OIS) and modal analysis for Campbell diagrams [3]. As far as nonlinear response analysis is concerned, in order to reduce the computational burden, it has been the practice for many years to adopt an approximate non-simultaneous solution approach wherein the air film, foil and rotor equations were decoupled by approximating the air film equations as algebraic, rather than differential, equations e.g. [4, 5]. With regard to free perturbation analysis, the traditional approach has been to use the frequency-domain linear force coefficients method (LFCM) [6] for computing the OIS [7] and generating the Campbell diagrams [8, 9]. Problems and/or limitations associated with these traditional approaches have been widely reported e.g. [2, 7, 10-13] and these stem from their violation of the fully coupled nature of the dynamical system (eq. (1)) [3].

A rotor-FAB system was first expressed and analysed as a dynamical system in 2013/14 by Bonello and Pham [14, 10]. This, and subsequent work from Bonello et al. e.g. [11, 2, 3] devised efficient methods that do away with the aforementioned traditional approaches, thus bringing the dynamic analysis of rotor-

FAB systems into line with standard nonlinear dynamics analysis [3]. In these works the nonlinear response for given initial conditions $\mathbf{s}(0)$ is obtained via transient nonlinear dynamic analysis (TNDA) using readily available advanced integrator routines that were devised for the universal format of eq. (1). The static equilibrium state $\mathbf{s} = \mathbf{s}_{\mathrm{E}}$ of the system of eq. (1) at a given Ω is directly obtained by setting $\mathbf{s}' = \mathbf{0}$ for $\mathbf{f}_{\mathrm{ext}} = \mathbf{0}$ and solving the resulting set of nonlinear algebraic equations. The dynamics of free linear perturbations $\Delta\mathbf{s}$ about $\mathbf{s} = \mathbf{s}_{\mathrm{E}}$ are examined by computing the eigenvalues of the Jacobian matrix $\partial\boldsymbol{\chi}/\partial\mathbf{s}|_{\mathbf{s}=\mathbf{s}_{\mathrm{E}}}$ [10, 11]. The dominant eigenvalue (of most positive real part) determines the OIS, marking the birth of self-excited vibration (Hopf bifurcation). The process of finding $\mathbf{s}_{\mathrm{E}}$ and determining the OIS introduced in [10] for rotor-FAB systems is referred to as static equilibrium and stability analysis (SESA) [11]. Such analysis focuses only on the damping ratio of the dominant mode. Recently, Bonello [3, 15] developed the Jacobian eigenvalues approach into a full analysis of the vibration modes about $\mathbf{s} = \mathbf{s}_{\mathrm{E}}$. As shown in [3], there are a multitude of eigenvectors for given Ω, since, apart from the rotor state variables, $\mathbf{s}$ includes the numerous air film state variables arising from Finite Difference (FD) or Finite Element (FE) discretisation of the Reynolds Equation (RE), and the foil state variables. However, only a small proportion of these eigenvectors involve significant rotor vibration. Hence, for the purpose of extracting the Campbell diagram, an automated filtering process was devised [3]. The attributes of any mode (e.g. frequency, damping ratio, whirl direction) could be verified by TNDA of the original system (eq. (1)) from mode-specific initial conditions derived from its eigenvector [3]. The upgraded SESA of [3] shall henceforth be referred to by the more precise acronym SESMA (static equilibrium, stability and modal analysis). The above described approach for TNDA or SESMA, based on eq. (1), is referred to as "simultaneous" [10] or "(fully) coupled" [16].

The TNDA approach of Bonello at al. [10, 11, 14] has been taken up by a growing number of researchers e.g. [7, 12, 13, 17-20]. There has been less take-up of the SESA/SESMA approach of [10, 11, 3, 15], due to continued attachment to the LFCM, despite known discrepancies between its OIS prediction and the OIS determined from low-amplitude time domain integration of the nonlinear system (simultaneous or not) [7]. However, Gu et al. [20] followed the SESA approach of Bonello and Pham [10] for the OIS and,

most recently, von Osmanski et al. [16] adopted the SESMA approach of Bonello [3, 15] (but with *ad hoc* filtering) as a benchmark for troubleshooting the application of LFCM to FABs. SESMA can be used as the benchmark linearisation method since it works directly on the Jacobian of eq. (1), and is therefore perfectly consistent with low-amplitude TNDA (while being much faster) [3]. It is noted that the works in [16, 20] used the alternative implicit representation $\mathbf{M}(\mathbf{s})\mathbf{s}' = \check{\boldsymbol{\chi}}(\tau, \mathbf{s})$ which nonetheless can be expressed in the explicit format of eq. (1) in the normal case where all domains are represented by time-based differential equations [16], as was the case in [16, 20].

With regard to the aforementioned problem with the LFCM, it was recently found by Pronobis and Liebich [21], and later by [16], that previous works (e.g. [4, 5, 7]) comparing LFCM with time domain analysis did not ensure that the damping was precisely equivalent in the two methods. This problem arose since LFCM is formulated in the frequency domain, and can accommodate a hysteretic damping loss factor (η), whereas time domain analysis requires an equivalent viscous damping coefficient. Once this disparity was resolved, the discrepancies between LFCM and time domain were reduced. Nonetheless, discrepancies remain [21, 16] and increase with decreasing foil stiffness [16]. von Osmanski et al. [16] went on to extend LFCM to consider the dependency of the air pressure on foil deflection ("extended perturbation method" (EPM)). The EPM resulted in the virtual elimination of the discrepancies with the benchmark for the system considered, thus lending validation to the hypothesis put forward in [7] that the omission of the foil deflection from the Taylor series expansion of the pressure (as done in LFCM [6]) is fundamentally erroneous. It is noted that the benchmark modes/Campbell diagram of [16] are the essentially the same as those of [15], subject to minor changes arising from a change to the damping model (section 4.4).

Another major limitation with LFCM, and the considerably more complicated EPM, is their inapplicability to complex foil structures, since they require a dynamic foil stiffness (based on a spring-damper model). In contrast, the SESMA methodology of [3] does not have this limitation.

With few exceptions [17, 22], the coupled analysis based on eq. (1) has been done using a simple equivalent foundation model (SEFM) for the foil structure domains. The SEFM ignores the top foil,

assuming it is always stuck to the bump foil. A correction for the latter assumption may be achieved by applying the Gümbel condition, which involves truncating sub-atmospheric air film pressures prior to integrating for the journal forces [2, 13]. Although lumped inertia can be added, the SEFM assumes the bump foil to be a continuously distributed viscoelastic compliance, defined by a uniform stiffness per unit area typically given by the classical formula in [23]. This means that elastic coupling between neighbouring points is ignored, and it is assumed that there is a bump apex at each and every point of the air film mesh. A look at Figure 1b shows that this latter assumption is an idealisation that can be approximated in reality by having several strips of corrugated foil placed side-by-side in the z direction with their respective bumps staggered in the θ direction.

The aforementioned exceptions that have not used SEFM in the coupled analysis used either the full foil structure modal model (FFSMM) of Mohd and Bonello (2017) [22] or the bilinear model of Nielsen and Santos (2017) [17], both of which were applied to a single-pad FAB (Figure 1b). The FFSMM, used in TNDA, SESA/SESMA in [2, 3], is based entirely on the bump foil (i.e. ignores the top foil and its detachment) but recognises that the bumps are discretely distributed, elastically cross-coupled and have inertia. These features are captured in the modal equations of the bump foil. Nielsen and Santos [17] used modal equations for the top foil which can detach from the bump foil, the latter modelled as a SEFM (i.e. continuously distributed viscoelastic compliance). The *effective* bump foil was therefore *bilinear* SEFM. The top foil component modes in [17] were derived from the FE model of a clamped-free shell, and thus deflection variation in the z direction was allowed. The Nielsen and Santos model [17] originated from Nielsen's thesis [24]. It was only used in TNDA and the bulk of the analysis focused on the operating mode where the top foil was clamped at the leading edge and free at the trailing edge (CLE/FTE). This is opposite to the configuration in Figure 1b, which shows the manufacturer-recommended operating mode for *single-pad* FABs to avoid premature failure [2] i.e. a free leading edge/clamped trailing edge (FLE/CTE). The reason for the focus on CLE/FTE in [17, 24] is that sub-atmospheric pressure, that is known from SEFM (i.e. no-detachment) analysis under static loading to form near the trailing edge, will in reality cause a top foil with a *free* trailing edge to detach from the

bump foil in that region and reach a static equilibrium position once the pressures on either side equalise to atmospheric pressure. This is the rationale of applying the Gümbel condition to SEFM analysis. Hence, it was hypothesised in [17, 24] that the simulated journal trajectory with the bilinear (i.e. detachable top foil) model for CLE/FTE would follow that simulated by SEFM-Gümbel. This proved to be the case in [17, 24] and the SEFM-Gümbel was therefore described as the "validation model" for the bilinear model with CLE/FTE. The same cannot be said for the FLE/CTE case, for which there is only one TNDA simulation, found in Nielsen's thesis [24]. In this case, the bilinear model revealed sub-atmospheric pressure towards the trailing edge where the top foil cannot freely separate. This finding led Nielsen [24] to state that the Gümbel condition may not be appropriate for FLE/CTE application. It is noted that the detachment model of Nielsen and Santos [17] has not been verified against an alternative top foil detachment model. Arghir and Benchekroun [25] recently introduced a foil model that not only considers detachment of the top foil from the bump foil, but also separation of the bump foil from the bearing sleeve. Coulomb friction is also considered. However, the model in [25] was not used in a rotordynamic problem and its use within the fully coupled approach appears elusive at this stage.

The novel contribution of this paper is the first time investigation of the effects of air film constraints and top foil detachment on the static equilibrium, stability and modal characteristics (Campbell diagrams) of a rotor-FAB model. The recently introduced SESMA procedure [3] will be used, backed up by TNDA where needed. A secondary contribution will be the first independent verification of key results from the model of Nielsen and Santos in [17, 24]. To this end, a novel top foil detachment model is devised that combines key elements of those in [22] and [17]. As in [22] (and unlike [17]), the discrete distribution of the bumps will be recognised, and elastic coupling can be accommodated. However, unlike [22] (and like [17]), top foil detachment will be allowed and bump foil inertia ignored, the modal representation being used for the top foil (as in [17]), rather than the bump foil. Experimental analysis on the same design bump foil [22] shows that neglect of the bump foil inertia is justified for the range of speeds considered. Unlike [17], which only performed TNDA, the bilinearity of the new model has *smoothing* to ensure differentiability at all states required by the Jacobian. The parameter that controls the smoothing can also

be used to suppress detachment altogether, thus isolating the effect of detachment for investigative purposes. A finite difference (FD) model is used for the air film, unlike the finite element (FE) model used in [17]. The top foil will be modelled as a curved beam, as opposed to a shell model used in [17]. The assumption of constant foil deflection along the *z* direction makes it easier to relate the results to the previous no-detachment works on the same system, which all made this assumption e.g. [10, 15, 16]. The simulations consider both FLE/CTE and CLE/FTE to relate to the results in [17, 24].

Section 2 presents the fully coupled generic rotor-FAB model. An overview of the computational approach is presented in section 3. Section 4 presents the results for the case study, which is a rigid symmetric rotor mounted on two identical FABs. The conclusions are summarised in section 5.

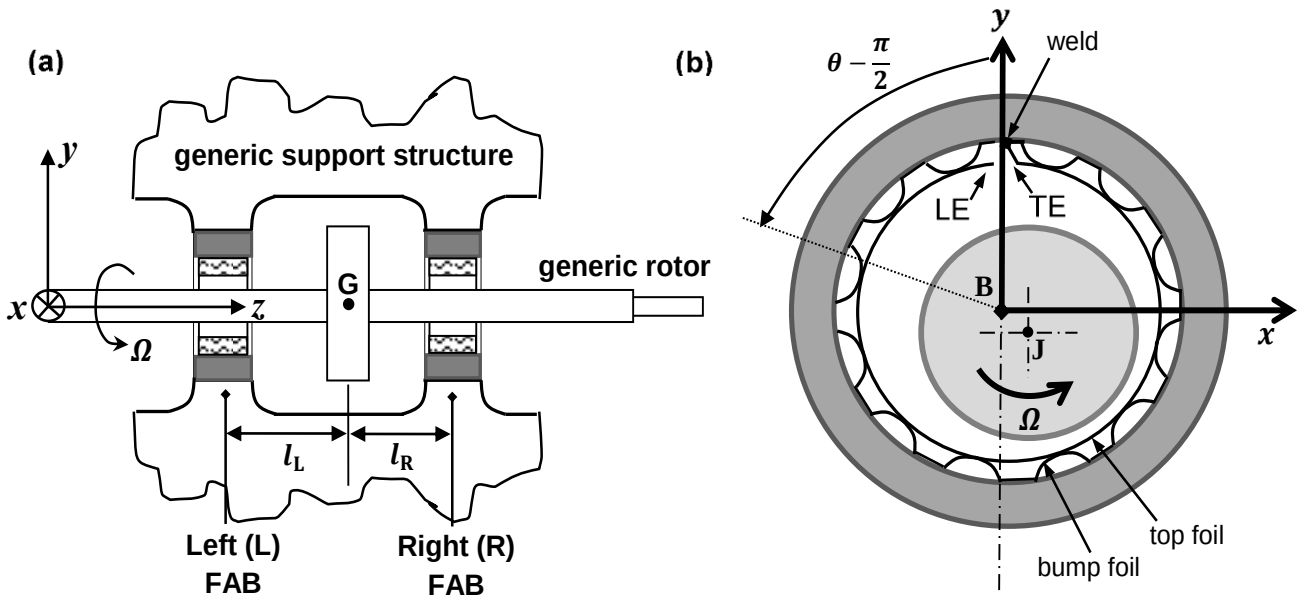

Figure 1. System schematic showing (a) generic rotor-FAB system and (b) single-pad bump-type FAB (configuration shown has a free leading edge/clamped trailing edge (FLE/CTE)).

2. MODELLING

The differential equations governing the nonlinear dynamics of the generic rotor-FAB system in Figure 1a can be expressed in the dynamical system form of eq. (1) as follows [3]:

$$\boldsymbol{\psi}_{\mathrm{L}}{}' = \mathbf{g}_{\mathrm{RE_L}}\left(\boldsymbol{\psi}_{\mathrm{L}}, \tilde{\mathbf{w}}_{\mathrm{L}}(\mathbf{s}_{\mathrm{F_L}}), \boldsymbol{\varepsilon}_{\mathrm{L}}(\mathbf{q})\right), \quad \mathbf{s}_{\mathrm{F_L}}{}' = \mathbf{g}_{\mathrm{Foil_L}}\left(\boldsymbol{\psi}_{\mathrm{L}}, \mathbf{s}_{\mathrm{F_L}}, \boldsymbol{\varepsilon}_{\mathrm{L}}(\mathbf{q})\right) \tag{2a, 2b}$$

$$\boldsymbol{\psi}_{\mathrm{R}}{}' = \mathbf{g}_{\mathrm{RE_R}}\left(\boldsymbol{\psi}_{\mathrm{R}}, \widetilde{\mathbf{w}}_{\mathrm{R}}(\mathbf{s}_{\mathrm{F_R}}), \boldsymbol{\varepsilon}_{\mathrm{R}}(\mathbf{q})\right),\ \mathbf{s}_{\mathrm{F_R}}{}' = \mathbf{g}_{\mathrm{Foil_R}}\left(\boldsymbol{\psi}_{\mathrm{R}}, \mathbf{s}_{\mathrm{F_R}}, \boldsymbol{\varepsilon}_{\mathrm{R}}(\mathbf{q})\right) \qquad \text{(2c, 2d)}$$

$$\begin{bmatrix}\mathbf{q}\\ \mathbf{q}'\end{bmatrix}' =$$

$$\begin{bmatrix} \mathbf{q}' \\ \frac{4}{\Omega^2}\left[-\boldsymbol{\Lambda}\mathbf{q} + \mathbf{H}_{\mathbf{f}_{\mathrm{u}}}^{\mathrm{T}}\mathbf{f}_{\mathrm{u}}(\tau) + \mathbf{H}_{\mathbf{f}_{\mathrm{s}}}^{\mathrm{T}}\mathbf{f}_{\mathrm{s}} + \frac{\Omega}{2}\mathbf{H}_{\mathbf{g}}^{\mathrm{T}}\mathbf{P}\mathbf{H}_{\boldsymbol{\alpha}}\mathbf{q}' + \mathbf{H}_{\mathbf{f}_{\mathrm{J_L}}}^{\mathrm{T}}\mathbf{f}_{\mathrm{J_L}}\left(\boldsymbol{\psi}_{\mathrm{L}}, \widetilde{\mathbf{w}}_{\mathrm{L}}(\mathbf{s}_{\mathrm{F_L}}), \boldsymbol{\varepsilon}_{\mathrm{L}}(\mathbf{q})\right) + \mathbf{H}_{\mathbf{f}_{\mathrm{J_R}}}^{\mathrm{T}}\mathbf{f}_{\mathrm{J_R}}\left(\boldsymbol{\psi}_{\mathrm{R}}, \widetilde{\mathbf{w}}_{\mathrm{R}}(\mathbf{s}_{\mathrm{F_R}}), \boldsymbol{\varepsilon}_{\mathrm{R}}(\mathbf{q})\right)\right] \end{bmatrix} \qquad \text{(2e)}$$

where: the non-dimensional time is defined as $\tau = \Omega t/2$ (Ω being the rotational speed); the subscripts "L", "R" used throughout refer to the left and right hand bearings in Figure 1a; the vector state variable $\mathbf{s}$ comprises sub-vectors containing state variables relating to the air films ($\boldsymbol{\psi}_{\mathrm{L}}$, $\boldsymbol{\psi}_{\mathrm{R}}$), the respective foils ($\mathbf{s}_{\mathrm{F_L}}, \mathbf{s}_{\mathrm{F_R}}$) and the rotor ($\mathbf{q}, \mathbf{q}'$):

$$\mathbf{s} = \begin{bmatrix}\boldsymbol{\psi}_{\mathrm{L}}^{\mathrm{T}} & \mathbf{s}_{\mathrm{F_L}}^{\mathrm{T}} & \boldsymbol{\psi}_{\mathrm{R}}^{\mathrm{T}} & \mathbf{s}_{\mathrm{F_R}}^{\mathrm{T}} & \mathbf{q}^{\mathrm{T}} & \mathbf{q}'^{\mathrm{T}}\end{bmatrix}^{\mathrm{T}} \qquad (3)$$

Although the case studied (section 4) is a symmetrical rotor-bearing system, the presentation is for a generic system where the vibration responses at L, R bearings can be different. To avoid excessive use of subscripts "L" and "R", it shall be assumed that the bearings are identical.

2.1 Rotor Equations (eqs. (2e))

The degrees of freedom of the rotor are transformed to modal coordinates using a truncated series of H component modes [3]. These are the undamped free vibration modes of the given system minus the nonlinear elements (FABs) at zero speed. The terms in eq. (2e) are defined as follows [3].

- $\mathbf{q}$ is the $H \times 1$ column matrix (vector) of modal coordinates;
- $\boldsymbol{\Lambda}$ is the $H \times H$ diagonal matrix of squares of the component modes' circular frequencies;
- $\mathbf{f}_{\mathrm{u}}$ is the vector of rotational unbalance forces;
- $\mathbf{f}_{\mathrm{s}}$ the vector of the distributed weight of the rotor;

- $\mathbf{f}_{\mathrm{J_{L,R}}}$ are the 2×1 vectors of air film pressure forces exerted by the L, R FABs on the respective journals in the *x*, *y* directions; taking the left hand FAB as an example, the forces in $\mathbf{f}_{\mathrm{J_L}}$ are obtained by integrating the air film pressure distribution $p(\xi, \theta, \tau)$ over the bearing area:

$$\mathbf{f}_{\mathrm{J_L}} = -2R^2 \int_{\xi=0}^{0.5L/R} \int_{\theta=0}^{2\pi} (p(\xi, \theta, \tau) - p_{\mathrm{a}}) \begin{bmatrix} \cos\theta \\ \sin\theta \end{bmatrix} d\theta d\xi \tag{4}$$

(where R and L are the radius and length respectively of the FAB, $\xi = \frac{z_{\mathrm{local}}}{R}$ the non-dimensional local axial coordinate and p_{a} is the absolute atmospheric pressure).

- the term $\mathbf{H}_{\mathbf{g}}^{\mathrm{T}} \mathbf{P} \mathbf{H}_{\boldsymbol{\alpha}} \mathbf{q}'$ accounts for any distributed gyroscopic effect;
- the matrices $\mathbf{H}_{\mathbf{f}_{\mathrm{u}}, \mathbf{f}_{\mathrm{s}}, \mathbf{f}_{\mathrm{J_L}}, \mathbf{f}_{\mathrm{J_R}}}$ are modal matrices associated with the vectors $\mathbf{f}_{\mathrm{u}}, \mathbf{f}_{\mathrm{s}}, \mathbf{f}_{\mathrm{J_L}}, \mathbf{f}_{\mathrm{J_R}}$ respectively;
- $\boldsymbol{\varepsilon}_{\mathrm{L,R}}$, are the journal eccentricity vectors at the two bearings,

$$\boldsymbol{\varepsilon}_{\mathrm{L,R}} = \mathbf{H}_{\mathbf{f}_{\mathrm{J_{L,R}}}} \mathbf{q}(\tau)/c \tag{5}$$

where c is the radial clearance of either bearing.

2.2 Foil Equations (eqs. (2b), (2d))

The foil equations are described with respect to the left hand FAB (eq. (2b)). The deflections of both top foil and bump foil are assumed to vary only in the θ direction. The top foil can therefore be modelled as a curved beam which contacts the bump foil at the discrete angular locations $\theta = \theta_{\mathrm{b}_n}$ $(n = 1 \ldots N_{\mathrm{b}})$ of the apexes of the bumps, if contact conditions are met. The bump foil is composed of a single corrugated strip and its inertia is neglected, but elastic cross-coupling between the bumps is allowed. The vibrating shape of the top foil is assumed to be represented by a truncated series of H_{F} undamped modes (top foil component modes). The vector $\widetilde{\mathbf{w}}_{\mathrm{L}}$ of non-dimensional deflections of the top foil in the radial direction at discrete values θ_j of θ within the FD grid is given by:

$$\widetilde{\mathbf{w}}_{\mathrm{L}} = \mathbf{H}_{\mathbf{w}} \mathbf{q}_{\mathrm{F_L}}(\tau)/c \tag{6}$$

where $\mathbf{H_w}$ is the matrix whose H_F columns are the $N_\theta \times 1$ mass-normalised eigenvectors containing the modal displacements of the top foil corresponding to the degrees of freedom within $\widetilde{\mathbf{w}}_\mathrm{L}$, and $\mathbf{q}_{\mathrm{F_L}}$ is the vector of modal coordinates of the top foil. The foil state vector in eq. (2b) is therefore

$$\mathbf{s}_{\mathrm{F_L}} \equiv \begin{bmatrix} \mathbf{q}_{\mathrm{F_L}} \\ \mathbf{q}'_{\mathrm{F_L}} \end{bmatrix} \tag{7}$$

Eq. (6) can be rewritten as:

$$\widetilde{\mathbf{w}}_\mathrm{L} = \mathbf{T}_\mathrm{F}\mathbf{s}_{\mathrm{F_L}} \tag{8}$$

where

$$\mathbf{T}_\mathrm{F} = [\mathbf{H_w}/c \quad \mathbf{0}_{N_\theta \times H_\mathrm{F}}] \tag{9}$$

and $\mathbf{0}_{N_\theta \times H_\mathrm{F}}$ is a matrix of zeros of dimension $N_\theta \times H_\mathrm{F}$.

The vector function $\mathbf{g}_{\mathrm{Foil_L}}$ in eq. (2b) is given by:

$$\mathbf{g}_{\mathrm{Foil_L}} \equiv \begin{bmatrix} \mathbf{q}'_{\mathrm{F_L}} \\ \frac{4}{\Omega^2}\left[-\frac{\Omega}{2}\mathbf{D}_\mathrm{F}\mathbf{q}'_{\mathrm{F_L}} - \mathbf{\Lambda}_\mathrm{F}\mathbf{q}_{\mathrm{F_L}} + \mathbf{H}_\mathbf{d}^\mathrm{T}\mathbf{f}_{\mathrm{p_L}}\left(\boldsymbol{\psi}_\mathrm{L}, \widetilde{\mathbf{w}}_\mathrm{L}(\mathbf{s}_{\mathrm{F_L}}), \boldsymbol{\varepsilon}_\mathrm{L}(\mathbf{q})\right) - \mathbf{H}_\mathbf{d}^\mathrm{T}\mathbf{f}_{\mathrm{b_L}}\left(\tilde{\mathbf{d}}_\mathrm{L}(\mathbf{q}_{\mathrm{F_L}}), \tilde{\mathbf{d}}'_\mathrm{L}(\mathbf{q}'_{\mathrm{F_L}})\right)\right] \end{bmatrix} \tag{10}$$

$\mathbf{\Lambda}_\mathrm{F} = \mathrm{diag}\left(\left[\cdots \varpi_{\mathrm{F}_r}^2 \cdots\right]\right)$ is the diagonal matrix of the squares of the natural circular frequencies ϖ_{F_r}, $r = 1 \ldots H_\mathrm{F}$, of the top foil modes, and $\mathbf{D}_\mathrm{F} = \mathrm{diag}\left(\left[\cdots 2\zeta_{\mathrm{F}_r}\varpi_{\mathrm{F}_r} \cdots\right]\right)$ is the modal damping matrix. $\tilde{\mathbf{d}}_\mathrm{L}$ is the vector of non-dimensional deflections of the top foil in the radial direction at the angular locations $\theta = \theta_{\mathrm{b}_n}$ of the bump apexes and is given by:

$$\tilde{\mathbf{d}}_\mathrm{L} = \mathbf{H}_\mathbf{d}\mathbf{q}_{\mathrm{F_L}}(\tau)/c \tag{11}$$

where $\mathbf{H_d}$ is the modal matrix whose H_F columns are the $N_\mathrm{b} \times 1$ mass-normalised eigenvectors containing the modal displacements of the top foil corresponding to the degrees of freedom within $\tilde{\mathbf{d}}_\mathrm{L}$.

$\mathbf{f}_{\mathrm{p_L}}$ is the $N_\mathrm{b} \times 1$ vector of air pressure forces discretised at the angular locations $\theta = \theta_{\mathrm{b}_n}$ of the bump apexes, each element of $\mathbf{f}_{\mathrm{p_L}}$ determined by integrating the regional air film pressure distribution over a bump projected area of $S \times L$, where S is the pitch:

$$\mathbf{f}_{\mathrm{p_L}} = \begin{bmatrix} \cdots & F_{\mathrm{p}_{n_\mathrm{L}}} & \cdots \end{bmatrix}^\mathrm{T}, \qquad F_{\mathrm{p}_{n_\mathrm{L}}} = 2R^2 \int_{\xi=0}^{0.5L/R} \int_{\theta=\theta_{\mathrm{b}_n}-\pi/N_\mathrm{b}}^{\theta_{\mathrm{b}_n}+\pi/N_\mathrm{b}} (p(\xi,\theta,\tau) - p_\mathrm{a})\, d\theta d\xi \qquad (12\text{a,b})$$

These forces act on the top foil and are countered by the reaction forces from bump foil, which are contained in $\mathbf{f}_{\mathrm{b_L}}$. By discretising the air film pressure forces at the same locations as the bump reactions, the issue of top foil sagging in-between bumps is eliminated from the model.

Assuming that the bump foil damping has been quoted in terms of a hysteretic damping factor η, this paper proposes the following expression for $\mathbf{f}_{\mathrm{b_L}}$,

$$\mathbf{f}_{\mathrm{b_L}} = c\mathbf{K}_{\mathrm{b_{eff}}} \left(\tilde{\mathbf{d}}_\mathrm{L} + \frac{\eta}{2\widetilde{\omega}_\mathrm{ref}} \tilde{\mathbf{d}}'_\mathrm{L} \right) + \mathbf{f}_\mathrm{sm}\left(\tilde{\mathbf{d}}_\mathrm{L}, \varrho\right) \qquad (13)$$

where:

- $\mathbf{K}_{\mathrm{b_{eff}}}$ is the $N_\mathrm{b} \times N_\mathrm{b}$ effective stiffness matrix of the bump foil at the apexes, "effective" meaning that it depends on the state of contact of the bump foil with top foil.
- $\widetilde{\omega}_\mathrm{ref} = \omega_\mathrm{ref}/\Omega$, ω_ref being the reference frequency used to *change* the damping model of the bump foil to frequency-independent viscous damping, where the resulting viscous damping matrix is $\mathbf{K}_{\mathrm{b_{eff}}}\eta/\omega_\mathrm{ref}$ (in Ns/m) and ω_ref is fixed for a given speed. For comparison with previous works (e.g. [15, 17]), $\omega_\mathrm{ref} = \Omega$, unless otherwise stated. Further discussion on this, including the effect of using an alternative speed-dependent reference frequency (as done in [16]), is found in section 4.4.
- $\mathbf{f}_\mathrm{sm}$ is a smoothing force function, controlled by a smoothing parameter ϱ that is introduced to ensure differentiability at all states.

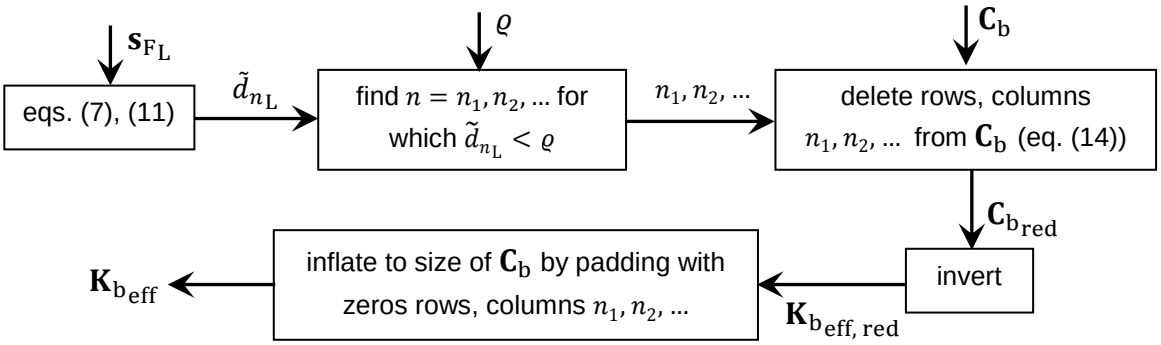

Figure 2. Algorithm for determination of the effective stiffness matrix $\mathbf{K}_{\mathrm{b_{eff}}}$ of the bump foil at the apexes, taking left (L) FAB as example.

$\mathbf{K}_{\mathrm{b_{eff}}}$ in eq. (13) is determined from the zero-frequency (i.e. inertia-less) compliance (receptance) matrix $\mathbf{C}_\mathrm{b}$ of the bump foil according to the algorithm in Figure 2. $\mathbf{C}_\mathrm{b}$ ($N_\mathrm{b} \times N_\mathrm{b}$) relates the elastic components of the reactions at the bump apexes $\mathbf{f}_{\mathrm{b_L}}^{(\mathrm{elast})}$ with *their* deflections $\mathbf{d}_{\mathrm{b_L}}$:

$$\mathbf{d}_{\mathrm{b_L}} = \mathbf{C}_\mathrm{b}\mathbf{f}_{\mathrm{b_L}}^{(\mathrm{elast})} \tag{14}$$

The bump reaction forces will be zero for those bumps that are not in contact with the top foil. In the present model, an individual bump no. *n* can have up to three alternative contact states, depending on the corresponding element no. *n* in the top foil deflection vector $\tilde{\mathbf{d}}_\mathrm{L}$ and the prescribed control parameter ϱ:

A. Contact: $\tilde{d}_{n_\mathrm{L}} \geq \varrho$

B. No contact: $\left(\tilde{d}_{n_\mathrm{L}} < \varrho\right)\&\left(\left|\tilde{d}_{n_\mathrm{L}}\right| \geq \varrho\right)$

C. "Marginal" contact: $\left|\tilde{d}_{n_\mathrm{L}}\right| < \varrho$

With reference to Figure 2, for any given foil state vector $\mathbf{s}_{\mathrm{F_L}}$ (eq. (7)), those elements $\tilde{d}_{n_\mathrm{L}}$ in $\tilde{\mathbf{d}}_\mathrm{L}$ (eq. (11)) for which $\tilde{d}_{n_\mathrm{L}} < \varrho$ are identified and the corresponding columns and rows are deleted from $\mathbf{C}_\mathrm{b}$ to produce the reduced matrix $\mathbf{C}_{\mathrm{b_{red}}}$, from which $\mathbf{K}_{\mathrm{b_{eff}}}$ is obtained as per Figure 2. This matrix (used in

first term of eq. (13)) can contain cross-coupling terms if these were present in $\mathbf{C}_{\mathrm{b}}$. However, with regards to the smoothing function $\mathbf{f}_{\mathrm{sm}}$, only diagonal (direct) terms $C_{\mathrm{b}_{n,n}}$ are considered:

$$\mathbf{f}_{\mathrm{sm}}\left(\tilde{\mathbf{d}}_{\mathrm{L}}, \varrho\right) = \begin{bmatrix} \cdots & F_{\mathrm{sm}}\left(\tilde{d}_{n_{\mathrm{L}}}, \varrho\right) & \cdots \end{bmatrix}^{\mathrm{T}} \tag{15}$$

where

$$F_{\mathrm{sm}}\left(\tilde{d}_{n_{\mathrm{L}}}, \varrho\right) = \begin{cases} \dfrac{c}{C_{\mathrm{b}_{n,n}}}\left(\dfrac{1}{4\varrho}\tilde{d}_{n_{\mathrm{L}}}^2 + \dfrac{1}{2}\tilde{d}_{n_{\mathrm{L}}} + \dfrac{\varrho}{4}\right) + \dfrac{c\eta}{2\widetilde{\omega}_{\mathrm{ref}} C_{\mathrm{b}_{n,n}}}\left(\dfrac{1}{2\varrho}\tilde{d}_{n_{\mathrm{L}}} + \dfrac{1}{2}\right), & \left|\tilde{d}_{n_{\mathrm{L}}}\right| < \varrho \\ 0, & \left|\tilde{d}_{n_{\mathrm{L}}}\right| \geq \varrho \end{cases} \tag{16a,b}$$

Using the above formulation, one can switch between three possible foil models, keeping all other things equal, by adjusting the control parameter ϱ:

1. Non-detachable modal beam top foil – linear discrete bump force ($\varrho = -\infty$).
2. Detachable modal beam top foil – bilinear discrete bump force ($\varrho = 0$).
3. Detachable modal beam top foil – smoothed bilinear discrete bump force (ϱ a small positive number).

$\mathbf{f}_{\mathrm{sm}} = \mathbf{0}$ (eqs. (13), (15), (16)) for conditions 1, 2. Model 1 allows only contact state A listed above. Model 2 allows states A and B. Model 3 introduces the additional state C ("marginal" contact) for an individual bump, and smoothing is applied for this state, as illustrated in Figure 3. In eq. (16a) and Figure 3, the smoothing of the reaction force of a bump in contact state C is done on the basis of the top foil deflection at its location only, which is by far the dominant influence. The smoothing is not strictly exact if $\mathbf{C}_{\mathrm{b}}$ has cross-coupling terms, but introducing displacements at other locations into the smoothing will result in an unnecessary over-complication. Moreover, the diagonal terms $C_{\mathrm{b}_{n,n}}$ can be based on the whole bump foil structure (rather than a single bump in isolation as typically done in SEFM [17]), thereby retaining some of the cross-coupling effect.

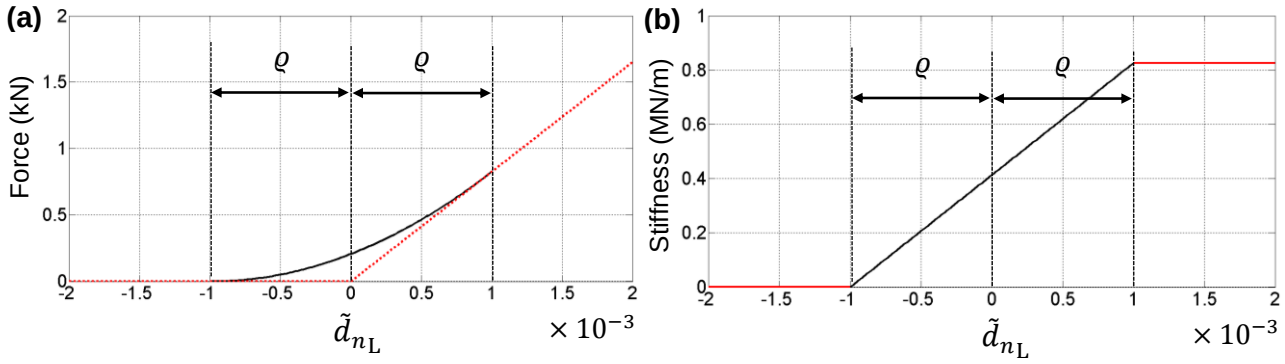

Figure 3. Illustration of smoothing of bilinear effect at bump no. n where top foil is in a state of "marginal" contact i.e. $|\tilde{d}_{n_L}| < \varrho$, where $\tilde{d}_{n_L} = d_{n_L}/c$ is the non-dimensional deflection of the top foil at the angular position of the apex of the bump and ϱ is a small positive number: (a) elastic component of bump reaction (black solid line – smoothed; red dotted line – unsmoothed); (b) effective smoothed stiffness at bump apex.

2.3 Air Film Equations (eqs. (2a,c))

Equations (2a,c) are obtained by using the FD method to discretise the RE, as described in [2, 3]. The RE is formulated in terms of the combined state variable $\psi \equiv \tilde{p}\tilde{h}$ where $\tilde{p}$ and $\tilde{h}$ are the non-dimensional air film pressure and thickness at a position (ξ, θ). The FD grid has $N_z \times N_\theta$ points spaced by $\Delta\xi$, $\Delta\theta$ in the axial and angular directions respectively, where $\xi = \xi_i$, $i = 1, \ldots, N_z$ and $\theta = \theta_j$, $j = 1, \ldots, N_\theta$. Hence, in eqs. (2a,c), $\boldsymbol{\psi}_{\mathrm{L,R}}$ are the $N_z N_\theta \times 1$ vectors of variables $\psi_{i,j_{\mathrm{L,R}}} = \psi_{\mathrm{L,R}}(\xi_i, \theta_j, \tau)$. In the ξ direction the grid extends from $\xi_1 = \Delta\xi$ to $\xi_{N_z} = 0.5L/R$ i.e. covers only half the axial length due to symmetry. The edges of the pad are excluded from the grid since they are at atmospheric pressure. The extent of the grid in the θ direction therefore depends on whether or not a pressure constraint of $p = p_{\mathrm{a}}$ is applied at the location of the weld ($\theta = \pi/2, 5\pi/2$ i.e. the location of the leading/trailing edges):

i. If $p = p_{\mathrm{a}}$ condition is applied at weld, the grid extends from $\theta_1 = \pi/2 + \Delta\theta$ to $\theta_{N_\theta} = 5\pi/2 - \Delta\theta$.

ii. If no pressure condition is applied at weld, the grid extends from $\theta_1 = \pi/2$ to $\theta_{N_\theta} = 5\pi/2 - \Delta\theta$.

Dispensing with the subscripts "L" and "R" for clarity, the boundary conditions in the θ direction corresponding to the above two cases are as follows.

For case (i), the boundary condition is the same as that in eq. (17c,d) of reference [3]:

$$\psi_{i,N_\theta+1} = \tilde{h}(\theta = 5\pi/2)\ ,\ \psi_{i,0} = \tilde{h}(\theta = \pi/2) \qquad (17a,b)$$

For case (ii), a periodicity condition is applied to the pressure:

$$\tilde{p}_{i,N_\theta+1} = \tilde{p}_{i,1}\ ,\ \tilde{p}_{i,0} = \tilde{p}_{i,N_\theta} \tag{18a,b}$$

Since the state variable of the RE is ψ ($\equiv \tilde{p}\tilde{h}$) rather than $\tilde{p}$, the boundary condition (18a,b) is applied in the following form:

$$\psi_{i,N_\theta+1} = \frac{\psi_{i,1}}{\tilde{h}(\theta = \theta_1)}\tilde{h}(\theta = 5\pi/2), \qquad \psi_{i,0} = \frac{\psi_{i,N_\theta}}{\tilde{h}\left(\theta = \theta_{N_\theta}\right)}\tilde{h}(\theta = \pi/2 - \Delta\theta) \tag{19a,b}$$

In the above, the film thickness $\tilde{h}$ is a function of θ and is given by

$$\tilde{h}(\theta) = 1 - \boldsymbol{\varepsilon}^{\mathrm{T}}\begin{bmatrix}\cos\theta \\ \sin\theta\end{bmatrix} + \widetilde{w}(\theta) \tag{20}$$

where $\widetilde{w}$ is the non-dimensional radial deflection of the top foil. In the case of eq. (19b), the value of $\widetilde{w}(\theta = \pi/2 - \Delta\theta)$ needed for $\tilde{h}(\theta = \pi/2 - \Delta\theta)$ is determined by extrapolating backward from $\theta = \pi/2$. This is because periodicity does not apply to the top foil deflection. It is for this reason that the pressure periodicity condition in eq. (19a,b) is somewhat different from the ψ periodicity condition of eq. (22a,b) in reference [3]. In the case of [3], periodicity in pressure could be considered to mean periodicity in ψ since $\widetilde{w}$ in [3] was based entirely on the bump foil (top foil effect ignored).

3. COMPUTATION

Section 3.1 summarises the static equilibrium, stability and modal analysis (SESMA) scheme which is applied unaltered to the cases studied in this paper (section 4). Section 3.2 presents expressions for the required Jacobian. As in [3], transient nonlinear dynamic analysis (TNDA) of eq. (1), using the implicit time domain integrator *ode23s* in *Matlab*, is applied where needed.

3.1 SESMA [3]

The first stage of SESMA involves the determination of the static equilibrium condition $\mathbf{s} = \mathbf{s}_{\mathrm{E}}$ at any fixed speed Ω by setting $\mathbf{s}' = \mathbf{0}$ for $\mathbf{f_u} = \mathbf{0}$ in eq. (1) and using an iterative process to solve the resulting set of nonlinear algebraic equations [3]:

$$\boldsymbol{\chi}(0, \mathbf{s})|_{\mathbf{f_u}=\mathbf{0}} = \mathbf{0} \tag{21}$$

The second stage of SESMA involves the stability and modal characteristics of free perturbations $\boldsymbol{\Delta s}$ about $\mathbf{s} = \mathbf{s_E}$, which are governed by the linearisation of the dynamical system (eq. (1)):

$$(\boldsymbol{\Delta s})' = \mathbf{J}(\boldsymbol{\Delta s}) \tag{22}$$

where the Jacobian $\mathbf{J}$ used in this stage is computed at the state $\mathbf{s} = \mathbf{s}_\mathrm{E}$:

$$\mathbf{J} = \left.\frac{\boldsymbol{\partial \chi}}{\boldsymbol{\partial s}}\right|_{\mathbf{f}_\mathrm{u}=\mathbf{0},\mathbf{s}=\mathbf{s}_\mathrm{E}} \tag{23}$$

The eigenvalue analysis of the matrix $\mathbf{J}$ at each given speed Ω yields N_s eigenvalues that comprise N_e real eigenvalues and N_o pairs of complex conjugate eigenvalues $\lambda_{n,\mathrm{Re}} \pm \mathrm{j}\lambda_{n,\mathrm{Im}}$, $\lambda_{n,\mathrm{Im}} > 0$ $(n = 1 \ldots N_\mathrm{o})$. The complex conjugate eigenvalues have associated conjugate eigenvectors $\boldsymbol{\rho}^{(n)}$, $\boldsymbol{\rho}^{(n)*}$. The *oscillatory* part of the general solution of eq. (22) is:

$$\boldsymbol{\Delta s} = \sum_{n=1}^{N_\mathrm{o}} c_n \mathrm{e}^{-\zeta_n \varpi_{\mathrm{u},n} t} \mathrm{mod}\{\boldsymbol{\rho}^{(n)}\} .* \cos\left(\varpi_{\mathrm{d},n} t + \arg\{\boldsymbol{\rho}^{(n)}\} + \alpha_n\right) \tag{24}$$

In eq. (24): c_n, α_n are arbitrary real scalar constants; $\mathrm{mod}\{\boldsymbol{\upsilon}\}$, $\arg\{\boldsymbol{\upsilon}\}$ respectively denote the vectors of moduli and phases of the complex elements of vector $\boldsymbol{\upsilon}$; $\mathbf{a}.*\mathbf{b}$ denotes a vector containing the products of corresponding elements of two vectors $\mathbf{a}$, $\mathbf{b}$; $\varpi_{\mathrm{d},n}$, ζ_n, $\varpi_{\mathrm{u},n}$ are, respectively, the damped natural circular frequency, viscous damping ratio, and the undamped natural circular frequency of (oscillatory) mode no. n:

$$\varpi_{\mathrm{d},n} = \Omega\lambda_{n,\mathrm{Im}}/2,\ \zeta_n = -\lambda_{n,\mathrm{Re}}/\left(\lambda_{n,\mathrm{Re}}^2 + \varpi_{\mathrm{d},n}^2\right)^{0.5},\ \varpi_{\mathrm{u},n} = \varpi_{\mathrm{d},n}/(1-\zeta_n^2)^{0.5} \tag{25a-c}$$

A filtering criterion is applied to extract only those modes that involve significant vibration (whirl) of the rotor (thus extracting the Campbell diagram from the unfiltered eigenfrequency *vs* speed map). This is based on a comparison of the journal vibration with the foil vibration for each mode no. n $(n = 1 \ldots N_\mathrm{o})$ at each given speed Ω. It is efficiently implemented by appropriately scaling the eigenvectors $\boldsymbol{\rho}^{(n)}$ and then setting a minimum journal amplitude.

For each eigenvector $\boldsymbol{\rho}^{(n)}$ $(n = 1 \ldots N_\mathrm{o})$, the scaling factor $\kappa^{(n)}$ is chosen to be:

$$\kappa^{(n)} = \sigma / \tilde{A}^{(n)} \tag{26}$$

where σ is a prescribed fraction of the radial clearance c and $\tilde{A}^{(n)}$ is the overall greatest non-dimensional vibration amplitude within the two FABs:

$$\tilde{A}^{(n)} = \max\left(\mathrm{mod}\left\{\boldsymbol{\rho}_{\boldsymbol{\varepsilon}_{\mathrm{L}}}^{(n)}\right\}, \mathrm{mod}\left\{\boldsymbol{\rho}_{\tilde{\mathbf{w}}_{\mathrm{L}}}^{(n)}\right\}, \mathrm{mod}\left\{\boldsymbol{\rho}_{\boldsymbol{\varepsilon}_{\mathrm{R}}}^{(n)}\right\}, \mathrm{mod}\left\{\boldsymbol{\rho}_{\tilde{\mathbf{w}}_{\mathrm{R}}}^{(n)}\right\}\right) \tag{27}$$

In eq. (27), from eqs. (5), (8):

$$\boldsymbol{\rho}_{\boldsymbol{\varepsilon}_{\mathrm{L,R}}}^{(n)} = \mathbf{H}_{\mathbf{f}_{\mathrm{J_{L,R}}}} \boldsymbol{\rho}_{\mathbf{q}}^{(n)} / c \tag{28}$$

$$\boldsymbol{\rho}_{\tilde{\mathbf{w}}_{\mathrm{L,R}}}^{(n)} = \mathbf{T}_{\mathrm{F}} \boldsymbol{\rho}_{\mathbf{s}_{\mathrm{F_{L,R}}}}^{(n)} \tag{29}$$

where $\boldsymbol{\rho}_{\mathbf{q}}^{(n)}$, $\boldsymbol{\rho}_{\mathbf{s}_{\mathrm{F_{L,R}}}}^{(n)}$ are sub-vectors of $\boldsymbol{\rho}^{(n)}$ in accordance to the partitioning of state-vector $\mathbf{s}$ (eq. (3)). The scaled eigenvectors are denoted by $\tilde{\rho}^{(n)}$ where

$$\tilde{\boldsymbol{\rho}}^{(n)} = \kappa^{(n)} \boldsymbol{\rho}^{(n)} \tag{30}$$

The scaled vibrations at the FABs are then given by:

$$\Delta\boldsymbol{\varepsilon}_{\mathrm{L,R}}^{(n)}(t) = \mathrm{e}^{-\zeta_n \varpi_{\mathrm{u},n} t} \mathrm{mod}\left\{\tilde{\boldsymbol{\rho}}_{\boldsymbol{\varepsilon}_{\mathrm{L,R}}}^{(n)}\right\} .* \cos\left(\varpi_{\mathrm{d},n} t + \arg\left\{\tilde{\boldsymbol{\rho}}_{\boldsymbol{\varepsilon}_{\mathrm{L,R}}}^{(n)}\right\} + \alpha_n\right) \tag{31}$$

$$\Delta\tilde{\mathbf{w}}_{\mathrm{L,R}}^{(n)}(t) = \mathrm{e}^{-\zeta_n \varpi_{\mathrm{u},n} t} \mathrm{mod}\left\{\tilde{\boldsymbol{\rho}}_{\tilde{\mathbf{w}}_{\mathrm{L,R}}}^{(n)}\right\} .* \cos\left(\varpi_{\mathrm{d},n} t + \arg\left\{\tilde{\boldsymbol{\rho}}_{\tilde{\mathbf{w}}_{\mathrm{L,R}}}^{(n)}\right\} + \alpha_n\right) \tag{32}$$

where $\tilde{\boldsymbol{\rho}}_{\boldsymbol{\varepsilon}_{\mathrm{L,R}}}^{(n)}$, $\tilde{\boldsymbol{\rho}}_{\tilde{\mathbf{w}}_{\mathrm{L,R}}}^{(n)}$ are derived from eqs. (28), (29) using scaled eigenvectors and yield $\tilde{A}^{(n)} = \sigma$ when used in eq. (27). The minimum journal amplitude filtering criterion is then:

$$\left(\tilde{A}_{\boldsymbol{\varepsilon}_{\mathrm{L}}}^{(n)} > C\sigma\right) \mathrm{OR} \left(\tilde{A}_{\boldsymbol{\varepsilon}_{\mathrm{R}}}^{(n)} > C\sigma\right) \tag{33}$$

where:

- $\tilde{\tilde{A}}_{\boldsymbol{\varepsilon}_\mathrm{L}}^{(n)}$, $\tilde{\tilde{A}}_{\boldsymbol{\varepsilon}_\mathrm{R}}^{(n)}$ denote the means of the *x*, *y* non-dimensional scaled vibration amplitudes of the journals of the two FABs respectively i.e. $\tilde{\tilde{A}}_{\boldsymbol{\varepsilon}_{\mathrm{L,R}}}^{(n)} = \mathrm{mean}\left(\mathrm{mod}\left\{\tilde{\tilde{\boldsymbol{\rho}}}_{\boldsymbol{\varepsilon}_{\mathrm{L,R}}}^{(n)}\right\}\right)$;
- C is a prescribed cut-off threshold factor.

In this work, $\sigma = 0.2$ and $C = 0.1$ i.e. the mode is scaled so that the overall greatest non-dimensional vibration at the FABs (considering both foil and journal vibration) is 20% of the radial clearance, and it is then rejected unless the journal vibration of at least one of the FABs exceeds 2% of the radial clearance. Any modes that manage to pass this criterion but are still dominated by pad vibration typically have a high damping ratio [3]. Such rogue modes of little practical significance can be filtered out by applying a *maximum modal damping* criterion in conjunction with eq. (33) [3].

Any specific eigenmode can be verified by TNDA of the nonlinear system (eq. (1), with no unbalance excitation) using initial conditions that induce it to respond in that specific mode *only* in the vicinity of the state $\mathbf{s} = \mathbf{s}_\mathrm{E}$:

$$\mathbf{s}(\tau = 0) = \mathbf{s}_\mathrm{E} + c_n \mathrm{mod}\left\{\tilde{\tilde{\boldsymbol{\rho}}}^{(n)}\right\} .* \cos\left(\arg\left\{\tilde{\tilde{\boldsymbol{\rho}}}^{(n)}\right\} + \alpha_n\right) \tag{34}$$

In eq. (34), c_n is a reduction factor that converts the scaled mode to a suitably small TNDA perturbation.

3.2 Jacobian

The Jacobian of the dynamical system (eq. (1)) is required for TNDA and the two stages of SESMA. A part-analytical expression is used to compute it, to make TNDA feasible and SESMA more efficient and accurate [3]. The expression used here is obtained by adapting the expression in [3] to account for the present foil model, and considering identical bearings, each single pad with FD grid of dimension N_z by N_θ.

The Jacobian is written as

$$\frac{\partial \boldsymbol{\chi}}{\partial \mathbf{s}} = \left[\frac{\partial \boldsymbol{\chi}}{\partial\left[\boldsymbol{\psi}_\mathrm{L}^\mathrm{T} \quad \mathbf{s}_{\mathrm{F_L}}^\mathrm{T}\right]^\mathrm{T}} \quad \frac{\partial \boldsymbol{\chi}}{\partial\left[\boldsymbol{\psi}_\mathrm{R}^\mathrm{T} \quad \mathbf{s}_{\mathrm{F_R}}^\mathrm{T}\right]^\mathrm{T}} \quad \frac{\partial \boldsymbol{\chi}}{\partial \mathbf{q}} \quad \frac{\partial \boldsymbol{\chi}}{\partial \mathbf{q}'}\right] \tag{35}$$

The sub-matrices in eq. (35) are given by the expressions below, where $\mathbf{0}_{m\times n}$ denotes an $m \times n$ matrix of zeros, $\mathbf{I}_{m\times m}$ denotes an m-square identity matrix, and all other notation was defined in section 2.

$$\frac{\partial \boldsymbol{\chi}}{\partial\left[\boldsymbol{\psi}_{\mathrm{L}}^{\mathrm{T}} \quad \mathbf{s}_{\mathrm{F_L}}^{\mathrm{T}}\right]^{\mathrm{T}}} = \begin{bmatrix} \frac{\partial \mathbf{g}_{\mathrm{RE_L}}}{\partial \boldsymbol{\psi}_{\mathrm{L}}} & \frac{\partial \mathbf{g}_{\mathrm{RE_L}}}{\partial \tilde{\mathbf{w}}_{\mathrm{L}}}\mathbf{T}_{\mathrm{F}} \\ \frac{\partial \mathbf{g}_{\mathrm{Foil_L}}}{\partial \boldsymbol{\psi}_{\mathrm{L}}} & \frac{\partial \mathbf{g}_{\mathrm{Foil_L}}}{\partial \mathbf{s}_{\mathrm{F_L}}} \\ \mathbf{0}_{N_{\mathrm{z}}N_\theta \times N_{\mathrm{z}}N_\theta} & \mathbf{0}_{N_{\mathrm{z}}N_\theta \times 2H_{\mathbf{F}}} \\ \mathbf{0}_{2H_{\mathbf{F}} \times N_{\mathrm{z}}N_\theta} & \mathbf{0}_{2H_{\mathbf{F}} \times 2H_{\mathbf{F}}} \\ \mathbf{0}_{H \times N_{\mathrm{z}}N_\theta} & \mathbf{0}_{H \times 2H_{\mathbf{F}}} \\ \frac{4}{\Omega^2}\mathbf{H}_{\mathbf{f}_{\mathrm{J_L}}}^{\mathrm{T}}\frac{\partial \mathbf{f}_{\mathrm{J_L}}}{\partial \boldsymbol{\psi}_{\mathrm{L}}} & \frac{4}{\Omega^2}\mathbf{H}_{\mathbf{f}_{\mathrm{J_L}}}^{\mathrm{T}}\frac{\partial \mathbf{f}_{\mathrm{J_L}}}{\partial \tilde{\mathbf{w}}_{\mathrm{L}}}\mathbf{T}_{\mathrm{F}} \end{bmatrix} \tag{36}$$

$$\frac{\partial \boldsymbol{\chi}}{\partial\left[\boldsymbol{\psi}_{\mathrm{R}}^{\mathrm{T}} \quad \mathbf{s}_{\mathrm{F_R}}^{\mathrm{T}}\right]^{\mathrm{T}}} = \begin{bmatrix} \mathbf{0}_{N_{\mathrm{z}}N_\theta \times N_{\mathrm{z}}N_\theta} & \mathbf{0}_{N_{\mathrm{z}}N_\theta \times 2H_{\mathbf{F}}} \\ \mathbf{0}_{2H_{\mathbf{F}} \times N_{\mathrm{z}}N_\theta} & \mathbf{0}_{2H_{\mathbf{F}} \times 2H_{\mathbf{F}}} \\ \frac{\partial \mathbf{g}_{\mathrm{RE_R}}}{\partial \boldsymbol{\psi}_{\mathrm{R}}} & \frac{\partial \mathbf{g}_{\mathrm{RE_R}}}{\partial \tilde{\mathbf{w}}_{\mathrm{R}}}\mathbf{T}_{\mathrm{F}} \\ \frac{\partial \mathbf{g}_{\mathrm{Foil_R}}}{\partial \boldsymbol{\psi}_{\mathrm{R}}} & \frac{\partial \mathbf{g}_{\mathrm{Foil_R}}}{\partial \mathbf{s}_{\mathrm{F_R}}} \\ \mathbf{0}_{H \times N_{\mathrm{z}}N_\theta} & \mathbf{0}_{H \times 2H_{\mathbf{F}}} \\ \frac{4}{\Omega^2}\mathbf{H}_{\mathbf{f}_{\mathrm{J_R}}}^{\mathrm{T}}\frac{\partial \mathbf{f}_{\mathrm{J_R}}}{\partial \boldsymbol{\psi}_{\mathrm{R}}} & \frac{4}{\Omega^2}\mathbf{H}_{\mathbf{f}_{\mathrm{J_R}}}^{\mathrm{T}}\frac{\partial \mathbf{f}_{\mathrm{J_R}}}{\partial \tilde{\mathbf{w}}_{\mathrm{R}}}\mathbf{T}_{\mathrm{F}} \end{bmatrix} \tag{37}$$

$$\frac{\partial \boldsymbol{\chi}}{\partial \mathbf{q}} = \begin{bmatrix} \frac{\partial \mathbf{g}_{\mathrm{RE_L}}}{\partial \boldsymbol{\varepsilon}_{\mathrm{L}}}\mathbf{H}_{\mathbf{f}_{\mathrm{J_L}}} \\ \frac{\partial \mathbf{g}_{\mathrm{Foil_L}}}{\partial \boldsymbol{\varepsilon}_{\mathrm{L}}}\mathbf{H}_{\mathbf{f}_{\mathrm{J_L}}} \\ \frac{\partial \mathbf{g}_{\mathrm{RE_R}}}{\partial \boldsymbol{\varepsilon}_{\mathrm{R}}}\mathbf{H}_{\mathbf{f}_{\mathrm{J_R}}} \\ \frac{\partial \mathbf{g}_{\mathrm{Foil_R}}}{\partial \boldsymbol{\varepsilon}_{\mathrm{R}}}\mathbf{H}_{\mathbf{f}_{\mathrm{J_R}}} \\ \mathbf{0}_{H\times H} \\ \frac{4}{\Omega^2}\left[\mathbf{H}_{\mathbf{f}_{\mathrm{J_L}}}^{\mathrm{T}}\frac{\partial \mathbf{f}_{\mathrm{J_L}}}{\partial \boldsymbol{\varepsilon}_{\mathrm{L}}}\mathbf{H}_{\mathbf{f}_{\mathrm{J_L}}} + \mathbf{H}_{\mathbf{f}_{\mathrm{J_R}}}^{\mathrm{T}}\frac{\partial \mathbf{f}_{\mathrm{J_R}}}{\partial \boldsymbol{\varepsilon}_{\mathrm{R}}}\mathbf{H}_{\mathbf{f}_{\mathrm{J_R}}} - \boldsymbol{\Lambda}\right] \end{bmatrix} \qquad \frac{\partial \boldsymbol{\chi}}{\partial \mathbf{q}'} = \begin{bmatrix} \mathbf{0}_{N_{\mathrm{z}}N_\theta \times H} \\ \mathbf{0}_{2H_{\mathbf{F}} \times H} \\ \mathbf{0}_{N_{\mathrm{z}}N_\theta \times H} \\ \mathbf{0}_{2H_{\mathbf{F}} \times H} \\ \mathbf{I}_{H\times H} \\ \frac{2}{\Omega}\mathbf{H}_{\mathbf{g}}^{\mathrm{T}}\mathbf{P}\mathbf{H}_{\boldsymbol{\alpha}} \end{bmatrix} \tag{38, 39}$$

In the above expressions, taking FAB "L" as an example, the foil domain Jacobian sub-matrices are given as follows:

$$\frac{\partial \mathbf{g}_{\mathrm{Foil_L}}}{\partial \boldsymbol{\psi}_{\mathrm{L}}} = \begin{bmatrix} \mathbf{0}_{H_{\mathbf{F}} \times N_{\mathrm{z}}N_\theta} \\ \frac{4}{\Omega^2}\mathbf{H}_{\mathbf{d}}^{\mathrm{T}}\frac{\partial \mathbf{f}_{\mathrm{p_L}}}{\partial \boldsymbol{\psi}_{\mathrm{L}}} \end{bmatrix} \tag{40a}$$

$$\frac{\partial \mathbf{g}_{\mathrm{Foil_L}}}{\partial \mathbf{s}_{\mathrm{F_L}}} = \begin{bmatrix} \mathbf{0}_{H_{\mathbf{F}} \times H_{\mathbf{F}}} & \mathbf{I}_{H_{\mathbf{F}} \times H_{\mathbf{F}}} \\ -\frac{4}{\Omega^2}\boldsymbol{\Lambda}_{\mathrm{F}} & -\frac{2}{\Omega}\mathbf{D}_{\mathrm{F}} \end{bmatrix} + \begin{bmatrix} \mathbf{0}_{H_{\mathbf{F}} \times 2H_{\mathbf{F}}} \\ \frac{4}{\Omega^2}\mathbf{H}_{\mathbf{d}}^{\mathrm{T}}\frac{\partial \mathbf{f}_{\mathrm{p_L}}}{\partial \tilde{\mathbf{w}}_{\mathrm{L}}}\mathbf{T}_{\mathrm{F}} - \frac{4}{c\Omega^2}\mathbf{H}_{\mathbf{d}}^{\mathrm{T}}\begin{bmatrix} \frac{\mathbf{f}_{\mathrm{b_L}}}{\partial \tilde{\mathbf{d}}_{\mathrm{L}}}\mathbf{H}_{\mathbf{d}} & \frac{\mathbf{f}_{\mathrm{b_L}}}{\partial \tilde{\mathbf{d}}'_{\mathrm{L}}}\mathbf{H}_{\mathbf{d}} \end{bmatrix} \end{bmatrix} \tag{40b}$$

$$\frac{\partial \mathbf{g}_{\mathrm{Foil_L}}}{\partial \boldsymbol{\varepsilon}_{\mathrm{L}}} = \begin{bmatrix} \mathbf{0}_{H_{\mathbf{F}} \times 2} \\ \dfrac{4}{\Omega^2} \mathbf{H}_{\mathbf{d}}^{\mathrm{T}} \dfrac{\partial \mathbf{f}_{\mathrm{p_L}}}{\partial \boldsymbol{\varepsilon}_{\mathrm{L}}} \end{bmatrix} \tag{40c}$$

As in [3], the FD method establishes functional expressions for $\mathbf{g}_{\mathrm{RE_L}}$, $\mathbf{f}_{\mathrm{J_L}}$, $\mathbf{f}_{\mathrm{p_L}}$, each in terms of ($\boldsymbol{\psi}_{\mathrm{L}}$, $\widetilde{\mathbf{w}}_{\mathrm{L}}$, $\boldsymbol{\varepsilon}_{\mathrm{L}}$), and the *Symbolic Math Toolbox*™ is used to derive symbolic expressions for the Jacobians of these functions with respect to $\boldsymbol{\psi}_{\mathrm{L}}$, $\widetilde{\mathbf{w}}_{\mathrm{L}}$, $\boldsymbol{\varepsilon}_{\mathrm{L}}$ (see section 3.1 of [3] for more detail). Additionally, in the present case, the expressions for the Jacobians of $\mathbf{f}_{\mathrm{b_L}}$ with respect to $\tilde{\mathbf{d}}_{\mathrm{L}}$, $\tilde{\mathbf{d}}'_{\mathrm{L}}$ (eq. (40b)) are readily determined from eqs. (13), (15) and (16).

4. APPLICATION TO SYMMETRIC ROTOR-FAB SYSTEM: RESULTS AND DISCUSSION

The generic system in Figure 1a is specialised to a symmetric rigid rotor of total mass M_{tot} supported on two identical single-pad bump-type FABs (Figure 1b) mounted in a rigid support structure. The total number of rotor component modes is $H = 2$, comprising one purely translational mode at 0 Hz defined by $\varphi_{\mathrm{trans}}(z) = 1/\sqrt{M_{\mathrm{tot}}}$ in each of the *xz* and *yz* planes. Hence, in eq. (2e), the non-zero matrices are:

$$\mathbf{H}_{\mathbf{f}_{\mathrm{J_{L,R}}}} = \begin{bmatrix} 1/\sqrt{M_{\mathrm{tot}}} & 0 \\ 0 & 1/\sqrt{M_{\mathrm{tot}}} \end{bmatrix}, \mathbf{H}_{\mathbf{f}_{\mathrm{s}}} = \begin{bmatrix} 0 & 1/\sqrt{M_{\mathrm{tot}}} \end{bmatrix} \tag{41a,b}$$

Although dynamic symmetry allows reduction of the problem (by considering $M_{\mathrm{tot}}/2$ supported by only one bearing, as done in [15]), this was not done here in order to get a better idea of the computational burden involved in more practical scenarios.

The parameters of the system are presented in Table 1. The rotor and air film parameters are as in [10, 15] and negligibly different from [17, 16]. To align with the *continuously distributed* compliance (i.e. SEFM) used in previous linear or bilinear bump foil models, the discrete compliance matrix $\mathbf{C}_{\mathrm{b}}$ (Table 1) is a diagonal matrix (no elastic cross-coupling) and the direct stiffness K_{b} is chosen so that the equivalent stiffness per unit area $K_{\mathrm{b}}/(SL) = 4.739$ GN/m^3 with the pitch S taken to be 4.572 mm [17, 22, 26]. This is the stiffness per unit area used in the model of [10, 15] (SEFM bump foil, top foil ignored) and is only 2% different from that of the Nielsen and Santos model [17] (detachable modal shell top foil – bilinear

SEFM bump foil). It is noted that eq. (12b) is based on the exact pitch ($2\pi R/N_\mathrm{b} = 4.604$ mm) and this further reduces the difference from [17] to 1.4%. The top foil parameters are identical to those used in [17]. The top foil was modelled as a curved beam in *ANSYS* FE software using 400 elements of type *BEAM188*. It was clamped at either the trailing edge or leading edge, depending on the configuration studied. The first 50 modal frequencies of the top foil ranged from 24.5 Hz (mode 1) through to 11.9 kHz (mode 20), through to 69 kHz (mode 50). A mesh convergence study showed that these 50 frequencies changed by less than 5% when the number of elements was decreased from 400 to 200.

In line with previous works (e.g. [4, 10, 14]), the FD grid size $N_\mathrm{z} \times N_\theta$ (covering half the axial length of each FAB, excluding open end) was either 7×71 if the pressure constraint $p = p_\mathrm{a}$ was applied at weld, and 7×72 otherwise (section 2.3). The accuracy of this grid size is supported by mesh convergence studies in [10, 14] for a FAB of identical geometry and reconfirmed for use with the present foil model. Unless otherwise stated, the number of top foil component modes $H_\mathrm{F} = 20$.

Table 1. System parameters ($\mathbf{I}_{N_\mathrm{b}\times N_\mathrm{b}}$ is an identity matrix of size $N_\mathrm{b} \times N_\mathrm{b}$).

Rotor [10, 15]	
symmetric rigid, total mass $M_\mathrm{tot} = 2 \times 3.061$ kg	
Air film (either bearing) [10, 15]	
radial clearance c ($\times 10^{-6}$ m)	32
viscosity (Pa·s)	1.95×10^{-5}
atmospheric pressure p_a (Pa)	101325
Bump foil (either bearing)	
number of bumps N_b	26 [26]
θ at first bump apex i.e. θ_{b_1} (rad)	$7\pi/13$
assumed inertia-less compliance matrix $\mathbf{C}_\mathrm{b}$	$\mathbf{I}_{N_\mathrm{b}\times N_\mathrm{b}}/K_\mathrm{b}$ where $K_\mathrm{b} = 0.8255 \times 10^6$ N/m
hysteretic damping loss factor η	0.25 [15, 17]
Top foil (either bearing) [17]	
inner radius R, length L , thickness ($\times 10^{-3}$ m)	19.05, 38.1, 0.2032
Young Modulus (GPa), density (kg/m^3)	207, 8280
θ at leading, trailing edges (rad)	$\pi/2$, $5\pi/2$
modal damping ratio (used in $\mathbf{D}_\mathrm{F}$, eq. (10))	0.005

4.1 Non-detachable modal beam top foil – linear discrete bump force

In this section a no-detachment condition is imposed by setting $\varrho = -\infty$. The results are obtained for three alternative conditions:

1. $p = p_a$ at weld *and* Gümbel;
2. $p = p_a$ at weld;
3. No pressure constraint.

As already mentioned, the Gümbel condition is an assumed correction (to non-detachment models) that caters for top foil detachment, and is only used in this sub-section. To be consistent with previous works [3, 13], it is applied by truncating p below $p = p_a$ when integrating for the air film forces on the journal (eq. (4)), but not when integrating for the air film forces on the top foil (eq. (12b)).

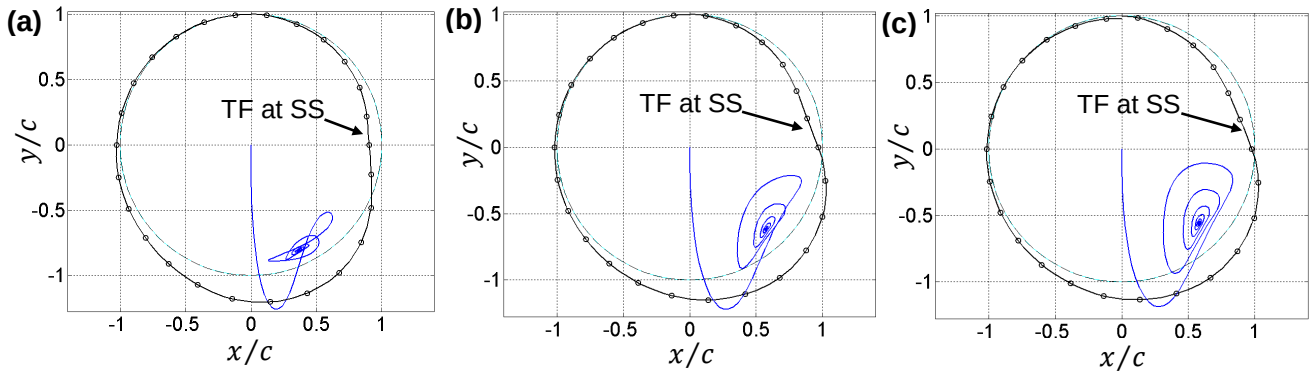

Figure 4. TNDA result at 12 krpm and zero rotor unbalance for a symmetric rotor-FAB system with single-pad FABs showing the journal trajectory from default initial conditions, and deformed top foil (TF) at steady-state (SS), assuming modal beam top foil ($H_F = 20$) and linear discrete bump force ($\varrho = -\infty$ i.e. no detachment): (a) $p = p_a$ at weld *and* Gümbel; (b) $p = p_a$ at weld; (c) no pressure constraints (NB: TF locations at angular positions of bump apexes indicated by circles; results obtained with FLE/CTE, results for CLE/FTE virtually identical).

Figures 4a-c show the TNDA results at 12 krpm for the above three conditions, from default initial conditions (corresponding to $\boldsymbol{\varepsilon}_{L,R}$, $\boldsymbol{\varepsilon}'_{L,R} = 0$, $\tilde{\mathbf{w}}_{L,R} = 0$ and atmospheric pressure). These three alternative results are virtually identical to those obtained with SEFM bump foil (top foil ignored) and corresponding air film constraints, published in the following works: [15, 17] (for Figure 4a); [12] (for Figure 4b); [10]

(for Figure 4c). The results in Figure 4 were obtained for a free leading edge/clamped trailing edge (FLE/CTE) (evident in case of Figure 4c by zooming on weld area). The results are found to be virtually unchanged if the top foil is switched to clamped leading edge/free trailing edge (CLE/FTE), and this observation applies to all results of this sub-section, unless otherwise stated.

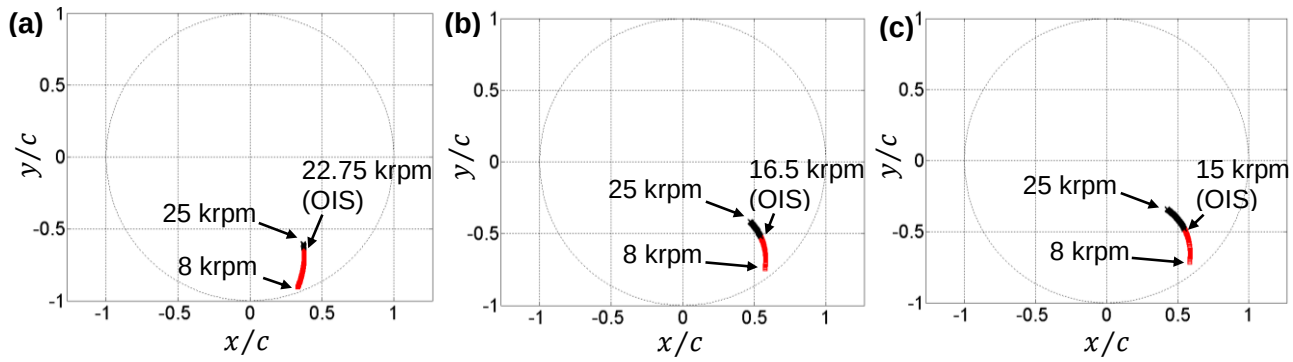

Figure 5. Loci of static equilibrium journal positions over a range of speeds for a symmetric rotor-FAB system with single-pad FABs assuming modal beam top foil ($H_F = 20$) and linear discrete bump force ($\varrho = -\infty$ i.e. no detachment): (a) $p = p_a$ at weld and Gümbel; (b) $p = p_a$ at weld; (c) no pressure constraints (NB: stable positions – red; unstable – black; OIS – onset of instability speed; results obtained with FLE/CTE, results for CLE/FTE virtually identical).

Figures 5a-c shows the loci of the static equilibrium positions (SEPs) of the journal for the speed range 8-25 krpm for the above three conditions. The OIS is defined as the first speed, in increments of 250 rpm, to register a negative damping ratio in one of the modes of vibration about the SEP. It is seen that the SEPs lift up, and the OIS reduces, as the air film constraints are progressively removed. The biggest change is caused by the removal of Gümbel. The subsequent removal of the weld location pressure constraint results in a further relatively small uplift of the SEPs and further small reduction in OIS. These observations are consistent with those reported in [2].

The free vibration (linearised) about the static equilibria in Figure 5a ($p = p_a$ at weld *and* Gümbel) is now considered. Figures 6a,b show the unfiltered eigenfrequency *vs* speed maps, for the CLE/FTE and FLE/CTE cases respectively. These maps are similar but with visible differences arising from the different fixing configurations of the top foil. Also, whereas the corresponding unfiltered eigenfrequency

map in [15] (Figure 4 in [15]) contains frequencies up to 600 Hz, the maps in Figure 6 go to higher frequencies due to the foil inertia, like the one by von Osmanski et al. [16]. It should also be noted that the high frequency modes in Figure 6a or 6b are different from those in the unfiltered map in [16] since the foil inertia is considered differently – in [16] it was added to the SEFM as a diagonal matrix of lumped masses, whereas in the present case the inertia is introduced via the component modes of the top foil.

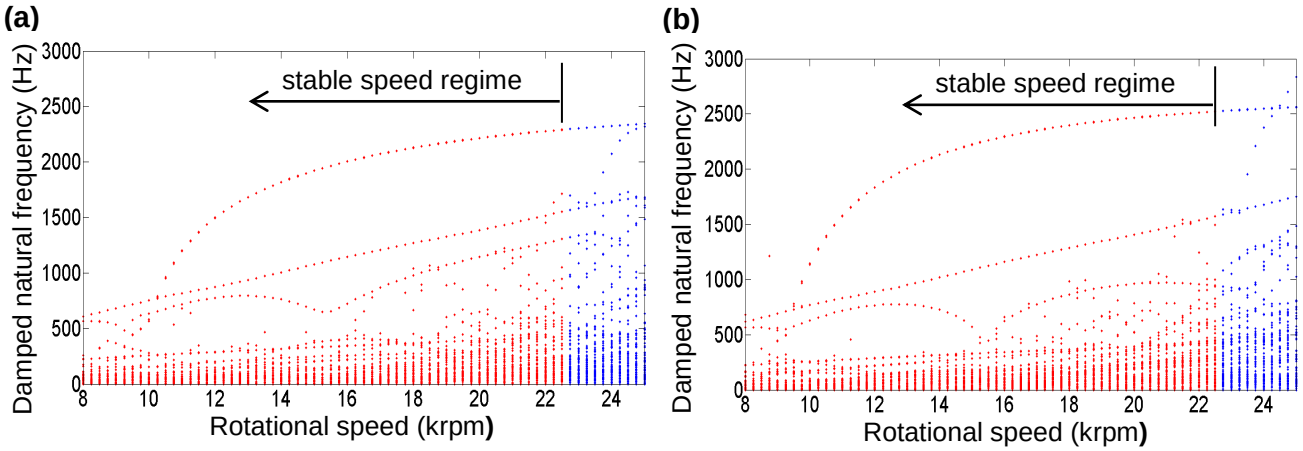

Figure 6. Unfiltered eigenfrequency $\varpi_{\mathrm{d},n}/(2\pi)$ *vs* speed map for a symmetric rotor-FAB system with single-pad FABs assuming modal beam top foil ($H_{\mathrm{F}} = 20$) and linear discrete bump force ($\varrho = -\infty$ i.e. no detachment) with $p = p_{\mathrm{a}}$ at weld and Gümbel: (a) CLE/FTE; (b) FLE/CTE.

Most of the eigenmodes in Figure 6a or 6b involve negligible journal vibration and will thus be rejected from the Campbell diagram. Figure 7 shows three examples of such reject modes. The 64.45 Hz mode in Figure 7a is similar to those already found in [15] (see Figure 6 of [15], where the "foil vibration" was simply the pressure-induced response of the continuously distributed compliance (SEFM)). The mode in Figure 7b has similar frequency (65.77 Hz) but is particular to the present system since it shows the vibration of the clamped-free top foil supported at the bumps (assumed not to detach in this sub-section). The high frequency mode in Figure 7c is clearly attributed to top foil inertia.

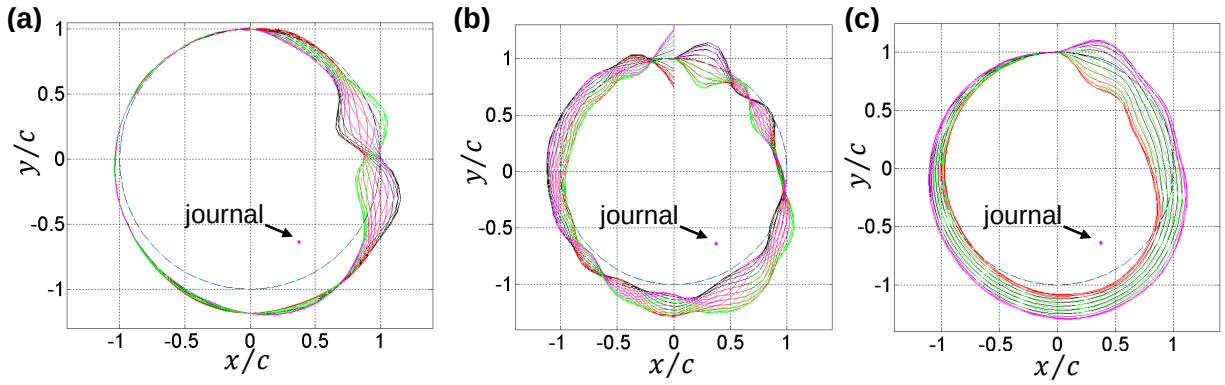

Figure 7. Three examples of modes in Figure 6b at 22 krpm that fail the minimum journal amplitude criterion, eq. (33): (a) $f_{\mathrm{d},n} = \varpi_{\mathrm{d},n}/(2\pi) = 64.45$ Hz, $\zeta_n = 0.99992$; (b) $f_{\mathrm{d},n} = 65.77$ Hz, $\zeta_n = 0.999997$; (c) $f_{\mathrm{d},n} = 2514.63$ Hz, $\zeta_n = 0.57288$ (NB for clarity of display, the exponential decay factor $\mathrm{e}^{-\zeta_n \varpi_{\mathrm{u},n} t}$ in eqs. (31), (32) was omitted when calculating the illustrated modal vibration – same applies for other figures showing eigenmodes).

The application of the minimum journal amplitude criterion to either Figure 6a or 6b results in identically the same Campbell diagram (Figure 8a). The extracted modes at individual speeds ("mode points") lie on two distinct curves. These curves are respectively (Campbell) mode nos. 1 and 2 of the system. The direction of whirl of each mode point is indicated (this is determined by computing eq. (31) at discrete times over the modal period). The Campbell diagram of Figure 8a agrees very closely with that in [15] (using SEFM and same air film conditions), with just a minor difference in OIS (22.75 krpm *vs* 22.25 krpm). The state of stability of each mode point in Figure 8a is governed by the sign of its modal damping ratio, which is plotted in Figure 8b. Reference [15] did not show the modal damping diagram, but the modal damping ratio curves in Figure 8b agree well with the corresponding ones computed in [16] despite the use of a different $\widetilde{\omega}_{\mathrm{ref}}$ (section 4.4).

The OIS of 22.75 krpm compares well with the OIS of ~20 krpm reported from the TNDA simulations with the bilinear model of Nielsen and Santos [17]. As already mentioned, the researchers in [17] demonstrated close agreement between their model and the SEFM-Gümbel model (although their demonstration was limited to a comparison of the respective TNDA journal trajectories at one speed). The variation of the frequency of mode 1 from 84 Hz at 8 krpm to 97 Hz at 20 krpm (Figure 8a) agrees

with the observation in [17] of a subharmonic frequency increasing "from approximately 80 Hz at 8,000 r/min to around 100 Hz at 20,000 r/min" (this frequency was clearly a natural mode since it appeared in the initial 0.22s of the TNDA response at low unbalance and was absent from the waterfall diagram of the steady-state vibration - see Figures 12, 13 in reference [17]). As observed in [15], mode 2 would not have featured in the unbalance response predictions of [17] since it is reverse whirl.

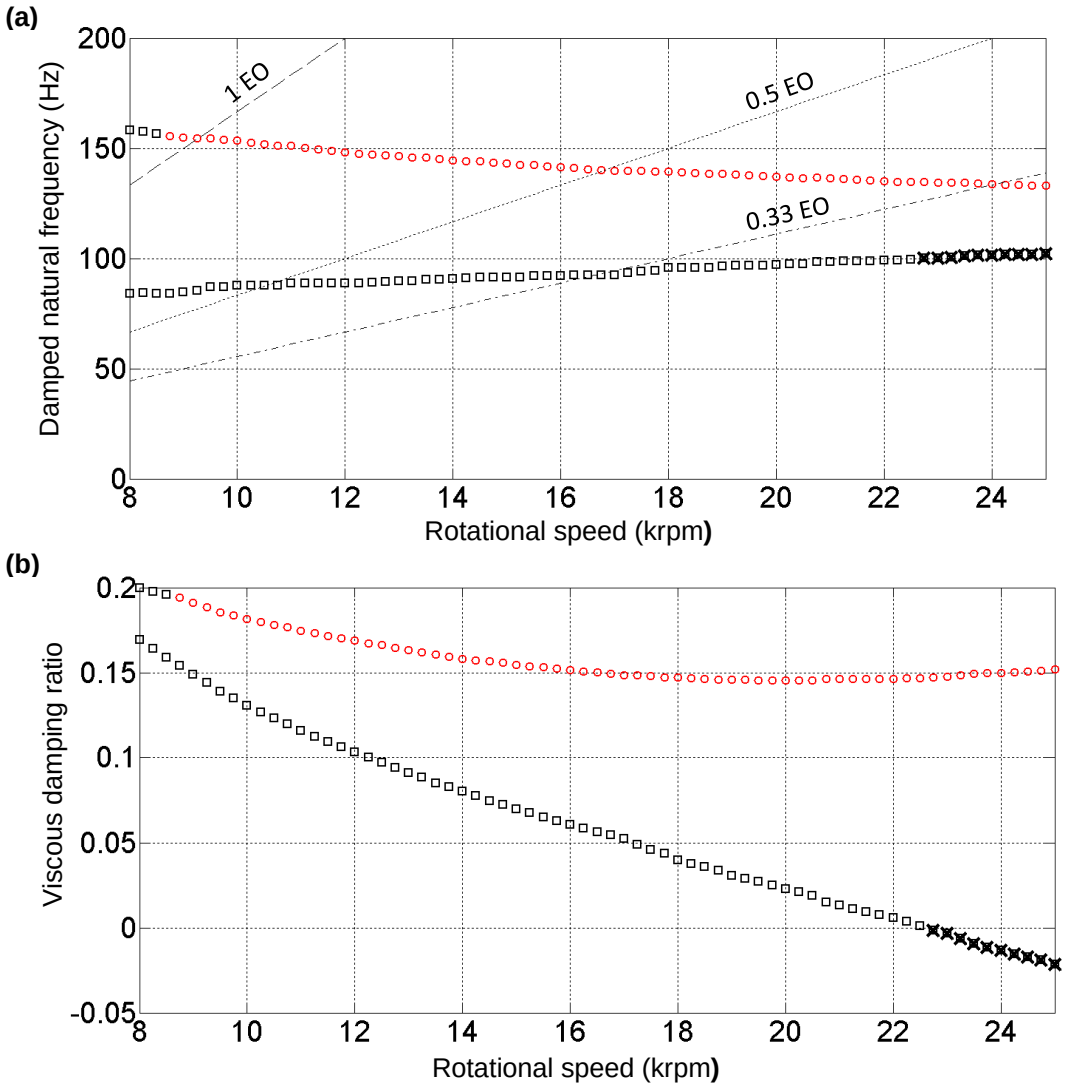

Figure 8. Campbell diagram (a) and associated modal damping diagram (b), for a symmetric rotor-FAB system with single-pad FABs assuming modal beam top foil ($H_F = 20$) and linear discrete bump force ($\varrho = -\infty$ i.e. no detachment) with $p = p_a$ at weld and Gümbel: forward whirl (black squares); reverse whirl (red circles); unstable mode points overlaid with a cross; EO (engine order) (NB: extracted using minimum journal amplitude criterion, eq. (33); identical results for CLE/FTE and FLE/CTE).

Figure 9 shows the Campbell modes at 22 krpm, which are essentially the same as the SEFM ones in [15] (the only significant difference is the damping ratio of mode 1, which is higher here than the corresponding result in Figure 7a of [15] since the speed considered is very close to the OIS, which has shifted slightly upward).

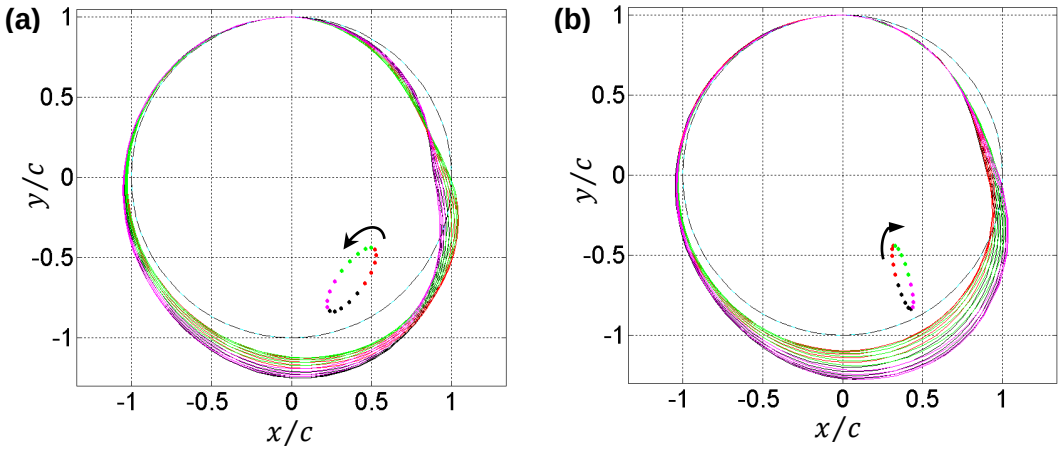

Figure 9. Modes at 22 krpm taken from Campbell diagram in Figure 8: (a) mode 1 ($f_{\mathrm{d},n} = 99.09$ Hz, $\zeta_n = 0.00565$, forward whirl); (c) mode 2 ($f_{\mathrm{d},n} = 135.13$ Hz, $\zeta_n = 0.14641$, reverse whirl) (NB: for readers of digital version, temporal sequence of vibration is indicated by colour sequence black-red-green-magenta – same applies for other figures showing eigenmodes).

.

The free vibration about the SEPs in Figure 5b ($p = p_{\mathrm{a}}$ at weld and no Gümbel) is next considered. Figure 10a shows the Campbell diagram and Figure 10b the associated modal damping diagram (following extraction from the unfiltered eigenfrequency map for this case). It is seen that the removal of the Gümbel condition has a minor effect on the Campbell diagram, as far as frequency and whirl direction are concerned, but has a major effect on the damping ratio of mode 1, resulting in a significant downward shift to the OIS. Figure 11 shows the Campbell modes at 22 krpm, which have the same orientation and whirl direction as those of the previous case.

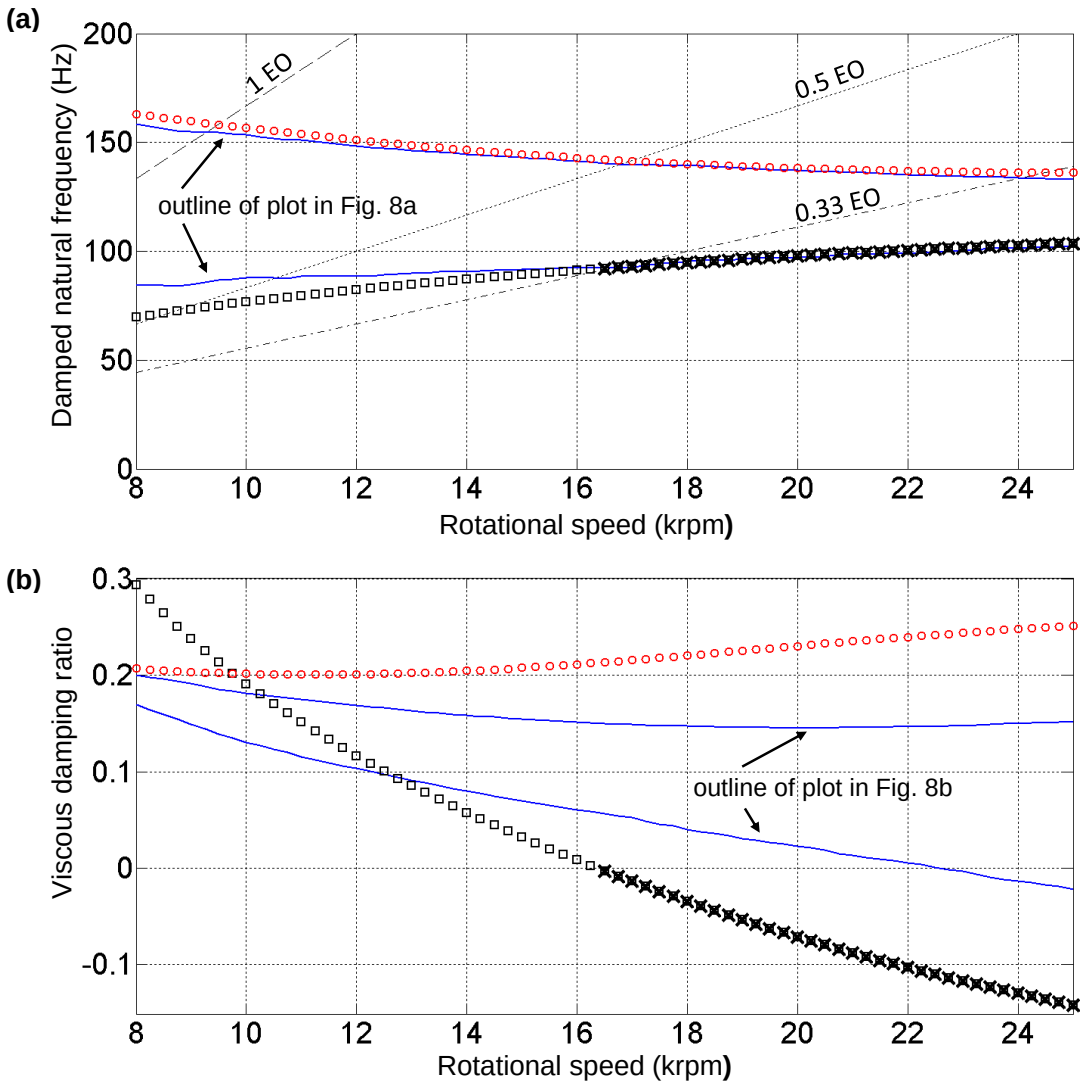

Figure 10. Campbell diagram (a) and associated modal damping diagram (b), for a symmetric rotor-FAB system with single-pad FABs assuming modal beam top foil ($H_{\mathrm{F}} = 20$) and linear discrete bump force ($\varrho = -\infty$ i.e. no detachment) with $p = p_{\mathrm{a}}$ at weld and *no* Gümbel: forward whirl (black squares); reverse whirl (red circles); unstable mode points overlaid with a cross; EO (engine order) (NB: extracted using minimum journal amplitude criterion, eq. (33) and a maximum modal damping criterion, $\zeta_n < 0.7$; identical results for CLE/FTE and FLE/CTE).

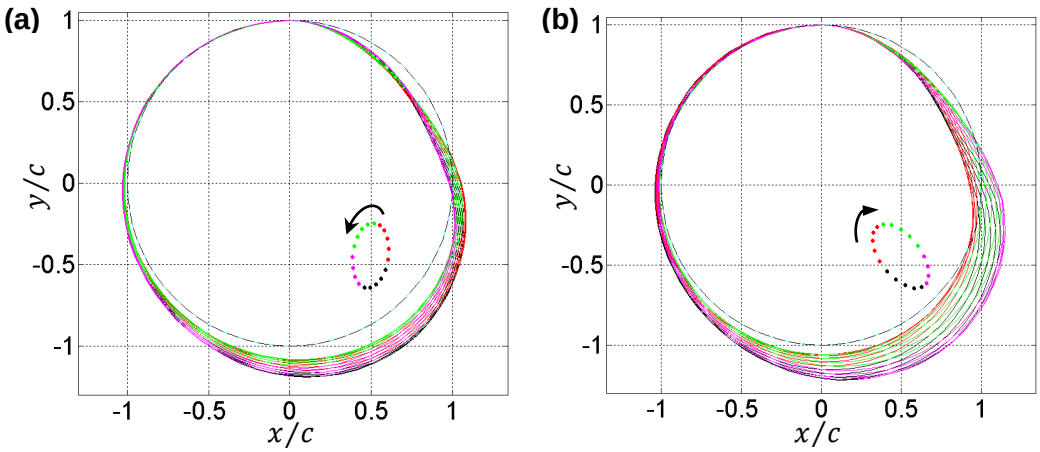

Figure 11. Modes at 22 krpm taken from Campbell diagram in Figure 10: (a) mode 1 ($f_{\mathrm{d},n} = 100.39$ Hz, $\zeta_n = -0.10282$, forward whirl); (c) mode 2 ($f_{\mathrm{d},n} = 136.93$ Hz, $\zeta_n = 0.23956$, reverse whirl).

.

Figures 12a,b show the Campbell diagram and associated modal damping diagram for free vibration about the SEPs in Figure 5c (no air film constraint). As expected, the OIS here is the same as that first reported by the author in [10] where the FAB model used SEFM and no air film constraints. Comparing with the previous results (Figures 10a,b) it is seen that the removal of the pressure constraint at the weld (while keeping the no-detachment condition) results in a slight reduction of the frequencies and a minor downshift in OIS.

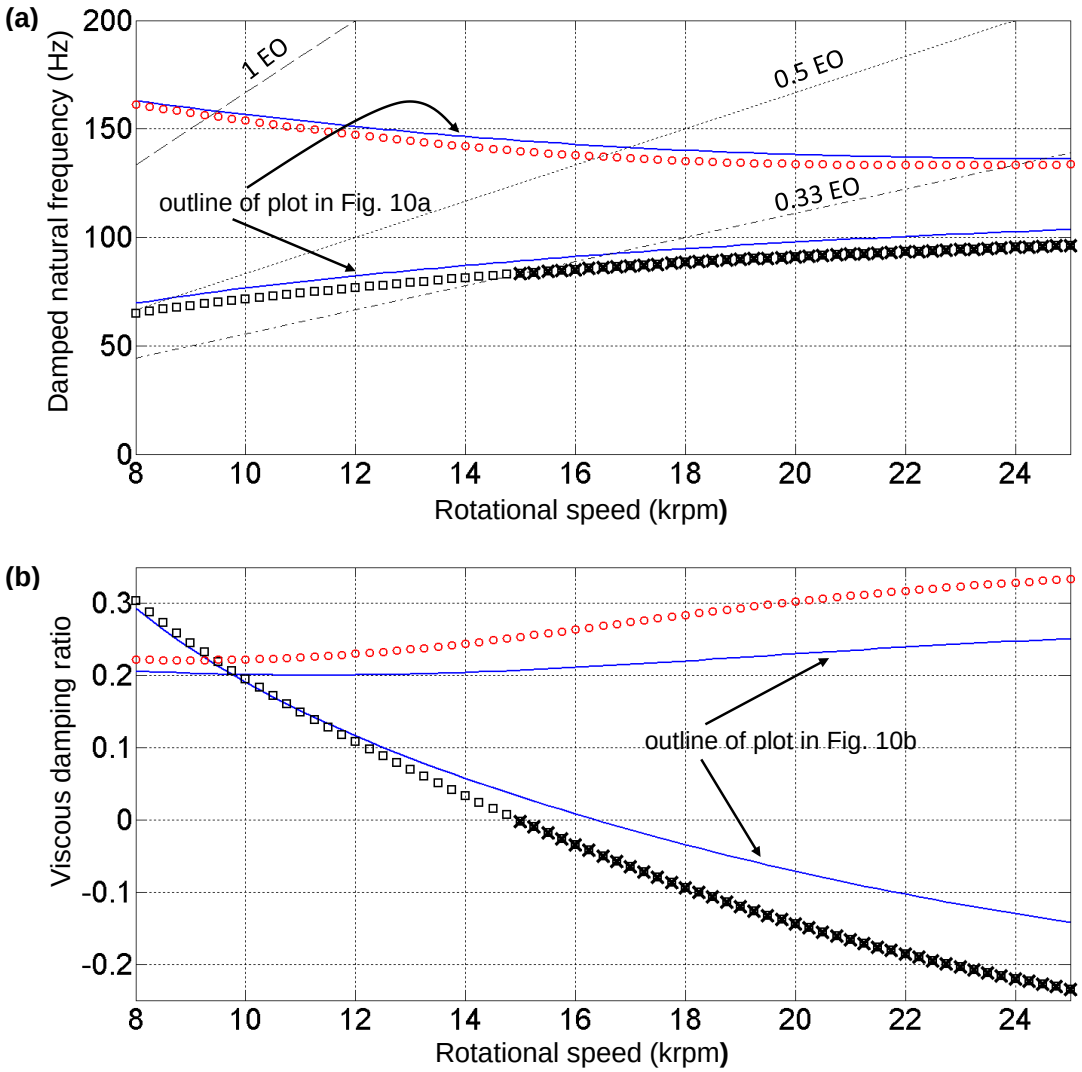

Figure 12. Campbell diagram (a) and associated modal damping diagram (b), for a symmetric rotor-FAB system with single-pad FABs assuming modal beam top foil ($H_F = 20$) and linear discrete bump force ($\varrho = -\infty$ i.e. no detachment) with no pressure constraints: forward whirl (black squares); reverse whirl (red circles); unstable mode points overlaid with a cross; EO (engine order) (NB: extracted using minimum journal amplitude criterion, eq. (33) and a maximum modal damping criterion, $\zeta_n < 0.7$; identical results for CLE/FTE and FLE/CTE).

4.2 Detachable modal beam top foil – smoothed bilinear discrete bump force: CLE/FTE

In the rest of this paper, top foil detachment is enabled by setting ϱ to a small positive number (Model 3, end of section 2.2). Unless otherwise stated, $\varrho = 10^{-3}$. This sub-section considers the clamped leading edge/free trailing edge (CLE/FTE) configuration.

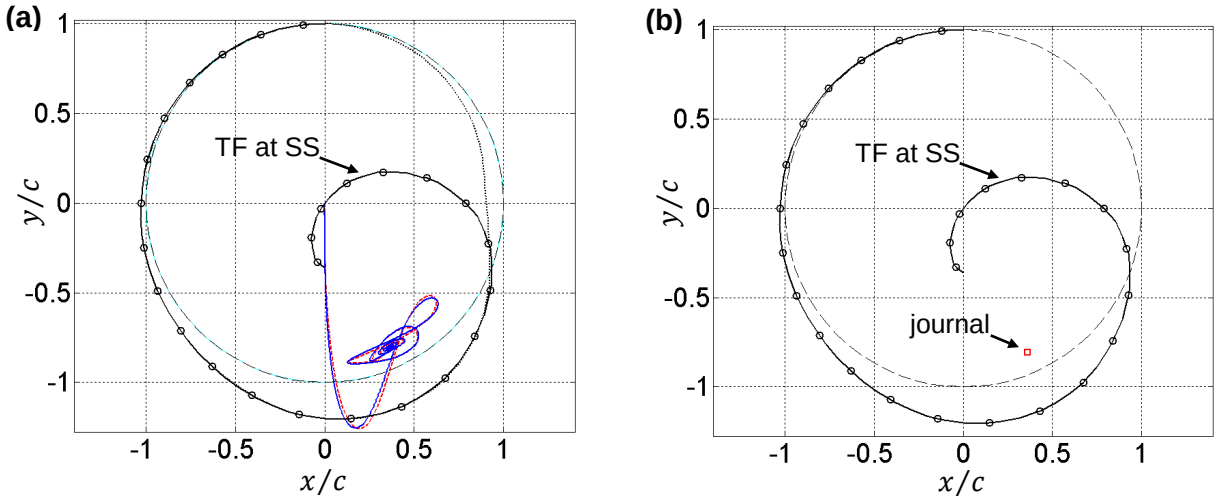

Figure 13. Results at 12 krpm and zero rotor unbalance for a symmetric rotor-FAB system with single-pad FABs, CLE/FTE, $p = p_a$ condition at weld, assuming modal beam top foil ($H_F = 20$) and smoothed bilinear discrete bump force ($\varrho = 10^{-3}$): (a) TNDA result for the journal trajectory from default initial conditions and deformed top foil (TF) at steady-state (SS) (corresponding results from Fig. 4(a) are reproduced as red, black dotted lines); (b) SS result (NB: TF locations at angular positions of bump apexes indicated by circles).

Figure 13 shows the TNDA result at 12 krpm with the condition $p = p_a$ at weld, where Figure 13a shows the convergence of the journal trajectory from default initial conditions towards the steady-state (SS) condition, and the deformed top foil at SS, and Figure 13b shows the SS configuration of both top-foil and journal. The journal trajectory closely follows that in Figure 4a ($\varrho = -\infty$, $p = p_a$ at weld, and Gümbel i.e. removal of sub-atmospheric pressures in journal force computation) whereas the top foil deflections deviate in the top right-hand quadrant due to top foil detachment. The results in Figure 13 agree very closely with those in Nielsen and Santos (Figure 3 of [17]), which is remarkable, given the modelling differences.

The researchers in [17] applied the condition $p = p_a$ at the weld. The removal of this constraint has virtually no effect on the results in Figures 13a,b. This is evident from Figures 14a,b which respectively show the mid-section pressure and film thickness at the steady-state condition (Figure 13b) with and

without the pressure constraint at the weld. It is also noted that the results in Figure 14a,b agree closely with those in [17] (see Figures 8a and 9a of [17]).

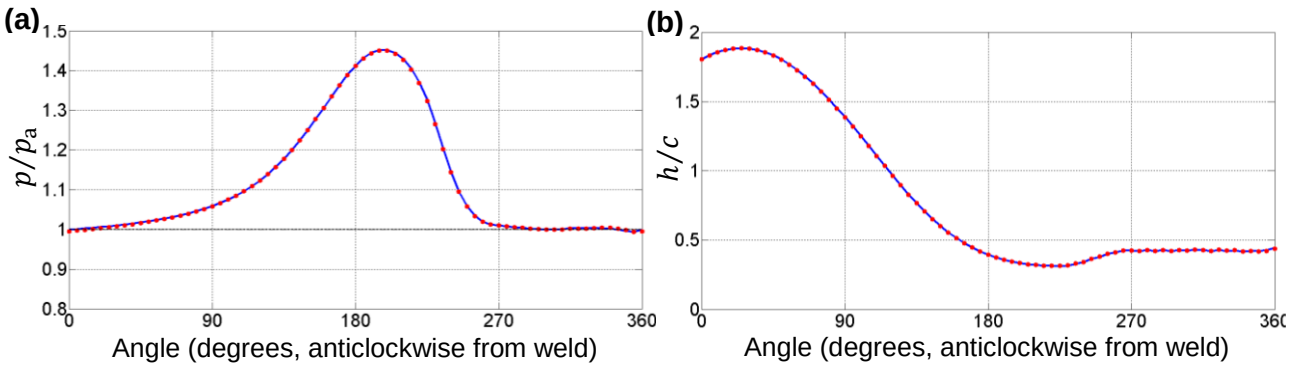

Figure 14. Non-dimensional pressure at mid-section of FAB (a) and non-dimensional air film thickness (b) for the steady-state condition at 12 krpm, zero rotor unbalance, symmetric rotor-FAB system with single-pad FABs, CLE/FTE, assuming modal beam top foil ($H_F = 20$) and smoothed bilinear discrete bump force ($\varrho = 10^{-3}$): $p = p_a$ condition at weld (blue solid line); no pressure constraint (red dotted line).

Figures 15a shows the locus of the SEPs of the journal for the speed range 8-25 krpm. Of the three loci in Figures 5a-c, the locus in Figure 15a is closest to Figure 5a, as expected. The OIS (22 krpm) is only slightly different from the case of Figure 5a (22.75 krpm). Figure 15b maps the state of contact of the top foil with the individual bumps at each point of the locus in Figure 15a (as per definitions of states A, B and C in section 2.2). As the speed increases from 16 krpm to 16.5 krpm, bump no. 19 (counting anti-clockwise from weld) transitions from a state of no contact with top foil (all speeds $\leq$16.25 krpm) to contact (all speeds $\geq$16.75 krpm), via a state of marginal contact (16.5 krpm). This implies that the top foil deflection away from the bump foil is gradually reducing with increasing speed, due to build-up of hydrodynamic pressure (see Figure 13b, where the top foil locations at the angular positions of the bump apexes are indicated by circles).

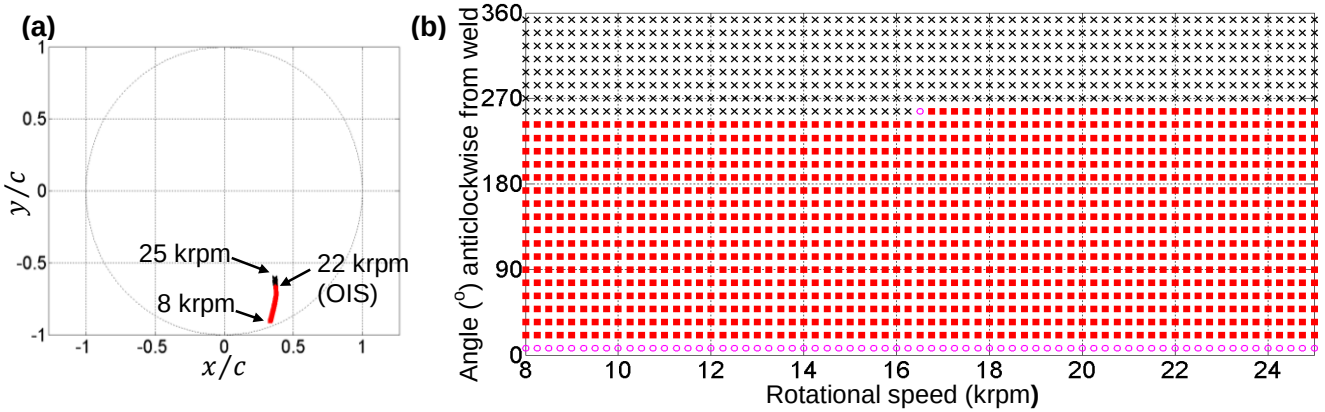

Figure 15. Static equilibrium condition over a range of speeds for a symmetric rotor-FAB system with single-pad FABs, CLE/FTE, $p = p_a$ condition at weld, assuming modal beam top foil ($H_F = 20$) and smoothed bilinear discrete bump force ($\varrho = 10^{-3}$): (a) Locus of static equilibrium journal positions (stable positions – red; unstable - black OIS – onset of instability speed); (b) State of contact between bump foil and top foil, points referring to distinct bumps (contact - red squares; no contact - black crosses; marginal contact – pink circles).

Figure 16 shows the unfiltered eigenfrequency *vs* speed map for free vibration (linearised) about the SEPs in Figure 15a. It is seen to cover a much higher frequency range (up to almost 14 kHz), than Figure 6a or 6b (which go up to ~2.5 kHz) since detachment introduces more possible modes of vibration.

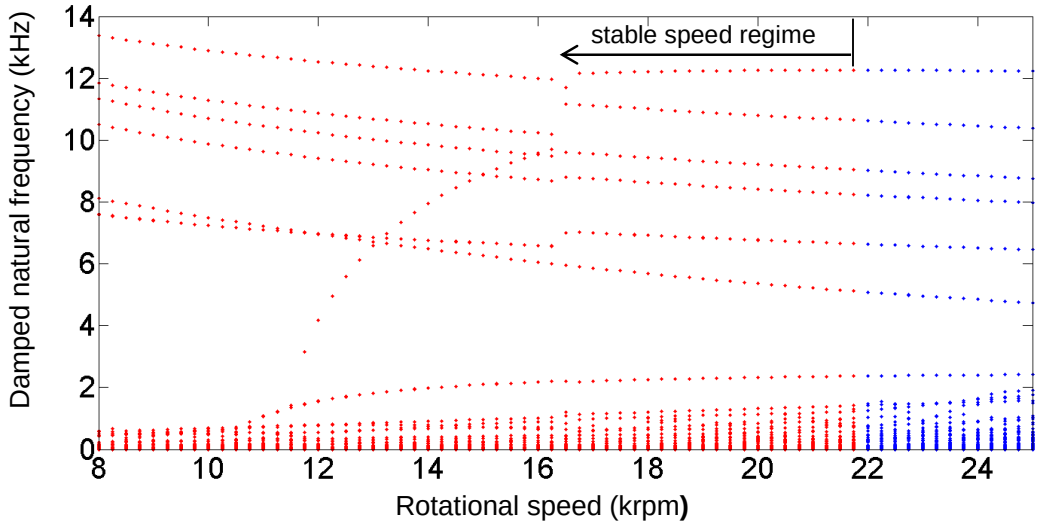

Figure 16. Unfiltered eigenfrequency $\varpi_{d,n}/(2\pi)$ *vs* speed map for a symmetric rotor-FAB system with single-pad FABs, CLE/FTE, $p = p_a$ condition at weld, assuming modal beam top foil ($H_F = 20$) and smoothed bilinear discrete bump force ($\varrho = 10^{-3}$).

The application of the filtering criterion of eq. (33) to the eigenfrequency map of Figure 16 results in the extraction of the Campbell diagram of Figure 17a. Figure 17b presents the viscous damping ratio of the extracted modes. These diagrams are seen to be close to those of Figure 8a,b ($\varrho = -\infty$ i.e. no detachment, $p = p_a$ at weld, and Gümbel), with similarities in details such as the transition of mode 2 from forward to reverse whirl as the speed changes from 8 krpm to ~8.5 krpm. However, the graphs of Figure 17a,b have one remarkable difference – a step-change in frequencies and damping ratios between 16.25 krpm and 16.75 krpm, which (by referring back to Figure 15b) corresponds to the top foil coming into (firm) contact with bump no.19 at the static equilibrium condition. This transition is seen to result in a small *upward* jump in both Campbell frequencies (Figure 17a). This *might* be explained by the additional stiffness introduced into the system by bump no. 19. However, Figure 17b shows that the damping ratio of Campbell mode 1 (the mode that becomes unstable) steps *down* while that of mode 2 steps *up*. These shifts will be verified by TNDA later on. It was earlier remarked that Nielsen and Santos [17] observed a transient subharmonic frequency in their TNDA analysis that corresponds to mode 1 of the Campbell diagram of Figure 8a. Due to the very short data length of the transient portion at each speed (0.22 s [17]), the frequency resolution would have been too low for the researchers in [17] to detect any sudden changes in this frequency. In any case, the author does not expect jumps in natural frequency (like those in Figure 17a,b) to happen with the model in [17], despite it being bilinear, since the bump foil compliance used in [17] was *continuously distributed* (SEFM), not localised at the 26 bump apex locations, thus ensuring that a small change in top foil static deflection does not result in an abrupt change to the modal characteristics.

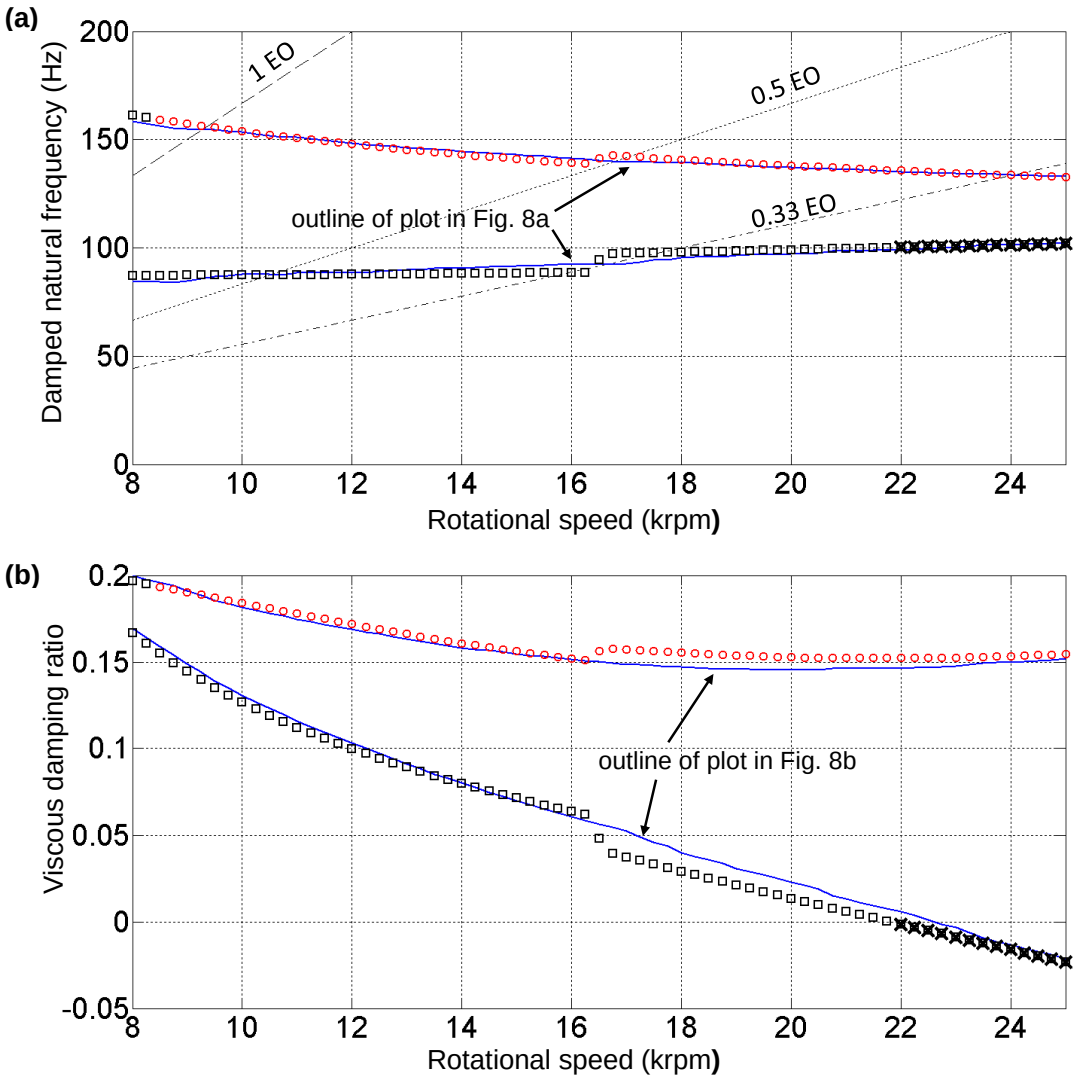

Figure 17. Campbell diagram (a) and associated modal damping diagram (b), for a symmetric rotor-FAB system with single-pad FABs, CLE/FTE, $p = p_a$ condition at weld, assuming modal beam top foil ($H_F = 20$) and smoothed bilinear discrete bump force ($\varrho = 10^{-3}$): forward whirl (black squares); reverse whirl (red circles); unstable mode points overlaid with a cross; EO (engine order) (NB: extracted using minimum journal amplitude criterion, eq. (33)).

Figures 18a,b show that the only effect of reducing ϱ from 10^{-3} to 10^{-6} is to sharpen the steps in the frequency and modal damping ratio curves. Figures 19a,b show that reducing the number of top foil component modes from $H_F = 20$ to $H_F = 10$ shifts the position of the step from ~16.5 krpm to ~18.5 krpm, but has little effect on the OIS. Increasing H_F from 20 to 50 causes a slight backward shift of the step but no change in OIS.

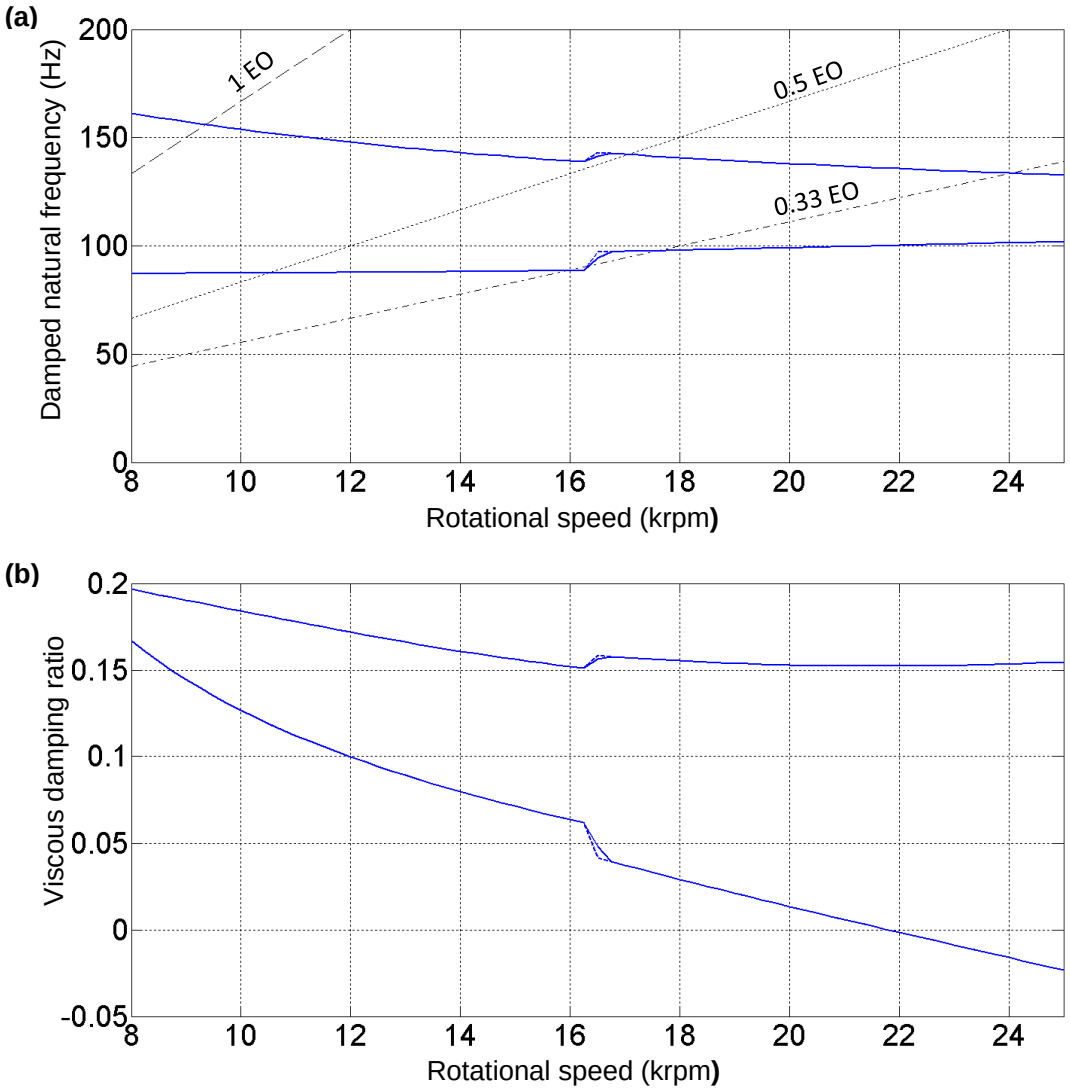

Figure 18. Effect of smoothing parameter ϱ on outline of Campbell diagram (a) and associated modal damping diagram (b), for a symmetric rotor-FAB system with single-pad FABs, CLE/FTE, $p = p_{\mathrm{a}}$ condition at weld, assuming modal beam top foil ($H_{\mathrm{F}} = 20$) and smoothed bilinear discrete bump force: $\varrho = 10^{-3}$ (solid line); $\varrho = 10^{-6}$ (dotted line).

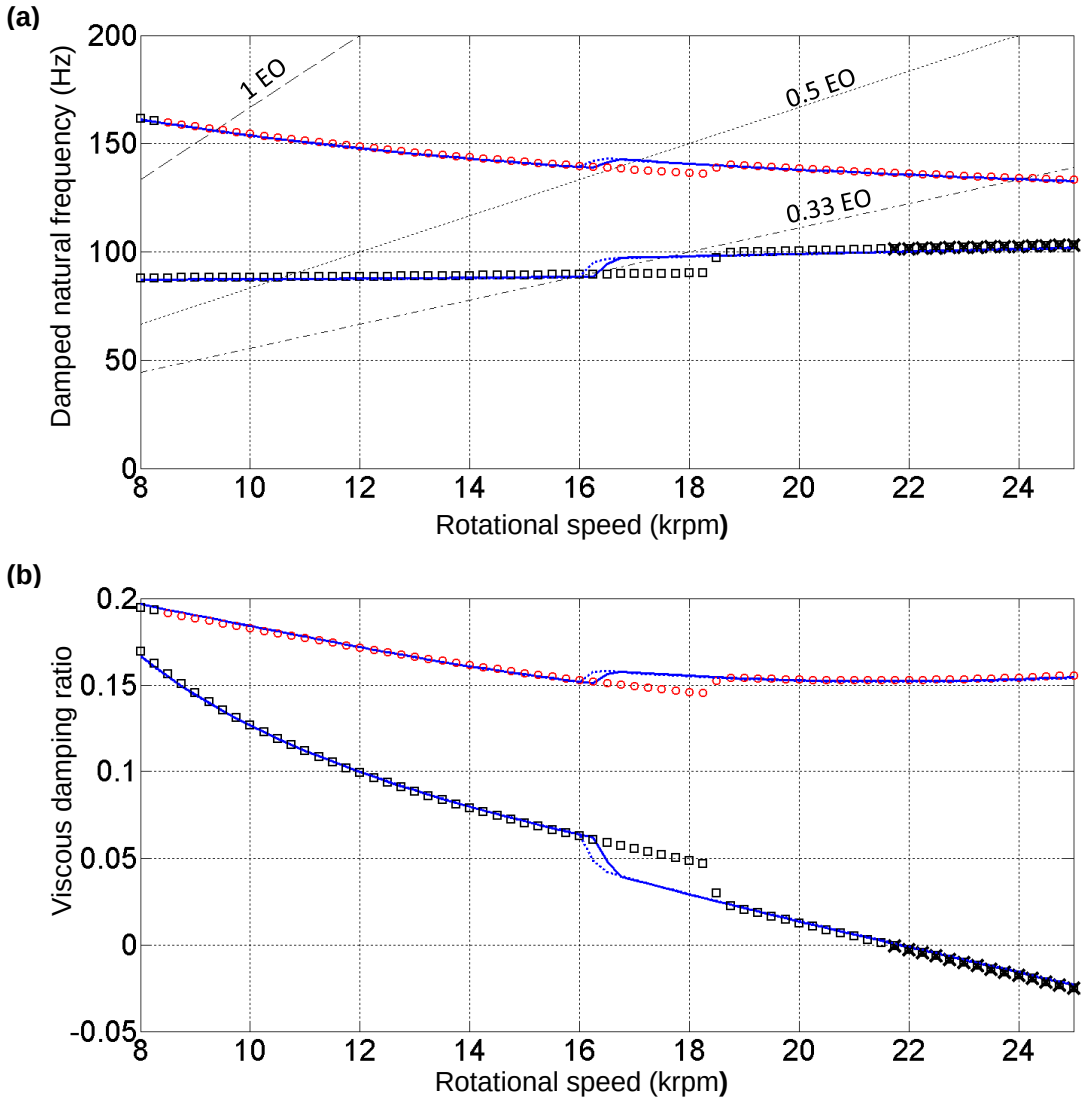

Figure 19. Effect of number of top foil modes on Campbell diagram (a) and associated modal damping diagram (b), for a symmetric rotor-FAB system with single-pad FABs, CLE/FTE, $p = p_a$ condition at weld, assuming modal beam top foil and smoothed bilinear discrete bump force ($\varrho = 10^{-3}$): $H_F = 10$ (detailed plots: forward whirl - black squares; reverse whirl - red circles; unstable mode points overlaid with a cross; EO - engine order); $H_F = 20$ (solid line – for more detail see Figure 17); $H_F = 50$ (dotted line) (NB: extracted using minimum journal amplitude criterion, eq. (33)).

Figures 20a,b shows the Campbell modes at 22 krpm. Comparing with those in Figure 9a,b the only significant differences are:

- The damping value of mode 1, since the speed considered (22 krpm) coincides with the OIS in this case.

- The modal vibration of the foil – Figure 20a,b shows for the first time the true modal vibration for CLE/FTE.

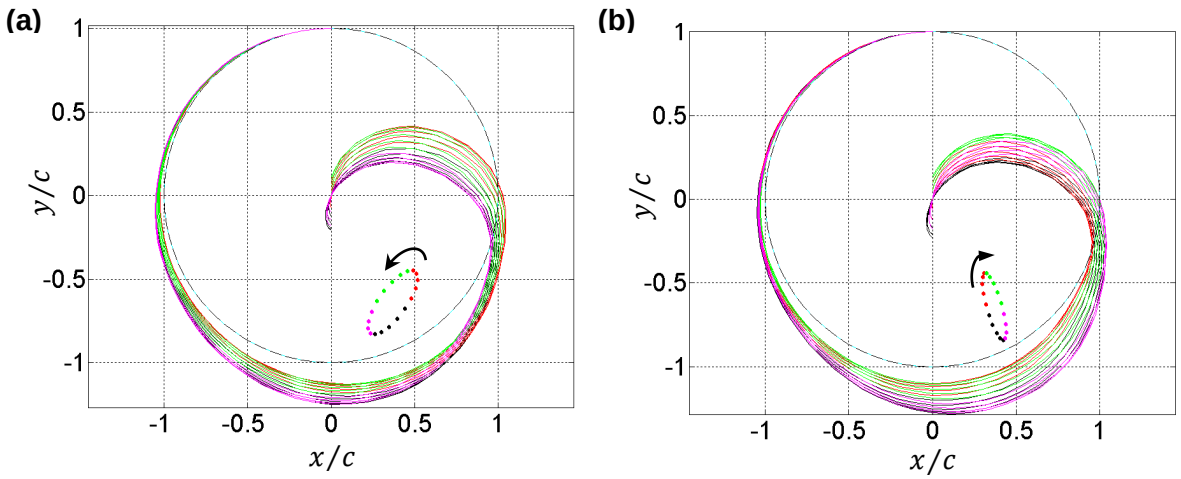

Figure 20. Modes at 22 krpm taken from Campbell diagram in Figure 17: (a) mode 1 ($f_{\mathrm{d},n} = 100.24$ Hz, $\zeta_n = -0.00143$, forward whirl); (c) mode 2 ($f_{\mathrm{d},n} = 135.675$ Hz, $\zeta_n = 0.15221$, reverse whirl).

The modes in Figure 20a,b were individually verified by TNDA of the nonlinear system (eq. (2)) using mode-specific initial conditions derived from the eigendata (see eq. (34)) with a suitably small reduction factor $c_n = 1/20$ (which means the perturbation corresponds to a journal displacement of ~1% of the radial clearance c since the modes are scaled to 20% of c). Figures 21a,b show that the TNDA journal trajectories have the same orientation and whirl directions as the journal orbits in Figures 20a,b. The reader is reminded that the exponential decay factor $\mathrm{e}^{-\zeta_n \varpi_{\mathrm{u},n} t}$ in eqs. (31), (32) was omitted when calculating the modal vibrations in Figures 20a,b (as per note in caption of Figure 7) – the inclusion of this factor will transform the elliptical journal orbits into spirals like those in Figure 21a,b. The values for damped natural frequency $f_{\mathrm{d},n} = \varpi_{\mathrm{d},n}/(2\pi)$ and the damping ratio ζ_n of the eigenmodes in Figure 20 were verified to a high degree of accuracy from the TNDA time histories by calculating the period and applying the logarithmic decrement method [27], as shown in Figure 21c. For added precision in the estimation of $f_{\mathrm{d},n}$, ζ_n the *Matlab* solver *ode23s* was set to output 200 points per shaft revolution when generating the TNDA responses in Figure 21.

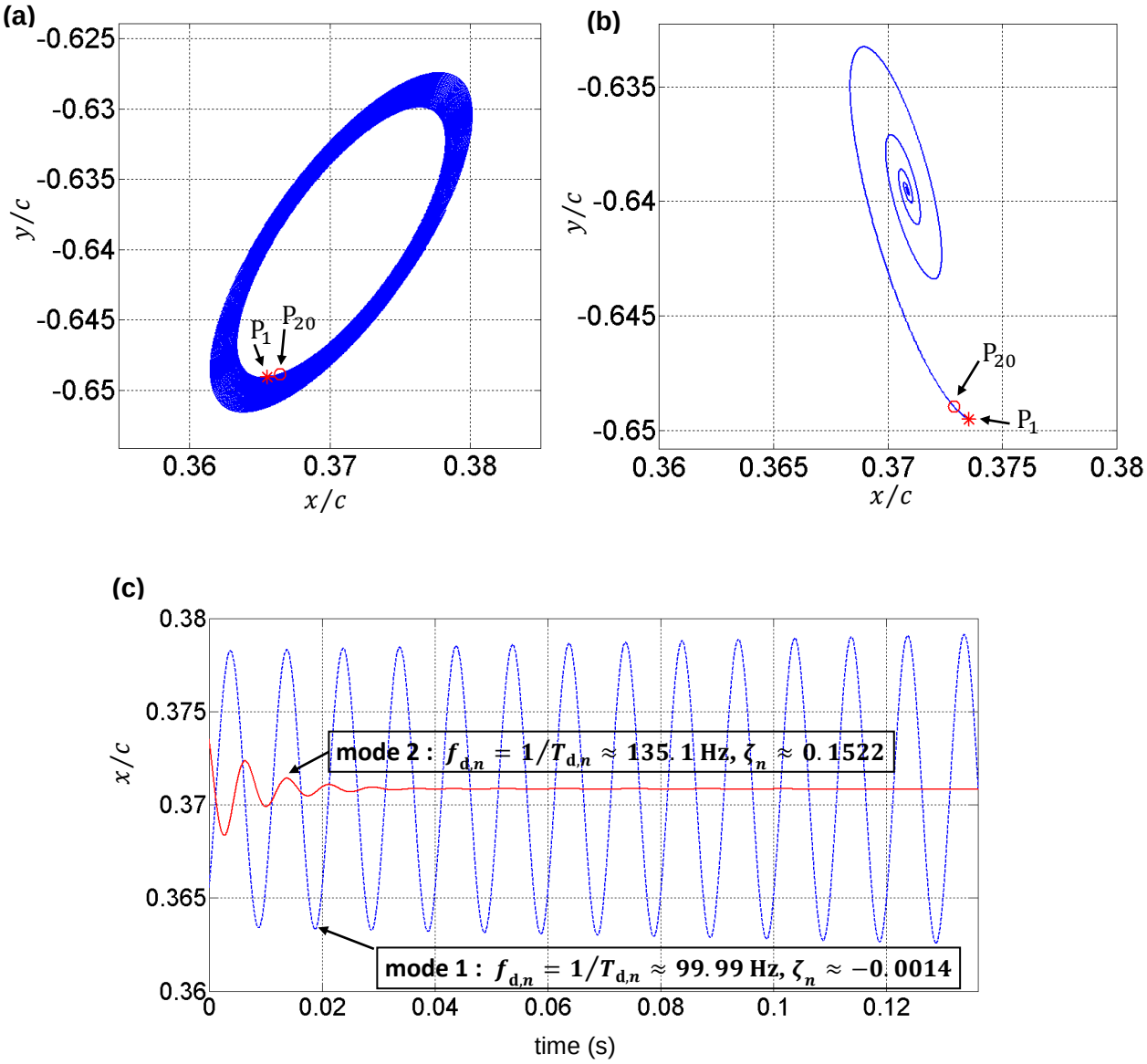

Figure 21. TNDA journal trajectories and time histories at 22 krpm using mode-specific initial conditions (eq. (34)) derived from the eigendata of the modes in the Campbell diagram of Figure 17: (a) mode 1; (b) mode 2; (c) time histories for estimation of $f_{d,n}$, ζ_n (P_1: point at $t = 0$; P_{20} : point 19 time steps later).

The coding was further developed to automate the above process, thus enabling the TNDA verification of each data point on the Campbell and modal damping ratio diagrams, as shown in Figure 22. The excellent correlation is evidence of the reliability of the SESMA procedure. The only significant discrepancy is in mode 2 at the step location (16.5 krpm, at which bump no. 19 is in the marginal contact state in the static equilibrium condition). The reason for this is shown in Figure 23 – the trajectory initially converges along the expected reverse whirl direction of mode 2 (Figure 23a), but interference

from the dominant (lesser damped) mode 1 causes the trajectory to switch to forward whirl as it closes in on the SEP. This mixing of modes affects the estimate of both frequency and (especially) damping ratio. This effect may be reduced if the reduction factor c_n is chosen to be even smaller. In [15] it was demonstrated that the TNDA trajectory may converge to the static equilibrium position from initial small perturbation conditions specific to a *stable* mode even if another mode is unstable (i.e. beyond OIS), provided the speed is sufficiently close to the OIS. It is seen from Figure 22 that the TNDA results for mode 2 replicate the eigenvalue analysis predictions well beyond the OIS. This was possible by using a smaller value of c_n than used in [15] ($1/20$ *vs* $1/10$) and basing the TNDA estimates for $f_{\mathrm{d},n}$, ζ_n on the first cycle of the TNDA simulation, before any possible interference from (the unstable) mode 1.

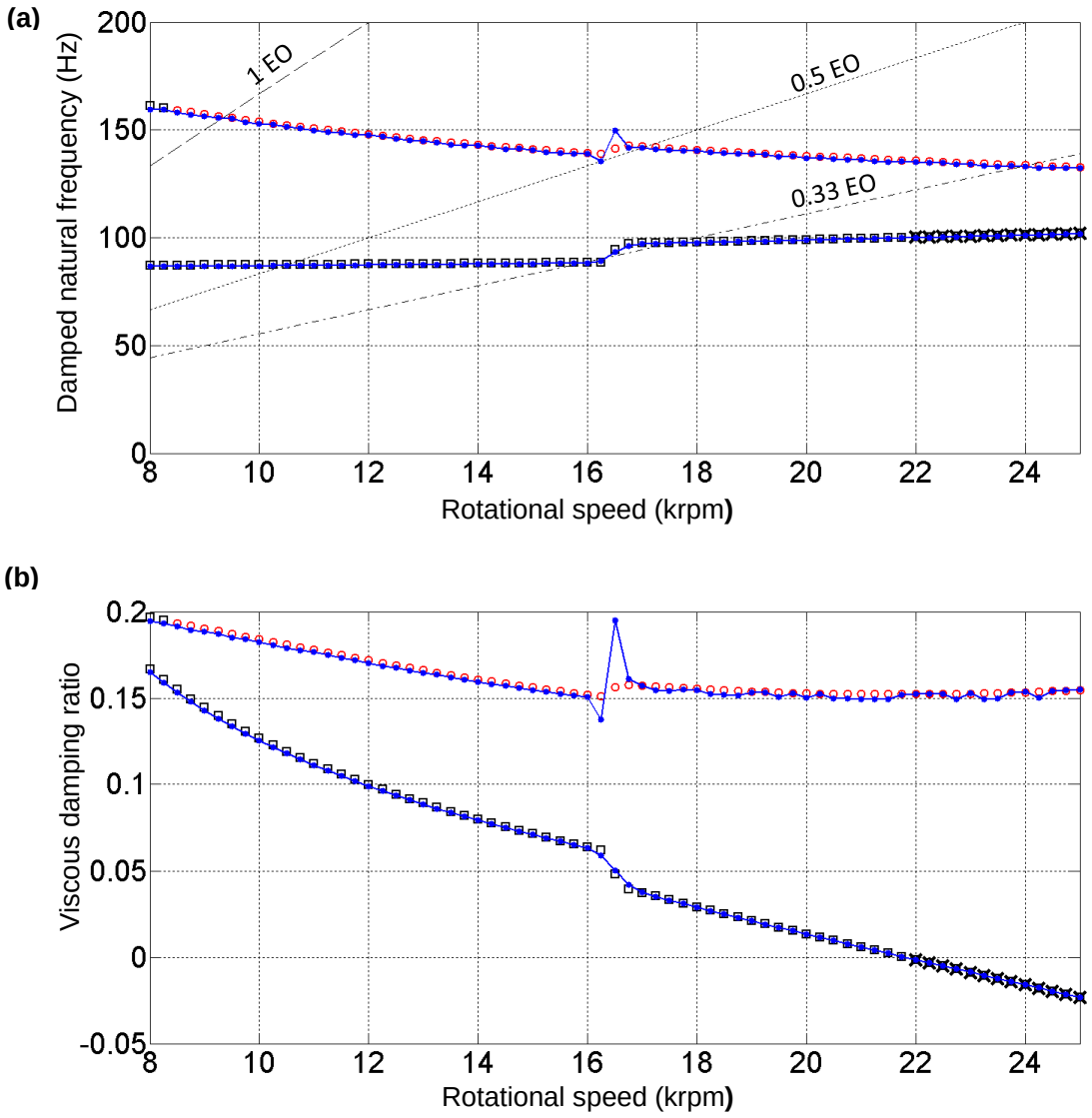

Figure 22. Verification of Campbell diagram and associated modal damping diagram of Figure 17, using estimates for $f_{\mathrm{d},n}$, ζ_n determined from time histories generated by TNDA from mode-specific initial conditions derived from the eigendata (as in Figure 21c): estimates for $f_{\mathrm{d},n}$, ζ_n (—●—); Campbell diagram/modal damping diagram (legend as in Figure 17).

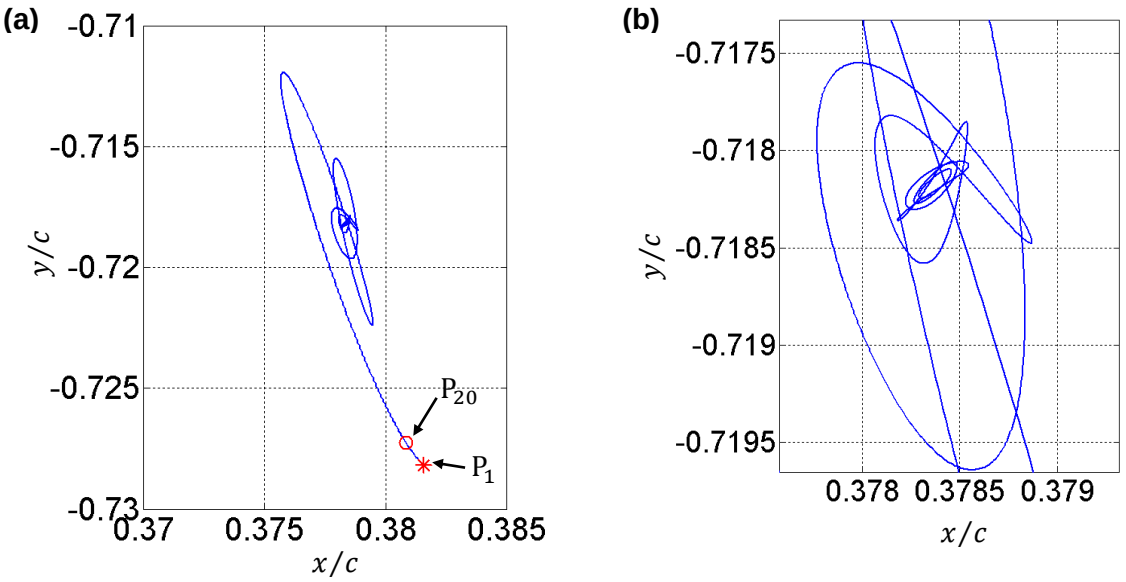

Figure 23. TNDA journal trajectory at 16.5 krpm using initial conditions specific to mode 2 of the Campbell diagram of Figure 17: (a) trajectory over 20 shaft revolutions, showing initial reverse (clockwise) whirl; (b) zoomed view of later stage of (a) showing eventual switch to mode 1 (forward whirl) (P_1: point at $t = 0$; P_{20} : point 19 time steps later).

4.3 Detachable modal beam top foil – smoothed bilinear discrete bump force: FLE/CTE

Attention now turns to the free leading edge/clamped trailing edge (FLE/CTE) configuration, which is the normal operating mode for single-pad FABs. The only published simulation with this configuration is found in Nielsen's thesis [24] and involved TNDA at 12 krpm from default initial conditions. Nielsen mentioned that, to achieve convergence, his simulation required considerably more top foil component modes (total of 50) than its CLE/FTE counterpart (total of 20), due to sharp change of curvature of the deflected top foil in the run-up toward the clamped trailing edge.

For the FLE/CTE case, the present author could not achieve convergence when performing TNDA at 12 krpm from *default* initial conditions, even with $H_F = 50$. However, it was found that convergence was easily achieved, even with $H_F = 20$, if the TNDA was initiated from the final conditions of the previous CLE/FTE simulation (Figure 13a), as shown in Figure 24a. It is seen that, upon switching from CLE/FTE to FLE/CTE, the trajectory converges to slightly higher static equilibrium position. The steady-state result is shown in Figure 24b, and this is virtually unchanged if H_F is then raised to 50.

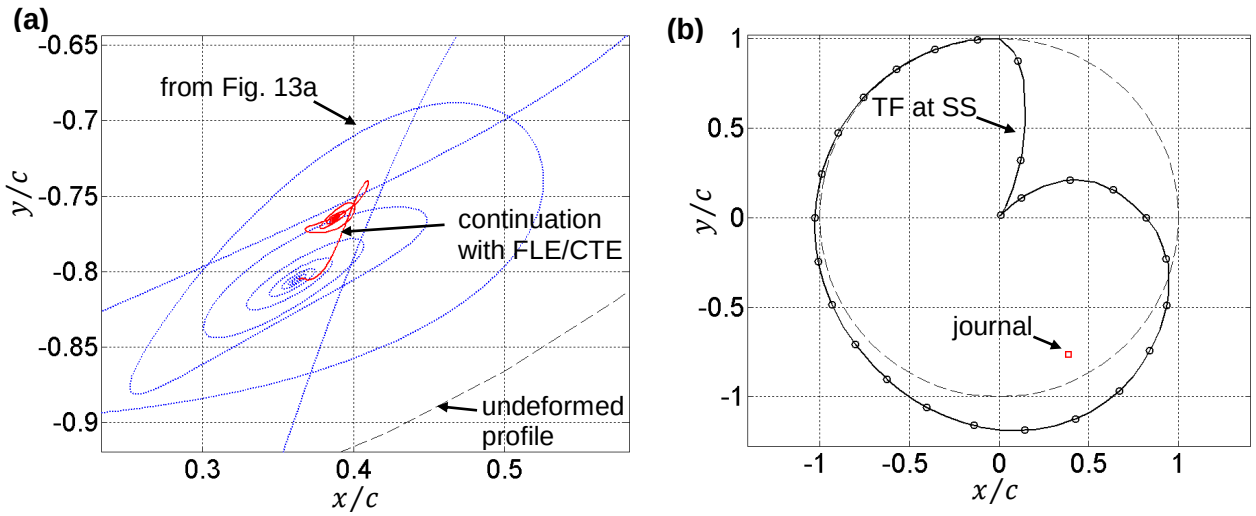

Figure 24. Results at 12 krpm and zero rotor unbalance for a symmetric rotor-FAB system with single-pad FABs, FLE/CTE, $p = p_a$ condition at weld, assuming modal beam top foil ($H_F = 20$) and smoothed bilinear discrete bump force ($\varrho = 10^{-3}$): (a) TNDA result for the transient journal trajectory (red solid line) continued from conditions on the trajectory in Figure 13a (reproduced as blue dotted line); (b) steady state (SS) result for top foil (TF) and journal (NB: TF locations at angular positions of bump apexes indicated by circles).

The result in Figure 24b agrees very closely with that in [24] (Figure 4.1, Case 2, in [24]), as do the corresponding pressure and film thickness profiles shown as blue solid curves in Figures 25a,b (compare these with Figure 4.2b, third and second rows, of [24]). The relevant curves in Figure 25a,b are those for the condition $p = p_a$ at the weld (the red dotted curves in Figure 25 are discussed later). As first found in [24], Figure 25a shows a region of sub-atmospheric pressure in the run-up to the trailing edge (TE) since the TE is clamped and so the foil cannot curl inward to a position that equalises the pressure on either side to atmospheric pressure, resulting in the top foil shape of Figure 24b.

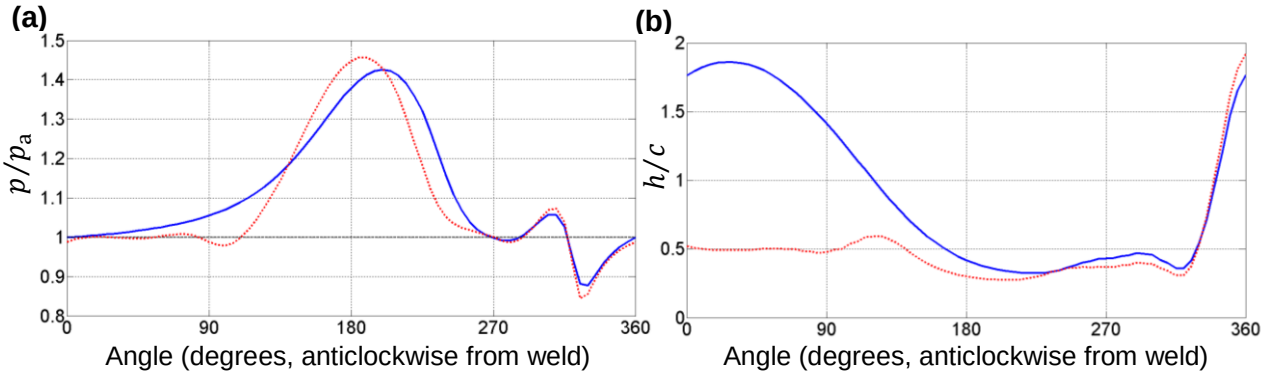

Figure 25. Non-dimensional pressure at mid-section of FAB (a) and non-dimensional air film thickness (b) for the steady-state condition at 12 krpm, zero rotor unbalance, symmetric rotor-FAB system with single-pad FABs, FLE/CTE, assuming modal beam top foil and smoothed bilinear discrete bump force ($\varrho = 10^{-3}$) and two pressure conditions at weld: $p = p_a$ condition at weld, as in Figure 24b (blue solid line); no pressure constraint at weld, as in Figure 32b (red dotted line).

It is important to note that the kink in Figure 24b is an artefact of the style of presentation of the top foil deflection w. The traditional way of presenting w is to superimpose it on the clearance circle (radius c) since one is primarily interested in the effect of w on the air film thickness. However, this distorts the profile of w since the undeformed radius of the top foil is R not c (where R is 19.05 mm i.e. $\sim 595c$). Such distortion may result in the appearance of a kink (Figure 24b) or a loop (Figure 32b later on) in regions where $w < 0$ and changing rapidly with θ. The true profiles of w corresponding to Figures 24b and Figure 32b are presented in Figure A.1 (Appendix) and do not feature a kink or a loop. This distortion (and consequent misrepresentation) is less of a problem if top foil detachment is suppressed (e.g. SEFM) since the inward deflection of the top foil is then restricted by the bump foil.

Figures 26a shows the locus of the SEPs of the journal. These are at a slightly higher level than those for the CLE/FTE case (Figure 15a) – as was evident from Figure 24a. This is attributed to the existence of sub-atmospheric pressure in the air film (Figure 25a), since it is recalled that for the case $\varrho = -\infty$ (i.e. no detachment), the removal of Gümbel led to higher SEPs (see Figures 5a,b). However, the difference in level between Figures 26a and 15a is not as significant as that between Figures 5b (no Gümbel) and 5a

(Gümbel) (in fact, Figure 26a is still closer to Figure 5a than to Figure 5b). The same can be said of the OIS – switching from CLE/FTE to FLE/CTE resulted in a decrease in OIS (22 krpm *vs* 20.25 krpm), as expected from the existence of sub-atmospheric pressure, but the decrease (8%) is not as big as the 27.5% decrease in OIS when comparing Figure 5a (22.75 krpm) with Figure 5b (16.5 krpm). All this suggests that the detachment of the top foil (Figure 24b) has somewhat restricted (but not eliminated) the development of sub-atmospheric pressure, thus mitigating its effect on performance.

Figure 26b maps the state of contact of the top foil with the individual bumps at each point of the locus in Figure 26a. Once again, (as in the CLE/FTE case of Figure 15b), it is bump no. 19 that transitions from a state of no contact with the top foil to a state of contact, but this happens at a lower speed (no contact for all speeds ≤15 krpm, marginal contact at 15.25 krpm, contact for all speeds ≥15.5 krpm).

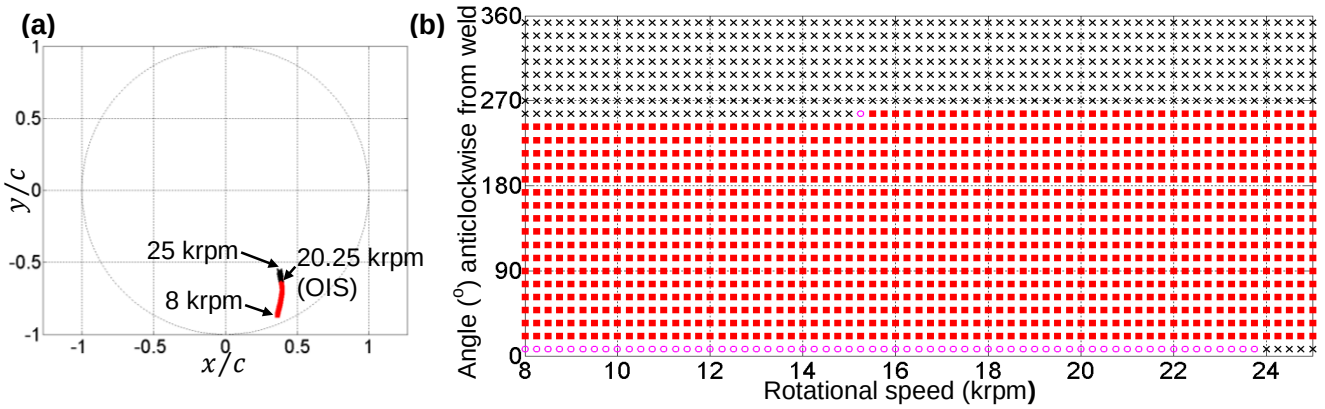

Figure 26. Static equilibrium condition over a range of speeds for a symmetric rotor-FAB system with single-pad FABs, FLE/CTE, $p = p_a$ condition at weld, assuming modal beam top foil ($H_F = 20$) and smoothed bilinear discrete bump force ($\varrho = 10^{-3}$): (a) Locus of static equilibrium journal positions (stable positions – red; unstable - black OIS – onset of instability speed); (b) State of contact between bump foil and top foil, points referring to distinct bumps (contact - red squares; no contact - black crosses; marginal contact – pink circles).

Figure 27 shows the unfiltered eigenfrequency *vs* speed map for free vibration about the static equilibria in Figure 26a. The application of the filtering criterion of eq. (33) results in the extraction of the Campbell diagram of Figure 28a, and Figure 28b shows the associated modal damping diagram. These diagrams are seen to be fairly close to those for CLE/FTE case (Figure 17a,b). In both cases, mode 2 reverses its whirl direction as the speed increases from 8 krpm to ~8.5 krpm. The steps in the frequency

and damping ratio diagrams of the FLE/CTE case are located at a lower speed (15.25 krpm), in line with the corresponding state of contact map in Figure 26b. As before, the steps are upward for both Campbell frequencies, and down, up respectively for the corresponding damping ratios

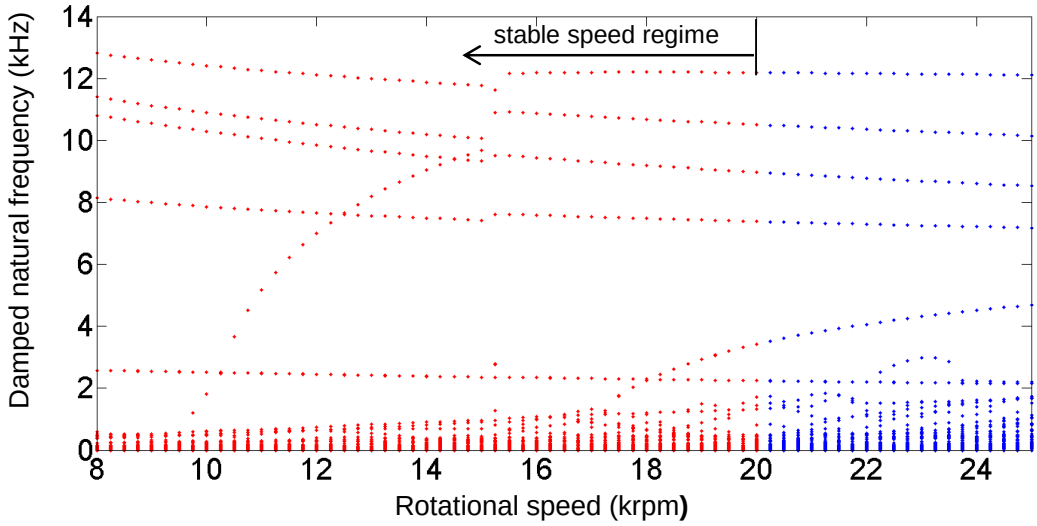

Figure 27. Unfiltered eigenfrequency $\varpi_{\mathrm{d},n}/(2\pi)$ *vs* speed map for a symmetric rotor-FAB system with single-pad FABs, FLE/CTE, $p = p_{\mathrm{a}}$ condition at weld, assuming modal beam top foil ($H_{\mathrm{F}} = 20$) and smoothed bilinear discrete bump force ($\varrho = 10^{-3}$).

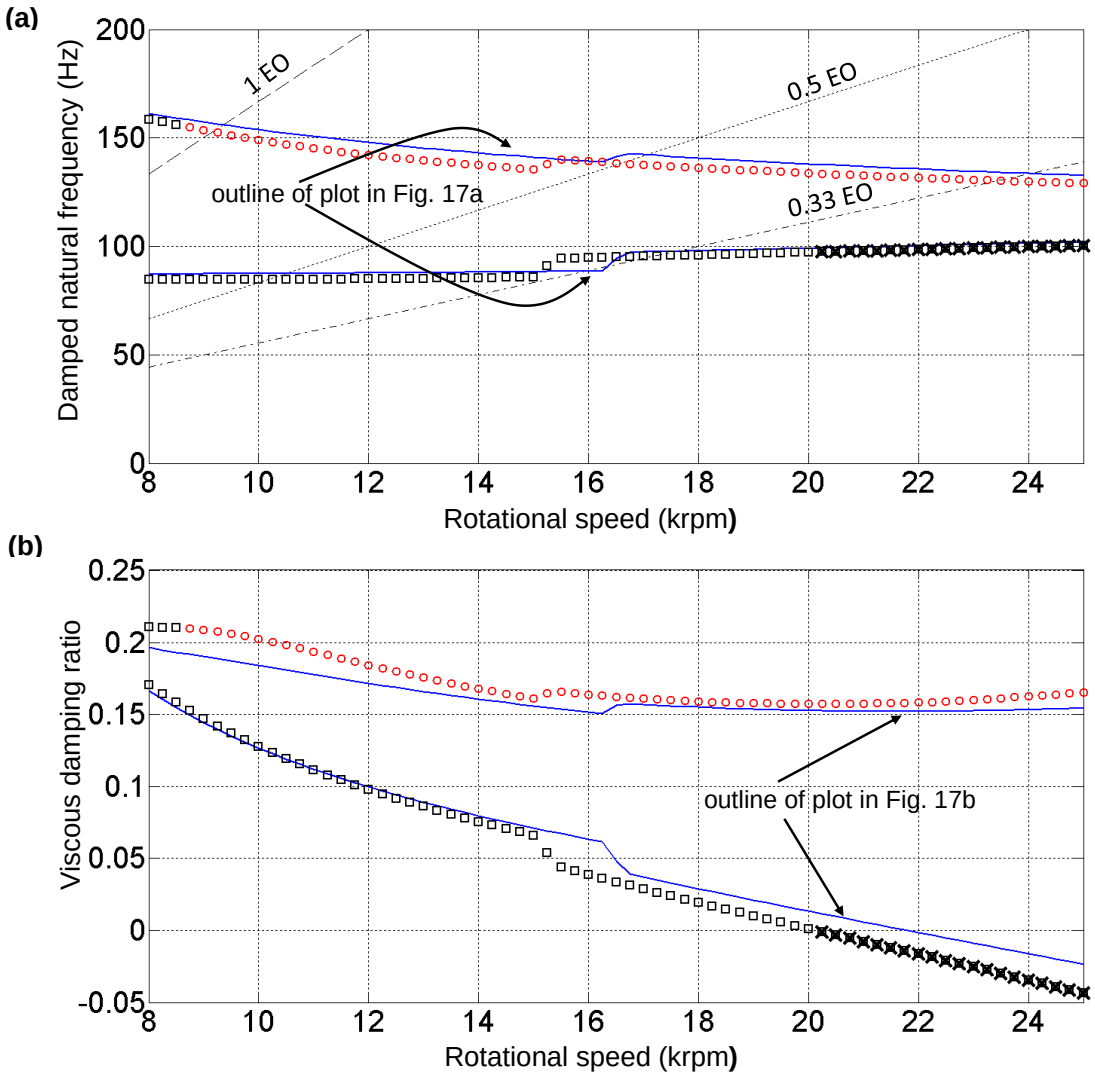

Figure 28. Campbell diagram (a) and associated modal damping diagram (b), for a symmetric rotor-FAB system with single-pad FABs, FLE/CTE, $p = p_a$ condition at weld, assuming modal beam top foil ($H_F = 20$) and smoothed bilinear discrete bump force ($\varrho = 10^{-3}$): forward whirl (black squares); reverse whirl (red circles); unstable mode points overlaid with a cross; EO (engine order) (NB: extracted using minimum journal amplitude criterion, eq. (33)).

Figures 29a,b show that reducing the number of top foil component modes from $H_F = 20$ to $H_F = 10$ has a significant effect on the OIS, shifting it downward from 20.25 krpm to 17.5 krpm. In contrast, the same change in the CLE/FTE case only reduced the OIS by 0.25 krpm (Figure 19). Nonetheless, Figure 29 shows that increasing H_F from 20 to 50 in the FLE/CTE case has an even less significant effect than in the CLE/FTE case.

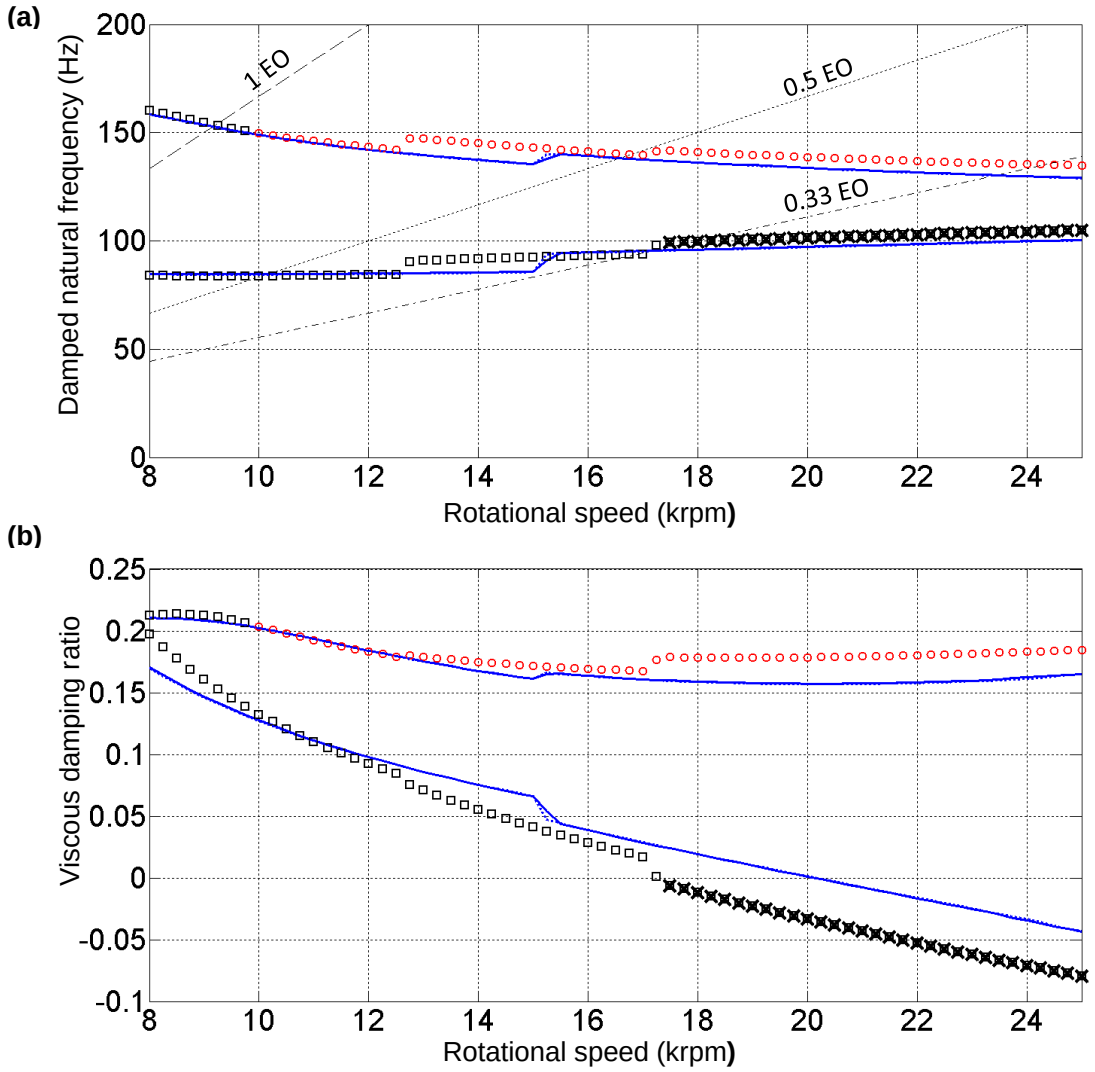

Figure 29. Effect of number of top foil modes on Campbell diagram (a) and associated modal damping diagram (b), for a symmetric rotor-FAB system with single-pad FABs, FLE/CTE, $p = p_a$ condition at weld, assuming modal beam top foil and smoothed bilinear discrete bump force ($\varrho = 10^{-3}$): $H_F = 10$ (detailed plots: forward whirl - black squares; reverse whirl - red circles; unstable mode points overlaid with a cross; EO - engine order); $H_F = 20$ (solid line – for more detail see Figure 28); $H_F = 50$ (dotted line) (NB: extracted using minimum journal amplitude criterion with $C = 0.1$, and for case $H_F = 10$, additional criterion of $\zeta_n < 0.5$).

Figures 30a,b shows the Campbell modes at 22 krpm for the FLE/CTE case. Comparing these with those in Figure 20a,b (CLE/FTE), the main difference is obviously the top foil vibration. The SESMA-computed damped natural frequency and damping ratio values in the caption of Figure 30, and at all other speeds within the range considered, were verified from the analysis of the time histories generated by TNDA of the original system (eq. (2)) from mode-specific initial conditions (eq. (34)), as previously done

in Figures 21c and 22. Figure 31 shows that the verification was highly accurate except for mode 2 at the step location, for the same reasons described in Figure 23.

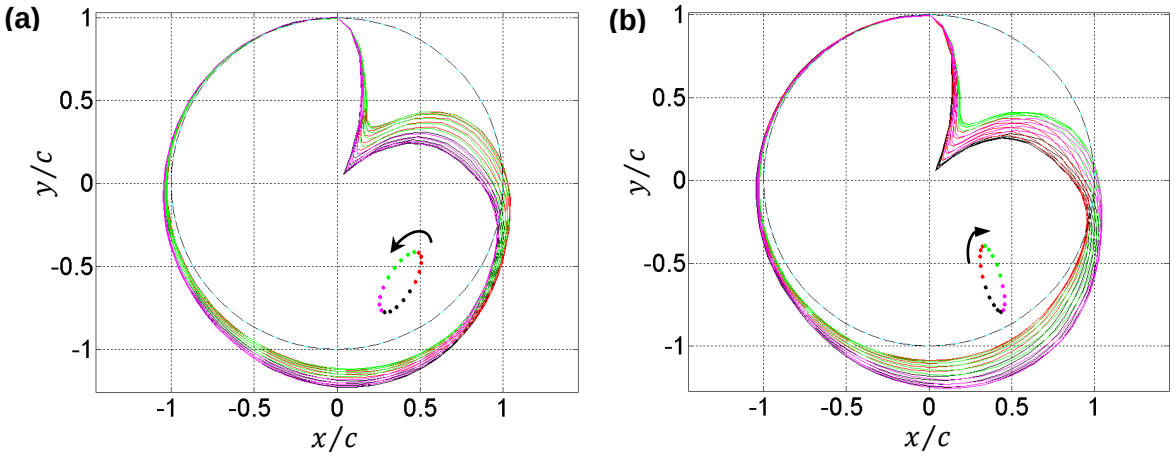

Figure 30. Modes at 22 krpm taken from Campbell diagram in Figure 28: (a) mode 1 ($f_{\mathrm{d},n} = 98.54$ Hz, $\zeta_n = -0.01638$, forward whirl); (c) mode 2 ($f_{\mathrm{d},n} = 131.64$ Hz, $\zeta_n = 0.15857$, reverse whirl).

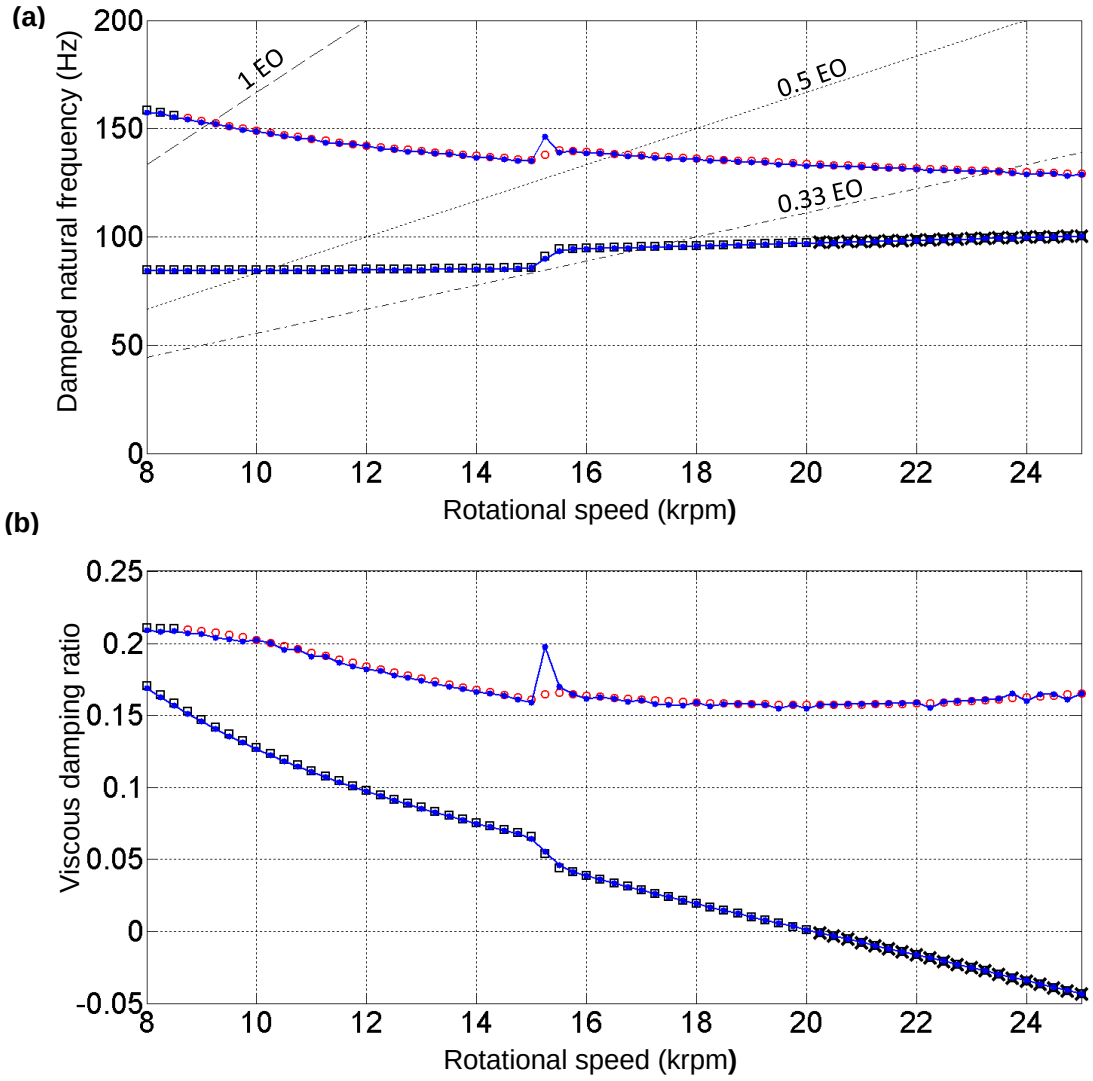

Figure 31. Verification of Campbell diagram and associated modal damping diagram of Figure 28, using estimates for $f_{\mathrm{d},n}$, ζ_n determined from time histories generated by TNDA from mode-specific initial conditions derived from the eigendata (as in Figure 21c): estimates for $f_{\mathrm{d},n}$, ζ_n (—●—); Campbell diagram/modal damping diagram (legend as in Figure 28).

4.3.1 Effect of removal of pressure constraint $p = p_{\mathrm{a}}$ at the weld on FLE/CTE results

Returning to the TNDA simulation at 12 krpm, the removal of the pressure condition at the weld enabled convergence towards a SEP, directly from default initial conditions, with $H_{\mathrm{F}} = 10$ top foil component modes, but not any more (see red dotted trajectory in Figure 32a). The corresponding steady-state deflection curve of the top foil indicates that $H_{\mathrm{F}} = 10$ may not be sufficient. The coding had the facility

of continuing an existing simulation with an increased number of top foil component modes. Figure 32a shows that continuation with $H_F = 60$ resulted in convergence towards a lower-positioned SEP, and an exact steady-state top foil deflection curve. The resulting steady-state result in Figure 32b is seen to be markedly different from that in Figure 24b ($p = p_a$ condition at weld). Figures 25a,b respectively compare the corresponding air film pressure and film thickness profiles, and the main difference is seen to lie in the left-hand half of the clearance. For the case of no pressure constraint at the weld there is a small region of sub-atmospheric pressure starting at around 90° anti-clockwise from the weld (red dotted profile in Figure 25a), which causes the free end to curl away from the bump foil (Figure 32b). This results in a substantial difference in air film thickness (Figure 25b) which affects the load-carrying ability of the FAB (resulting in a lower-positioned journal SEP).

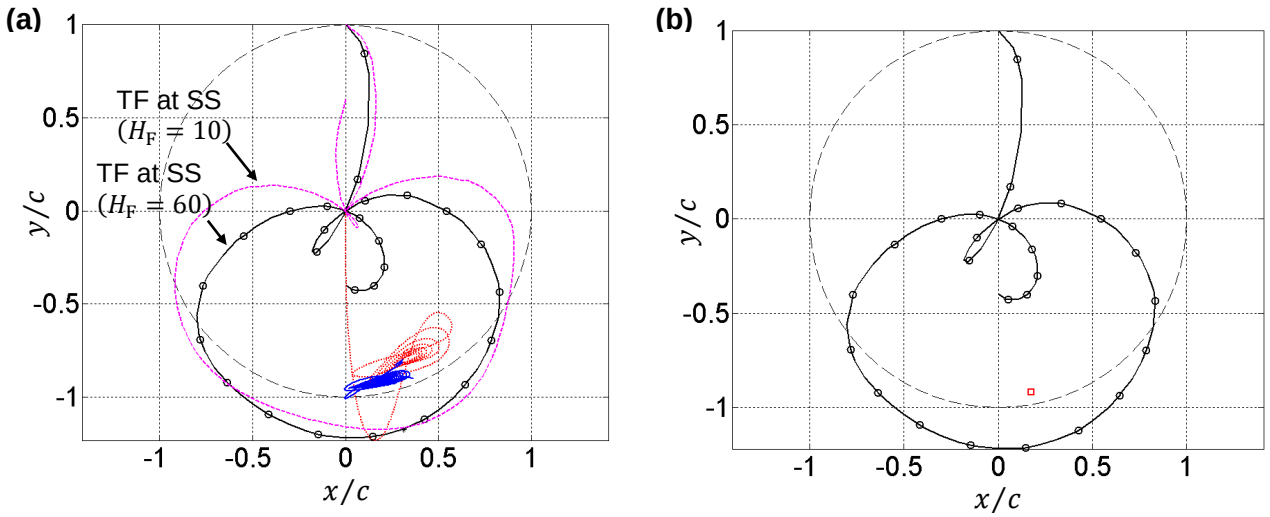

Figure 32. Results at 12 krpm and zero rotor unbalance for a symmetric rotor-FAB system with single-pad FABs, FLE/CTE, no pressure constraint at weld, assuming modal beam top foil and smoothed bilinear discrete bump force ($\varrho = 10^{-3}$): (a) TNDA result for the transient journal trajectory with $H_F = 60$ (blue solid line) continued from the result with $H_F = 10$ (reproduced as red dotted line); (b) steady state (SS) result for top foil (TF) and journal for $H_F = 60$ (NB: TF locations at angular positions of bump apexes indicated by circles).

Figure 33a shows that, with the removal of the pressure condition from the weld of the FLE/CTE single-pad FAB, the journal SEP is not predicted to lift-off over the speed range 8-25 krpm, and that the top foil is detached from the majority of the bumps at all speeds (Figure 33b). In this case, instability of modal vibration about the SEPs prevails over most of the speed range. As expected, the resulting Campbell

diagram is very different from any shown so far and is shown in the Appendix (Figure A.2). It was found that, over the speed range 19.5-25 krpm, the dominant instability was not a Campbell mode, but a mode dominated by the top foil vibration, with negligible journal vibration (ranging from 10 to 11 kHz). This phenomenon is analogous to pad flutter in tilting pad bearings. Such a phenomenon was recently mentioned by the researchers in [16], who did not detect it in their computation but speculated on the unlikelihood of encountering it in the eigenvalue analysis.

Given that, in practice, single-pad FABs are installed with FLE/CTE [2] and do not exhibit the above simulated load-carrying problem, one can conclude that the condition $p = p_a$ at the weld is an essential requirement when simulating top foil detachment. It should be emphasised however, that for simple foil models that ignore top foil detachment, the omission of this pressure condition does not result in problems regarding journal lift-off, rather the contrary, as can be seen by comparing Figure 5c with 5b.

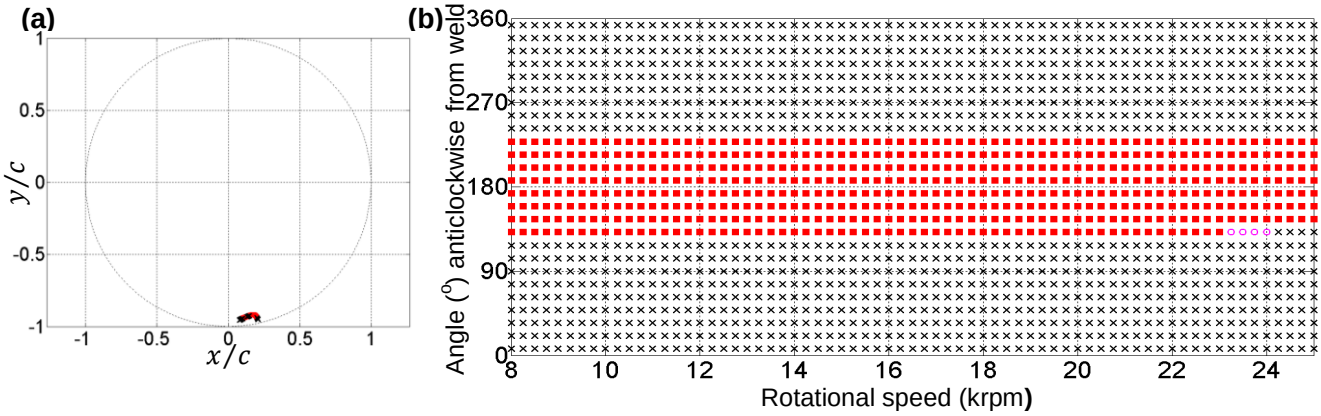

Figure 33. Static equilibrium condition over a range of speeds for a symmetric rotor-FAB system with single-pad FABs, FLE/CTE, no pressure constraint at weld, assuming modal beam top foil ($H_F = 60$) and smoothed bilinear discrete bump force ($\varrho = 10^{-3}$): (a) Locus of static equilibrium journal positions (stable positions – red; unstable – black); (b) State of contact between bump foil and top foil, points referring to distinct bumps (contact - red squares; no contact - black crosses; marginal contact – pink circles).

4.3.2 Summarised comparison of FLE/CTE detachment and no-detachment cases (for $p = p_a$ at the weld)

For the FLE/CTE pad, it has already been observed that the existence of sub-atmospheric pressure produces the same sort of changes (compared with the CLE/FTE pad) that the removal of Gümbel has on simple (no-detachment) foil models (namely the *elevation* of SEPs and, more significantly, the *reduction*

in OIS), albeit to a *lesser* extent. Figure 34 compares the Campbell and modal damping diagrams for the FLE/CTE detachable top foil model with those of the alternative no-detachment models - one with Gümbel, one without. The Gümbel curves are seen to be actually closer to the advanced model curves than the non-Gümbel ones. Hence, while the Gümbel condition is inappropriate in principle for FLE/CTE application (due to the existence of sub-atmospheric pressures), this does not necessarily mean that it will not lead to improved results, at least as far as SESMA is concerned.

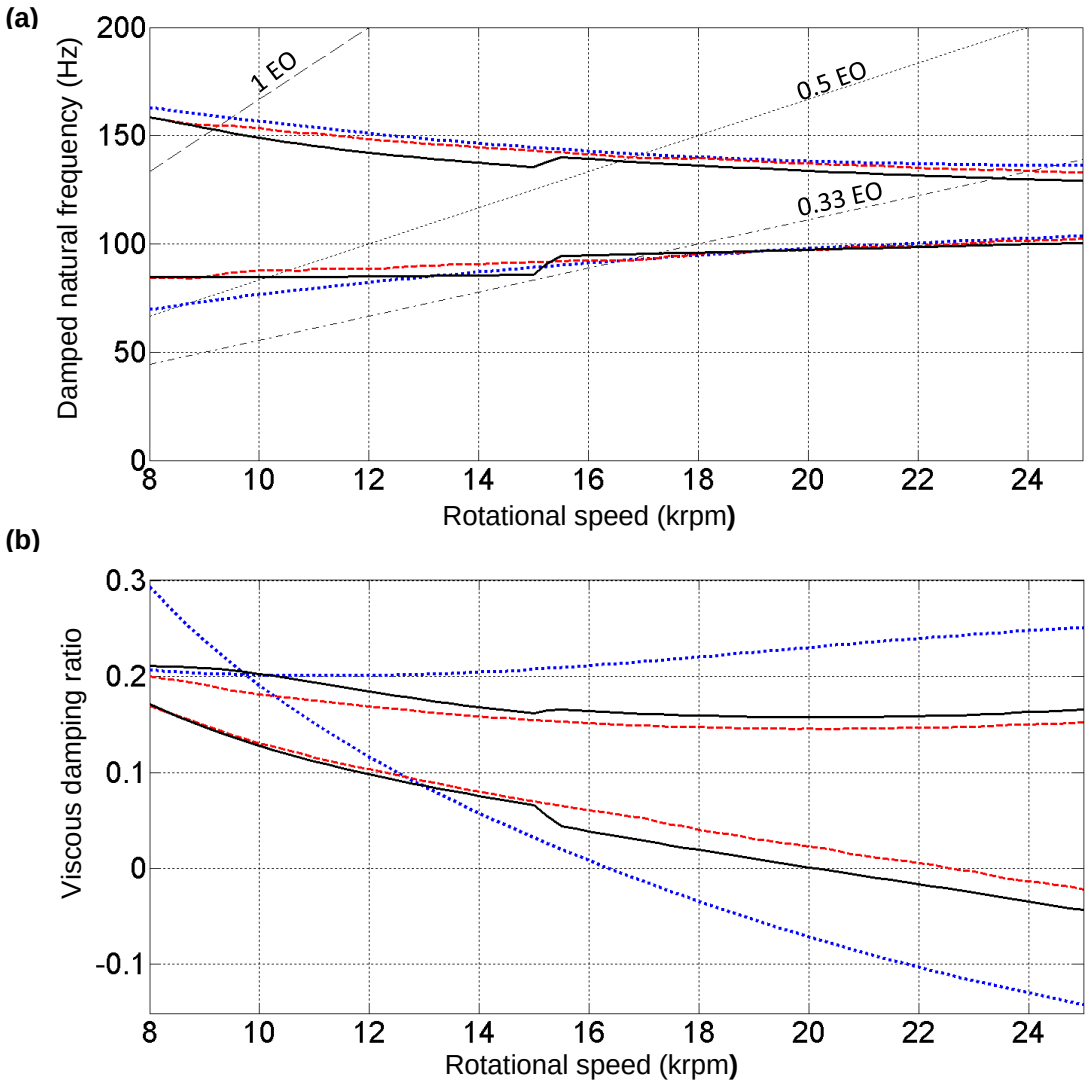

Figure 34. Comparison of Campbell diagram and modal damping diagram in Figure 28 i.e. *FLE/CTE* with *detachable* modal top foil (solid black line) with those in Figure 8 i.e. non-detachable modal top foil *with* Gümbel condition (dashed red line), and those in Figure 10 i.e. non-detachable modal top foil *without* Gümbel condition (dotted blue line) (EO - engine order).

.

4.4 Effect of bump foil hysteretic damping model conversion

The conversion of the bump foil damping model from hysteretic of loss factor η to viscous of damping matrix $\mathbf{K}_{\mathrm{b_{eff}}}\eta/\omega_{\mathrm{ref}}$ (in Ns/m) means that, for a steady-state vibration at a generic circular frequency ω, the hysteretic loss factor has been changed to $\eta\omega/\omega_{\mathrm{ref}}$ [21]. The resulting model is only equivalent to the original hysteretic model for harmonic vibration at ω_{ref} [27]. This change is necessary to work in the time domain since a frequency-independent hysteric loss factor η is only applicable for harmonic excitation (and the damped-free response with such damping is *non-causal* [28]). The decaying/growing modal perturbations in eq. (24) are therefore based on *one* imposed ω_{ref} (i.e. one viscous damping matrix). The rationale of choosing $\omega_{\mathrm{ref}} = \Omega$ is the consideration that the general linear response is the addition of the homogenous solution expression in eq. (24) and the steady-state oscillation driven by (a suitably-low) unbalance excitation - the viscous damping matrix that applies to this latter component is then *imposed* by the modified model on all the damped-free components of eq. (24).

von Osmanski et [16] (considering the same symmetric rigid rotor system, but with SEFM) recently changed ω_{ref} from Ω to ϖ_{Ca_1}, where $\varpi_{\mathrm{Ca}_1} = \varpi_{\mathrm{Ca}_1}(\Omega)$ is the (speed-dependent) damped circular frequency of Campbell mode no. 1 (i.e. the mode becoming unstable). In this way, the equivalent hysteretic loss factor of the viscous model is $\eta\varpi_{\mathrm{Ca}_1}/\varpi_{\mathrm{Ca}_1} = \eta$ for steady-state vibration at ϖ_{Ca_1} and $\eta\varpi_{\mathrm{Ca}_2}/\varpi_{\mathrm{Ca}_1}$ for steady-state vibration at ϖ_{Ca_2} (the damped circular frequency of mode 2). Manual iteration was then used in [16] to update ω_{ref} to match ϖ_{Ca_1} in the eigenvalue analysis. The resulting OIS in [16] was found to be 24.34 krpm, compared with 21.81 krpm when using $\omega_{\mathrm{ref}} = \Omega$ (in [16] η was 0.2 whereas here it is 0.25).

For the present work, the codes were upgraded to give the user the choice of either Ω or ϖ_{Ca_1} for ω_{ref}, with automatic generation of the Campbell diagram in either case. At each speed, the eigenvalue analysis at iteration no. *k* was performed with $\omega_{\mathrm{ref}}|_k = \varpi_{\mathrm{Ca}_1}\big|_{k-1}$, where $\omega_{\mathrm{ref}}|_1 = \Omega$ and $\varpi_{\mathrm{Ca}_1}\big|_k$ is identified from the result of the eigenvalue analysis, knowing that it belongs to the least-damped mode (for this system, at least - more sophisticated identification strategies may be applied for others). The iteration is repeated

until there is convergence in $\varpi_{\mathrm{Ca}_1}\big|_k$ before moving to the next speed. The eigenfrequency *vs* speed map is then filtered as before.

In line with [16], the only significant change arising from a switch in ω_{ref} from Ω to ϖ_{Ca_1} is a delay in OIS. In the CLE/FTE case, the OIS shifts from 22 krpm to 25.5 krpm, whereas in the FLE/CTE case it shifts from 20.25 krpm to 23 krpm. Apart from this, there is very little change to the Campbell diagram, as seen from Figure 35a. The shift in OIS means a shift in the modal damping, as per Figure 35b.

Finally, it is noted that the total CPU times on *Matlab* (2012 release) for SESMA over the range 8-26 krpm, in steps of 0.25 krpm, are as follows:

- $H_{\mathrm{F}} = 20$ (i.e. Jacobian 1078×1078): 7.7 mins ($\omega_{\mathrm{ref}} = \varpi_{\mathrm{Ca}_1}$), 4.5 mins ($\omega_{\mathrm{ref}} = \Omega$).
- $H_{\mathrm{F}} = 50$ (i.e. Jacobian 1198×1198): 12.2 mins ($\omega_{\mathrm{ref}} = \varpi_{\mathrm{Ca}_1}$), 5 mins ($\omega_{\mathrm{ref}} = \Omega$).

The above data shows that the Campbell diagram analysis procedure first introduced in [3, 15] is readily implementable to systems with complex FAB models.

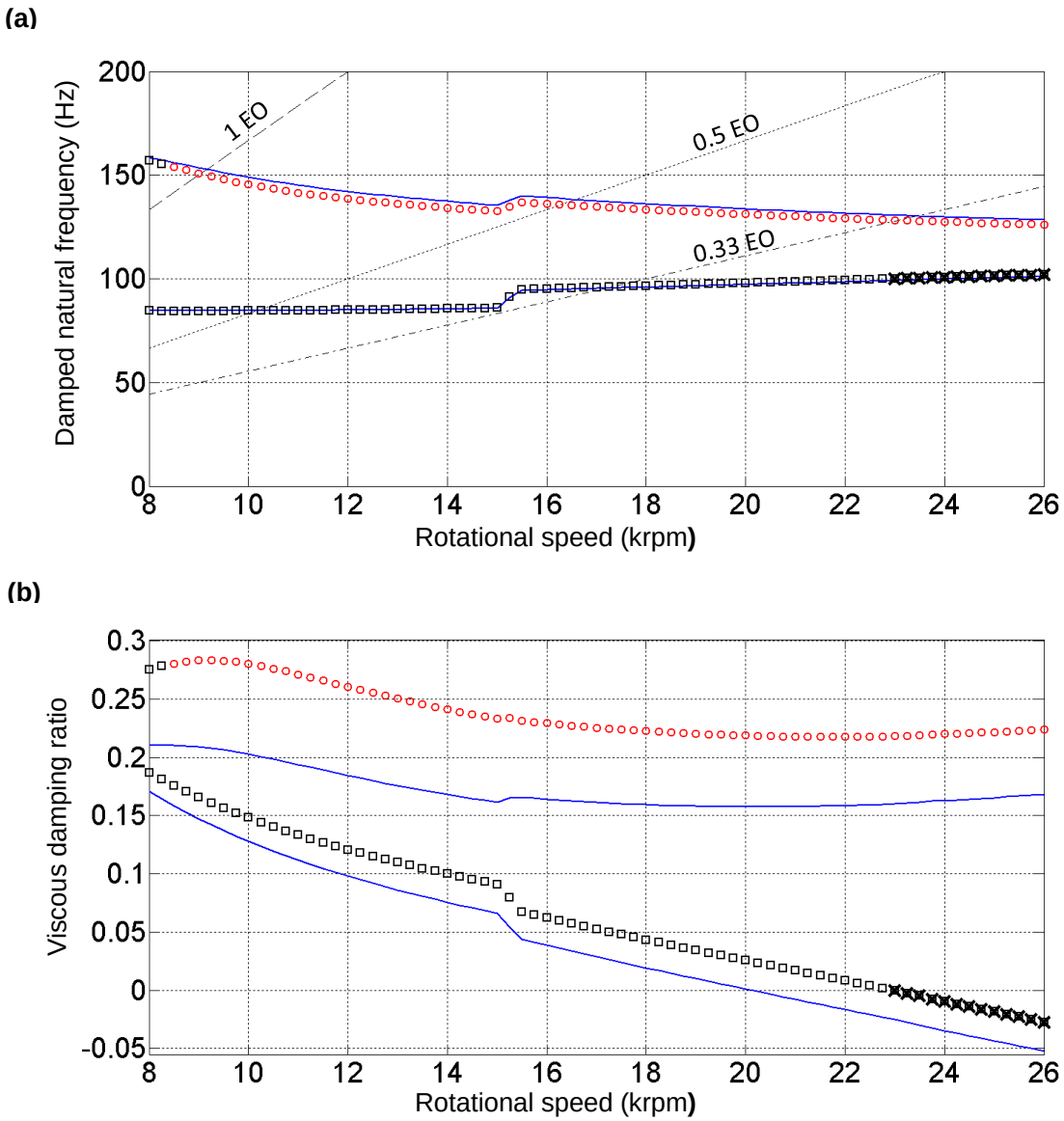

Figure 35. Effect of changing the reference frequency ω_{ref} used in the assumed viscous damping model of the bump foil (of given hysteretic damping) on Campbell diagram (a) and modal damping diagram (b), for FLE/CTE: $\omega_{\mathrm{ref}} = \varpi_{\mathrm{Ca}_1}(\Omega)$ (detailed plots: forward whirl - black squares; reverse whirl - red circles; unstable mode points overlaid with a cross; EO - engine order); $\omega_{\mathrm{ref}} = \Omega$ (solid blue lines – for more detail see Figures 28a,b).

5. CONCLUSIONS

The effects of air film constraints and top foil detachment in a rotor-FAB model have been investigated for the first time using SESMA, backed up by TNDA where needed. The SESMA followed the procedure recently established by the author, which is based on the eigenvalue analysis of the state Jacobian of the coupled rotor-FAB system. Such a linearisation approach eliminates the errors associated

with the traditional LFCM, which in any case is inapplicable to the required FAB model. The novel FAB model comprised an air film modelled with FD acting on a modal beam top foil that can detach from bumps that are discretely distributed (and elastically coupled, if considered) according to a bilinear model with smoothing. These features distinguish it from the only other detachable top foil model used in coupled rotor-FAB analysis. Application to a symmetric rigid rotor on single-pad FABs gave the following salient conclusions.

- TNDA results presented the first independent verification of the detachable top foil model results presented in the literature for both operating modes of a single-pad FAB - CLE/ FTE [17], and the more practical FLE/CTE [24].
- The recently established SESMA [3] procedure operated efficiently and accurately (verified by TNDA) without any modifications required.
- The Campbell and modal damping diagrams revealed an abrupt shift in the modal frequencies and damping ratios, due to a certain bump transitioning into a state of contact with the top foil in the static equilibrium state, as the speed increases (since the gradual increase in air pressure reduces the top foil's static deflection away from bump foil). The shifts in frequency were upwards, whereas the shift in the damping ratio of the dominant mode was downward. These shifts might be reduced by redesigning the bump foil to be as close as possible to an idealised continuously distributed compliance (several strips side-by-side with staggered bumps).
- If using a simple no-detachment model to simulate a CLE/FTE pad, Gümbel is a satisfactory correction for the TNDA journal trajectory, SEPs, OIS, and overall modal characteristics (although, it cannot reproduce the true top foil deflection and the aforementioned abrupt changes to the modal characteristics).
- Switching to FLE/CTE resulted in sub-atmospheric pressure in the region close to the CTE (confirming the finding in [24]), which is associated with a slight rise in the SEPs, and more significantly, the lowering of the OIS. These changes in SEPs and OIS were not as big as those obtained by removing Gümbel from the no-detachment (linear) foil model. Thus, the application

of Gümbel to FLE/CTE operation, even if inappropriate in principle, might lead to improved results (as in Figure 34). It is emphasised that this finding is based on SESMA of this specific system. The inappropriateness of Gümbel may become apparent when performing TNDA for large-amplitude limit cycles beyond the OIS, and the unbalance response. This was the case in the experimentally validated study of [2], where Gümbel did not perform as well as the model without any pressure constraints (i.e. as in Figure 5c).

- The pressure constraint at the weld is an essential requirement when simulating foil detachment in the FLE/CTE configuration.
- On the issue of converting the bump foil damping from hysteretic to viscous, switching the reference frequency from speed-synchronous to dominant mode-synchronous simply delays the OIS but does not change the above findings. This issue arises from the unsuitability of hysteretic damping for damped free vibration analysis, thus necessitating a judicious conversion of the damping model. It would not be encountered if a Coulomb damping model were used [25, 26], but formidable numerical issues relating to the TNDA and Jacobian of the coupled rotor/air-film/foil domains would then need to be resolved.

Experimental studies would be required to confirm the predictive advantage gained by considering top foil detachment, but that would be the subject of separate research.

APPENDIX A

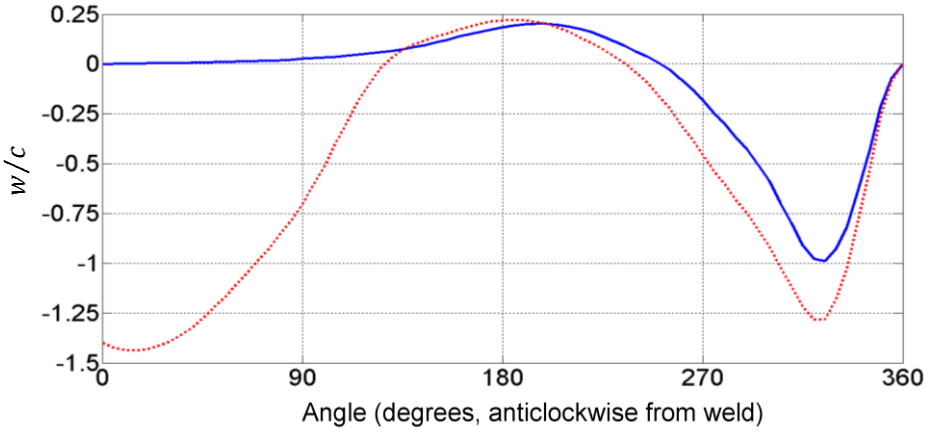

Figure A.1. Non-dimensional radial deflection of top foil for the steady-state condition at 12 krpm, zero rotor unbalance, symmetric rotor-FAB system with single-pad FABs, FLE/CTE, assuming modal beam top foil and smoothed bilinear discrete bump force ($\varrho = 10^{-3}$) and two pressure conditions at weld: $p = p_a$ condition at weld, as in Figure 24b (blue solid line); no pressure constraint at weld, as in Figure 32b (red dotted line).

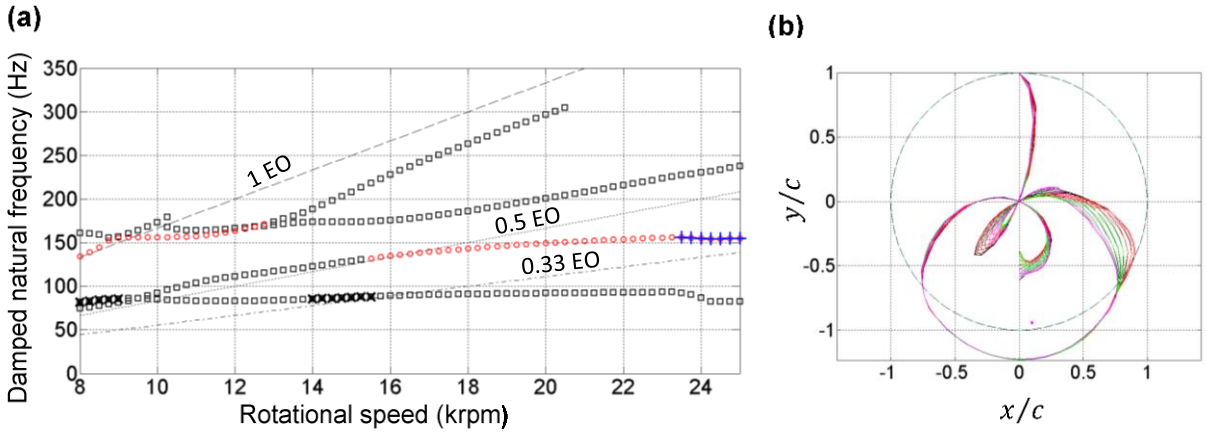

Figure A.2. Results of free vibration eigenvalue analysis for the locus of SEPs in Figure 33a: (a) Campbell diagram extracted using minimum journal amplitude criterion, eq. (33) and a maximum modal damping criterion, $\zeta_n < 0.7$; (b) dominant unstable mode at 19.5 krpm ($f_{d,n} = 10.3$ kHz, $\zeta_n = -9.5828 \times 10^{-5}$) that is rejected from Campbell diagram in (a) due to negligible journal vibration (notation for (a): black squares - forward whirl; red circles - reverse whirl; black oblique crosses - dominant instability; blue upright crosses - secondary instability)

REFERENCES

[1] C. DellaCorte, R.J. Bruckner, Remaining technical challenges and future plans for oil-free turbomachinery, Journal of Engineering for Gas Turbines and Power 133 (2011) 042502. https://doi.org/10.1115/1.4002271.

[2] P. Bonello, M.F. Bin Hassan, An experimental and theoretical analysis of a foil-air bearing rotor system, J. Sound Vib. 413 (2018) 395-420. https://doi.org/10.1016/j.jsv.2017.10.036.

[3] P. Bonello, The extraction of Campbell diagrams from the dynamical system representation of a foil-air bearing rotor model, Mech. Syst. Signal Process. 129 (2019) 502-530. https://doi.org/10.1016/j.ymssp.2019.04.018.

[4] D. Kim, Parametric studies on static and dynamic performance of air foil bearings with different top foil geometries and bump stiffness distributions, Journal of Tribology. 129(2) (2007) 354-364. https://doi.org/10.1115/1.2540065.

[5] R. Hoffmann, T. Pronobis, R. Liebich, Non-linear stability analysis of a modified gas foil bearing structure, in P. Pennacchi (Ed.): Proceedings of the 9th IFToMM International Conference on Rotor Dynamics, Politecnico di Milano, Italy, 2015, pp. 1259–1276. http://dx.doi.org/10.1007/978-3-319-06590-8_103.

[6] J.P. Peng, M. Carpino, Calculation of stiffness and damping coefficients for elastically supported gas foil bearings, Journal of Tribology. 115 (1993) 20–27.

[7] J.S. Larsen, I.F. Santos, S. von Osmanski, Stability of rigid rotors supported by air foil bearings: Comparison of two fundamental approaches, J. Sound Vib. 381 (2016) 179-191. https://doi.org/10.1016/j.jsv.2016.06.022.

[8] K. Sim, Y-B Lee, T. H. Kim, J. Lee, Rotordynamic performance of shimmed gas foil bearings for oil-free turbochargers, Journal of Tribology. 134 (2012) 031102. https://doi.org/10.1115/1.4005892.

[9] R. Hoffmann, R. Liebich, Characterisation and calculation of nonlinear vibrations in gas foil bearing systems – An experimental and numerical investigation, J. Sound Vib. 412 (2018) 389-409. https://doi.org/10.1016/j.jsv.2017.09.040.

[10] P. Bonello, H. M. Pham, The efficient computation of the nonlinear dynamic response of a foil–air bearing rotor system, J. Sound Vib. 333(15) (2014) 3459-3478. https://doi.org/10.1016/j.jsv.2014.03.001.

[11] P. Bonello, H. M. Pham, Nonlinear dynamic analysis of high speed oil-free turbomachinery with focus on stability and self-excited vibration, Journal of Tribology. 136(4) (2014) 041705. https://doi.org/10.1115/1.4027859.

[12] J.S. Larsen, B.B. Nielsen, I.F. Santos, On the Numerical Simulation of Nonlinear Transient Behaviour of Compliant Air-Foil Bearings, in: Proceedings of SIRM 2015, Magdeburg, Deutschland, 2015, Paper-ID 39.

[13] J.S. Larsen, I.F. Santos, On the nonlinear steady-state response of rigid rotors supported by air foil bearings – Theory and experiments, J. Sound Vib. 346 (2015) 284-297. https://doi.org/10.1016/j.jsv.2015.02.017.

[14] H.M. Pham, P. Bonello, Efficient Techniques for the Computation of the Nonlinear Dynamics of a Foil-Air Bearing-Rotor System, in: Proceedings of the ASME Turbo Expo 2013, San Antonio, Texas, USA, paper no. GT-2013-94389.

[15] P. Bonello, A new method for the calculation of the Campbell diagram of a foil-air bearing rotor model, in: I. Santos (Ed.), Proceedings of the 13th SIRM: The 13th Int. Conference on Dynamics of Rotating Machinery, Technical University of Denmark (DTU), Kgs. Lyngby, 2019, pp. 4–13.

[16] S. von Osmanski, J.S. Larsen, I.F. Santos, Multi-domain stability and modal analysis applied to Gas Foil Bearings: Three approaches, J. Sound Vib. 472 (2020) 115174. https://doi.org/ 10.1016/j.jsv.2020.115174 .

[17] B.B. Nielsen, I.F. Santos, Transient and steady state behaviour of elasto-aerodynamic air foil bearings, considering bump foil compliance and top foil inertia and flexibility: a numerical

investigation, Proc. IMechE Part J: Journal of Engineering Tribology. 231(10) (2017). https://doi.org/10.1177/1350650117689985.

[18] T. Leister, C. Baum, W. Seemann, On the importance of frictional energy dissipation in the prevention of undesirable self-excited vibrations in gas foil bearing rotor systems, Technische Mechanik. 37(2-5) (2017) 280-290. https://doi.org/10.24352/UB.OVGU-2017-104.

[19] G. Schilling, K. Bauerlein, R. Liebich, Numerical description of a rotor Supported by gas polymer bearings for time domain simulations - implementation and parametrization of the structure model, in: I. Santos (Ed.), Proceedings of the 13th SIRM: The 13th Int. Conference on Dynamics of Rotating Machinery, Technical University of Denmark (DTU), Kgs. Lyngby, 2019, pp. 340-349.

[20] Y. Gu, Y. Ma, G. Ren, Stability and vibration characteristics of a rotor-gas foil bearings system with high-static-low-dynamic-stiffness supports, J. Sound Vib. 397 (2019) 152-170. https://doi.org/10.1016/j.jsv.2017.02.047.

[21] T. Pronobis, R. Liebich, Comparison of stability limits obtained by time integration and perturbation approach for Gas Foil Bearings, J. Sound Vib. 458 (2019) 497–509. https://doi.org/10.1016/j.jsv.2019.06.034.

[22] M.F. Bin Hassan, P. Bonello, A new modal-based approach for modelling the bump foil structure in the simultaneous solution of foil-air bearing rotor dynamic problems, Journal of Sound and Vibration. 396 (2017) 255-273. https://doi.org/10.1016/j.jsv.2017.02.028.

[23] J. A. Walowit, J. N. Anno, Modern developments in lubrication mechanics, Applied Science Publishers London, 1975.

[24] B. B. Nielsen, Combining Gas Bearing and Smart Material Technologies for Improved Machine Performance: Theory and Experiment, Ph.D. thesis, DTU Mechanical Engineering. DCAMM Special Report, no. S221, ISBN 978-87-7475-481-7 Technical University of Denmark, Lingby, Denmark, 2017.

[25] M. Arghir, O. Benchekroun, A simplified structural model of bump-type foil bearings based on contact mechanics including gaps and friction, Tribology International. 134 (2019) 129-144. https://doi.org/10.1016/j.triboint.2019.01.038.

[26] S. Le Lez, M. Arghir, J. Frêne, Nonlinear numerical prediction of gas foil bearing stability and unbalanced response, Journal of Engineering for Gas Turbines and Power. 131(1) (2009) 012503. https://doi.org/10.1115/1.2967481.

[27] S. S. Rao, Mechanical Vibrations (Fifth Edition), Prentice Hall, Upper Saddle River N. J., 2011.

[28] S.H. Crandall, The role of damping in vibration theory, Journal of Sound and Vibration. 11(1) (1970) 3-18.